Photodegradation of Perfluorooctanoic Acid (PFOA) and Perfluorooctane Sulfonic Acid (PFOS) via Heterogeneous Indium Oxide (In_2O_3)/Gallium Oxide (Ga_2O_3) Nanocomposite

RUKİYE ÖZTEKİN, DELİA TERESA SPONZA*
Department of Environmental Engineering
Dokuz Eylül University
Tınaztepe Campus, 35160 Buca/Izmir,
TURKEY

**Corresponding Author*

Abstract: - The heterogeneous photocatalysis of perfluoroalkyl substances (PFAS), is an effective and advanced technology for their removal from water with relatively high efficiency. PFASs have received increasing attention in recent years, particularly because of their potential as reproductive and developmental toxins, endocrine disruptors, and carcinogens. Perfluorooctanoic acid (PFOA) and perfluorooctane sulfonic acid (PFOS) photodegradation were investigated with heterogeneous indium oxide (In2O3)/gallium oxide (Ga2O3) nanocomposite under increasing sun ligth powers, In2O3/Ga2O3 nanocomposite concentration, pH, temperature, PFOA and PFOS concentrations. The characterizations and morphological properties of samples were measured with XRD, EDX, XPS, FTIR, ICP-OES, STEM and FESEM analyses, respectively. XRD pattern of In2O3/Ga2O3 displays a number of peaks at 2θ = 20.50o, 30.40o, 36.11o, 52.37o, and 60.02o, respectively, corroborated to (221), (222), (400), (440) and (622) lattice planes of monoclinic WO3 (JCPDS # 08–0459). For maximum 99% PFOA and 98% PFOS photodegradation efficiencies the In2O3/Ga2O3 anocomposite concentration, and time should be 0.75 mg/l and 5 min at 1000 mg/l PFOA and PFOS concentrations. The In/Ga ratios with In2O3 target powers of 40 W were 69.80% in the In2O3/Ga2O3 nanocomposites with EDS spectrum. Spectrums of oxygen, gallium and indium were measured at 64.31%, 21.02% and 14.67%, respectively, in the In2O3/Ga2O3 nanocomposites. We observed that when the In2O3 target power increases, the ratio of indium to gallium also increases, which means that the proportion of indium increases, and the conductivity will improve. In2O3/Ga2O3 heterostructures possess significantly lower resistivity (0.49 ω.cm) (higher conductivity) compared with pure Ga2O3 nanobelts (10.87 ω.cm) as well as Ga2O3 nanowires (300-500 ω.cm). The reusability studies showed the resistance of the In2O3/Ga2O3 heterogenous nanocomposite.Up to the 60th cycle, the photodegradation efficiencies for both PFOA and PFOS were consistently recorded at 99%. After the 80th cycle, the efficiency slightly decreased to 98%, and after 100th cycles 97% photodegradation yields was detected. The optimized conditions for pH, rotating speed and temperature should be as follows: 7.0, 30/40oC and 5 rpm, respectively. The PFOA and PFOS photodegradation kinetic can be defined by Langmuir–Hinshelwood equation with k values of 0.087 and 0.099 min-1 for PFOS and PFOA, respectively at a sun ligth power of 80 W/m2. The fluorine content associated with declined PFOS, confirming that fluorine phase increased steadily, indicating defluorination process was occurred. The defluorination percentage increased proportionally with treatment time, reaching approximately 86-88% after photodegradation process.

Key-Words: - Gallium oxide (Ga2O3); Indium oxide (In2O3); Nanocomposites (NCs); Perfluoroalkyl substances (PFAS); Perfluorocarboxylic acids (PFCAs); Perfluorooctanoic acid (PFOA); Perfluorooctane sulfonic acid (PFOS); Persistent organic contaminants; Photocatalyst; Photodegradation.

Received: December 13, 2025. Revised: February 19, 2026. Accepted: March 14, 2026. Published: June 26, 2026.

1 Introduction

Per- and polyfluoroalkyl substances (PFAS) (Figure 1a), such as perfluorooctanoic acid (PFOA) (Figure 1b) and perfluorooctane sulfonic acid (PFOS) (Figure 1c), have become widespread environmental pollutants due to their extensive use in industrial and urban activities, [1]. High concentrations of PFAS are frequently detected in areas near airports, textile mills, and metal smelting industries, where they compromise the safety of drinking water sources. Long-chain PFAS are introduced into aquatic systems through

industrial effluents and atmospheric deposition, posing significant environmental and health challenges, [1], [2]. These substances are highly persistent, bioaccumulate, and exhibit toxicity, leading to their association with numerous health issues, including thyroid dysfunction, liver damage, immune suppression, reproductive toxicity, and potential carcinogenicity, [3]. PFAS can disrupt endocrine function by interfering with thyroid hormone transport and metabolism, which may contribute to developmental and metabolic disorders, [4]. Moreover, PFAS exposure has been associated with hepatotoxicity, characterized by altered lipid metabolism and liver enzyme dysregulation, increasing the risk of metabolic diseases, [5]. Furthermore, the accumulation of PFAS in aquatic ecosystems and drinking water sources disrupts microbial community structures, threatening ecosystem stability, [6]. Recent studies have also emphasized the role of PFAS in promoting the spread of antibiotic resistance genes (ARGs), with elevated levels of ARGs detected in PFAS-contaminated environments, [7], [8]. To mitigate these risks, stringent regulations and effective remediation technologies must be developed to address both the toxicological effects and ecological impact of PFAS contamination. Despite regulatory efforts, many frameworks inadequately address ultra-short-chain PFAS, emphasizing the critical need for a globally unified regulatory approach. Current regulations often fail to manage PFAS comprehensively, especially ultra-short-chain variants, highlighting the necessity for more inclusive global regulatory strategies, [9].

* Figure 1 can be found in the Appendix section.

PFAS have drawn increasing attention in recent years mainly because they are potential reproductive and developmental toxins, endocrine disrupters, and carcinogens, [10], although the relationship between PFAS and particular human disease is not established yet. It is a fact that PFAS exist not only in different environmental media but also in human body. Well-known PFAS such as PFOA and PFOS both commonly constitute high proposition of PFAS that have been detected in the aquatic environment, [11]. The source of PFAS in the environment can be divided into direct and indirect pathways, [12]. The direct route represents the emission from the manufacture and use of PFAS, or wastewater treatment plants (WWTP), [13]. The indirect route refers to the long-range transport and degradation products from precursor compounds such as fluorotelomer alcohols and perfluorooctane sulfonyl fluoride, [14]. Furthermore, it was reported that the direct route is accounting for more than 80% of the total source for PFAS in the environment, [15]. The transport of such compounds could also be separated as atmospheric and aqueous transport pathways, [16]. The atmospheric transport involves that PFAS diffuse in the atmosphere and then deposit on land or in water. The aqueous transport suggests the dissolution in water and transport by the currents to the other water matrices. The contamination of PFAS in the aquatic environment has been widely reported. In Spanish rivers, PFAS were found to be 43 ng/l, [17]. Zhang et al., [18], detected 16 PFAS in WWTP in China, with concentrations ranging from 0.04 to 91 ng/l in the influent. In addition, high PFOA concentration was detected in both the influent (2-91 ng/l) and effluent (3-107 ng/l) from WWTP. Moreover, serious PFAS water contamination was reported for the industrialized cities such as Dalian, China, [19], and Tokyo, Japan, [20]. Furthermore, as high as 68.6 ng/l of PFOA was detected in the Korean coastal water, [21]. Overall, water contamination by PFAS is wide spread demonstrating a variety of sources and potential persistence.

PFAS contamination stems from multiple sources, including aqueous film-forming foams, non-stick coatings, and industrial runoff, all of which have a negative impact on marine ecosystems and drinking water supplies, [22]. Exposure to these substances has been linked to various adverse health effects such as thyroid dysfunction, liver damage, immune suppression, reproductive issues, and potential carcinogenic risks, [23]. Effectively addressing these concerns requires strong international collaboration and standardized mitigation strategies to safeguard public health and the environment. For instance, the National Primary Drinking Water Regulations (NPDWR) set a stringent limit of 0.0040 parts per billion (ppb) for PFOA and PFOS in drinking water, [24]. Due to their persistence and potential risks, PFASs are considered a major environmental and public health concern, making them a research focus for scientists, regulators, and policymakers all over the world. The U.S. EPA set a health advisory level of 0.070 g/l for PFASs in 2016; this level was recently reduced to 0.004 ng/l for PFOA and 0.02 ng/l for PFOS, [25]. The EU Water Framework Directive has proposed a limit value of 0.10 g/l for twenty PFASs in total, [26]. In many cases, however, the PFAS levels in drinking water sources surpass the safety threshold, necessitating treatment methodologies for PFASs in water to mitigate their adverse effects.

Various treatment technologies have been developed to remove PFAS from water. Physical adsorption methods, such as granular activated carbon (GAC), powdered activated carbon (PAC), anion

exchange (AIX), molecularly imprinted polymers (MIP), and biomaterials, have shown promising removal efficiency, [27]. Their efficiency decreases when targeting short-chain PFAS due to their higher mobility, [28]. High-pressure-driven membrane processes like nanofiltration (NF) and reverse osmosis (RO) have also demonstrated significant effectiveness in separating PFAS, [29]. Nanofiltration (NF) offers moderate effectiveness, particularly for larger PFAS molecules, but may struggle with smaller variants. While NF can be a viable option, it comes with high costs related to membranes and energy, depending on system design and maintenance requirements. Challenges include membrane fouling, brine waste generation, and the need for periodic cleaning, monitoring, and maintenance to sustain performance. In contrast, reverse osmosis (RO) is highly effective at removing a wide range of PFAS, including short-chain compounds, but at a higher operational and capital cost. RO systems are energy-intensive and prone to membrane fouling, necessitating frequent maintenance, careful pressure management, and regular membrane replacement to ensure long-term efficiency, [27].

Photocatalytic degradation methods have attracted considerable attention for PFAS degradation and defluorination, due to their potential to address various environmental and energy-related challenges, [30]. Recent advancements have demonstrated promising outcomes, achieving complete PFAS mineralization through biological degradation and advanced oxidation processes (AOPs), including photochemical, sonolysis, electrochemical, thermolysis, chemical oxidation and reduction, plasma, subcritical, and radiochemical treatments, [31]. Among these, photochemical processes have shown remarkable PFAS dissociation and defluorination under ambient conditions, underscoring their potential as a key technology for PFAS degradation, [32]. Moreover, AOPs, such as electrochemical methods, radiation, ultrasound, ozonation, Fenton and photo-Fenton reactions, and plasma treatments, have emerged as effective alternatives to conventional approaches, [33]. At the recent literature studies have highlighted photocatalysis as a highly promising approach for PFAS removal, offering advantage over conventional methods such as adsorption and ozonation in terms of pollutant degradation efficiency and versatility. This advanced technology demonstrates considerable potential for addressing persistent organic pollutants and achieving cleaner and safer environments, [34].

The most microorganisms do not have the ability to decompose PFAS in water. Thus, technologies that cleavage C-F bonds are more suitable for PFAS removal. As an alternative, photolysis is recognized as an appealing option, which could degrade a variety of toxic substances e.g. agrochemicals in the presence of artificial or solar light and is environmentally friendly and cost effective, [35]. However, Due to the strong bonding energy in C-F, direct photolysis for the removal of PFAS from water is still of low efficacy. Giri et al., [36], used UV light (254 nm wavelength) for the photodegradation of PFOA in dilute aqueous solution, and observed no removal of PFOA within the reaction period of 300 min. This is mainly attributed to the fact that the bond dissociation energy of C - F bonds is up to 544 kJ/mol, whereas the photon energy of UV light with a wavelength of 254 nm is only 471 kJ/mol. So, C-F bonds are only likely to be cleaved by light of shorter wavelengths (e.g. photon energy=647 kJ/mol at 185 nm), [37]. In comparison, by utilizing the photon (h_v) absorption capacity of some catalysts, heterogeneous photocatalysis has been developed to decompose PFAS which can be conducted under a wider range of light wavelength. During heterogeneous photocatalysis, the contaminant and catalyst exist in the different phases and the process could be described as absorbing h_v and then generating negatively charged electron (e^-) and positively charged hole (h^+) pairs, which will migrate to the surface of the photocatalyst particles and react with adsorbed contaminant resulting in its decomposition. It has been proven that heterogeneous photocatalysis catalysts such as TiO_2, gallium oxide (Ga_2O_3), and indium oxide (In_2O_3) are far more effective for PFAS removal than direct photolysis, [38].

In_2O_3 is a PFAS affinity material with a narrow bandgap of 2.8 eV, exceptional photocatalytic activity, and sensitivity to visible light. When compared to TiO_2, In_2O_3 has shown a remarkable 8.4-fold increase in the degradation rate coefficient of a PFAS (PFOA) under UV irradiation. These findings suggest it is a promising photocatalyst for PFAS decomposition, [39]. Modifications are necessary for In_2O_3 due to its limitations, i.e., its low specific surface area and the rapid recombination of photogenerated electron-hole pairs. One effective approach is the generation of oxygen vacancies on the In_2O_3 surface, which enhances its photocatalytic performance. Additionally, nanostructures like nanospheres, [40], (porous) nanosheets, and nano cubes, [41], have been developed to provide adsorption sites for PFOA and oxygen atom binding sites in the carboxyl groups. These modifications ultimately contribute to the improved photocatalytic decomposition of PFOA. Several composite materials have been reported, such as g-C_3N_4 - In_2O_3, [42], CeO_2 - In_2O_3, [43], and MnO_x - In_2O_3, [44]. Among them, the deposition of MnO_x onto In_2O_3 surfaces has shown great potential; it creates abundant surface oxygen vacancies in In_2O_3,

leading to the generation of active species and enhanced absorption of solar light (Figure 2). This trend reflects the ongoing research efforts to develop photocatalytic materials for the enhanced degradation of PFASs. Because of its high optical transparency and electric properties, In_2O_3 is used in numerous optoelectronic applications such as photovoltaics, light-emitting diodes, and modern displays, [45].

* Figure 2 can be found in the Appendix section.

Ga_2O_3 has excellent conductivity and tunable optical properties, despite its wide band-gap (4.9 eV). Studies have demonstrated its remarkable UV photocatalytic activity against PFASs, specifically in the context of peroxymonosulfate (PMS, HSO_5^-)-assisted photocatalytic AOPs. The Ga_2O_3/PMS/UV system, with sulfate radicals ($SO_4^{-\bullet}$) and superoxide radicals ($O^{2-\bullet}$) as key reactive oxygen species (ROS), achieves 100% degradation within 60 min, [46]. The studies on Ga_2O_3 focuses on structure engineering to enhance its photocatalytic activity, primarily through size and morphology control. For example, synthesizing the compound into nanoparticles, monoclinic rod-like crystals, needle-like structures, and sheet-like structures has shown promising results. Furthermore, modifications have been explored to further improve the photocatalytic activity of Ga_2O_3. One common approach is metal-doping, such as Sn-doped-Ga_2O_3, [47], and In-doped Ga_2O_3 (Figure 3), [48]. Metal-doping on Ga_2O_3 promotes photocatalytic degradation by enhancing absorption through the hole oxidation process. This strategy provides a new method for removing PFOA from different water sources, capitalizing on the strong bonding ability between metal-doped Ga_2O_3 and PFASs. Ga_2O_3 can be applied as oxygen-gas sensors, as surface passivation of solar cells, and in electroluminescent devices, [49].

* Figure 3 can be found in the Appendix section.

In_2O_3 and Ga_2O_3 have advanced use in the degradation of PFOA, a key contaminant in PFAS, [50]. A MnO_x-modified, oxygen-vacancy-rich In_2O_3 submicro-rod photocatalyst (MnO_x/In_2O_3-Ov SR) has been developed for enhanced PFOA removal. The incorporation of manganese oxide increases the surface area, adsorption capacity, and photocatalytic activity under solar light irradiation, resulting in improved degradation and defluorination efficiencies. This enhancement is attributed to the increased generation of ROS, such as hydroxyl ($OH^\bullet$) and $O^{2-\bullet}$ radicals, essential for pollutant breakdown, [44].

Ga_2O_3 has also been explored as a stable, non-toxic photocatalyst for aqueous PFOA treatment, surpassing traditional catalysts like titanium dioxide (TiO_2). A Ga_2O_3-peroxymonosulfate (PMS) system, activated by UV light, produces $SO_4^\bullet$, significantly enhancing degradation efficiency. Under optimal conditions (UV irradiation at 185 nm, pH=3.0), this system achieves complete PFOA degradation within 60–90 min. Mechanistic studies reveal step-wise degradation of PFOA to shorter-chain intermediates, such as perfluoroheptanoic acid (PFHpA) and perfluorohexanoic acid (PFHxA), driven by sulfate ($SO_4^{2-\bullet}$) and $O^{2-\bullet}$ radicals, with $OH^\bullet$ radicals assisting. Notably, the system demonstrates a TOC removal rate of 75–85%, highlighting its practical potential for wastewater treatment, [46].

A nanostructured, sheaf-like Ga_2O_3 photocatalyst was synthesized through a polyvinyl alcohol (PVA)-assisted hydrothermal method followed by heat treatment. This morphology provides a high specific surface area (36.10 m^2/g) and nanoporous structure, enhancing interaction with PFOA molecules. The sheaf-like Ga_2O_3 exhibited a decomposition rate constant of 4.85% h^{-1} under λ=254 nm UV irradiation, with efficiencies 16 times greater than commercial Ga_2O_3 and 44 times higher than P25 TiO_2. Under vacuum UV (VUV) irradiation at λ=185 nm, the catalyst effectively removed trace PFOA from secondary effluents, overcoming interference from organic matter and bicarbonate in wastewater. The photocatalyst displayed excellent stability and reusability, maintaining high efficiency over multiple cycles, positioning it as a promising candidate for PFAS removal in water treatment, [51].

A Bi_4O_7-modified Ga_2O_3 composite ($GaBi_{10}$) was developed to improve photocatalytic efficiency for PFOA degradation. The $GaBi_{10}$ composite exhibited enhanced light absorption, charge carrier separation, and adsorption capacity. Compared to pure Ga_2O_3, which achieved only 5.82% degradation, $GaBi_{10}$ demonstrated a significantly higher defluorination rate of 59.60%, effectively breaking down the C–F bonds in PFOA. Despite a lower mineralization rate (TOC reduction of 64.10%), these results suggest that intermediate products hinder complete mineralization. The $GaBi_{10}$ composite outperformed previous catalysts in degradation, defluorination, and mineralization. However, variations in experimental conditions across studies pose challenges for standardizing performance comparisons. This research emphasizes the importance of optimizing catalyst design and experimental parameters to advance the photocatalytic degradation of PFAS pollutants, like PFOA, and improve environmental remediation strategies, [52].

In addition to TiO_2, alternative materials such as Ga_2O_3 and In_2O_3 have shown promising results in

PFAS degradation due to their superior photocatalytic properties in specific structural forms. The effectiveness of these semiconductors is largely determined by their bandgap, which governs their ability to absorb light within the UV–visible spectrum, [53].

Recent studies have highlighted the potential of semiconductor-based photocatalysts for PFAS degradation, particularly metal oxides with reduced bandgaps that extend light absorption into a broader spectrum. In_2O_3 and Ga_2O_3 have demonstrated promising performance for PFOA degradation. Nano-structured metal oxides with reduced bandgaps, such as In_2O_3, extend light absorption into a broader spectrum, further improving photocatalytic activity under diverse irradiation conditions. Additionally, the introduction of foreign metals on semiconductor surfaces promotes charge carrier separation, minimizing electron-hole recombination and sustaining the photocatalytic process, ultimately resulting in more efficient PFAS degradation, [32]. The photocatalytic degradation of PFAS have led to the development of innovative materials and strategies, each offering distinct mechanisms and performance characteristics. Traditional semiconductor-based photocatalysts, such as TiO_2, Ga_2O_3, and In_2O_3, have been widely studied for their strong oxidative potential, [54]. However, their efficiency is often limited by their wide bandgaps, which restrict activation to UV light, reducing practicality under natural sunlight.

Dissolved organic matter (DOM) is normally considered to be a significant factor that affects photodegradation process due to the generation of DOM-derived oxidative intermediates or their physicochemical quenching effects, [55]. Therefore, to assess the feasibility of three main catalysts (TiO_2, In_2O_3, Ga_2O_3) to degrade PFAS in wastewater, the photocatalysis efficacies for PFOA removal in WWTP effluent was investigated, [51], [56]. It can be observed that PFOA decomposition in wastewater under UV irradiation is obviously retarded compared with the degradation efficacy in pure water and the photocatalytic ability under UV light followed the order as needle-like Ga_2O_3 > In_2O_3 > TiO_2. Specifically, the needle-like Ga_2O_3 degraded 100% PFOA in wastewater which was spiked with 500 mg/l of PFOA within 180 min however this reaction period could be shortened to 40 min when the contaminant was from pure water. The same phenomenon is also observed in the In_2O_3 photocatalysis process. In pure water, 69% PFOA could be degraded by In_2O_3 within 180 min when the experimental solution was spiked with 100 mmol/l of PFOA; however, this value was decreased to only 10% when the contaminant was from wastewater. Such difference in PFOA degradation is likely due to the presence of DOM in high concentrations in real wastewater. These results are attributed to the fact that DOM most likely occupies the surface of the catalysts instead of PFOA, leading to less adsorption capacity of this pollutant. As a result, the PFOA photo-decomposition is largely inhibited and the efficacy is reduced.

Two significant methods were examined to solve the photo-decomposition problem, [56]. Firstly, ozone gas [O_3(g)] (≈ 8 mg/l.h) was added in the wastewater photodegradation by In_2O_3/UV compared with no ozone gas addition. The ozone addition largely promotes the efficacy of PFOA removal in wastewater, due to the fact that the addition of ozone could promote abundant photo-produced h^+ to react with PFOA rather than recombining with photo-produce e^-, [57]. Thus, the recombination of e^- - h^+ pairs is inhibited so the photocatalytic removal of PFOA is accelerated. Secondly, needle like Ga_2O_3 in combination with VUV irradiation (λ=185 nm) was conducted and the efficacy is exhibited with its k_t value of 0.059 which is much higher than the value in the needle-like Ga_2O_3/UV system. This is because that VUV light has a shorter wavelength of 185 nm and higher energy which could eliminate the adverse influence of DOM. Some novel catalysts such as In_2O_3 microspheres, In_2O_3 porous nanoplates (PNPs), and Pt-TiO_2 which have high PFOA degradation performance in water have not been examined in treating real wastewater, hence the potential negative influence of DOM should be further investigated.

Wastewater is highly complex in chemical composition due to the presence of many organic and inorganic substances e.g. DOM and bicarbonate. DOM is also a significant scavenger of oxidants and reductants as discussed above. Under realistic conditions, the impact of DOM for PFAS removal will be much worse. For bicarbonate in wastewater, as it has the same carboxyl group as PFOA, the competition between them will reduce the amount of PFOA adsorbed on catalyst surface hence its photodegradation. Thus, factors need to be considered for the practical application of PFOA degradation. Firstly, the photocatalytic degradation of PFOA can be conducted in a tubular quartz vessel reactor under UV irradiation. A low-pressure mercury lamp (15 W) emitting 254 nm UV light is set up which can be not only provide adequate light intensity (3-6 mW/cm^2) but also energy-saving when dealing with wastewater, [41]. Secondly, needle-like Ga_2O_3, In_2O_3 PNPs, or In_2O_3 microspheres can be used as the catalyst because needle-like Ga_2O_3 has been proven to be efficient (100% PFOA removal within 180 min) dealing with wastewater and In_2O_3 PNPs, or In_2O_3 microspheres is

able to degrade FPOA in pure water efficiently (100% PFOA removal within 30 and 17 min, respectively), so it is worth to test their performance in wastewater. Thirdly, during the degradation process, controlling factors should be set up as follows for the best efficacy: room temperature to save energy; acidic solution (pH=4.0) to promote high adsorption of PFAS and performance of e^- - h^+ pairs; ozone addition to eliminate the adverse influence of DOM; contact period of 60-180 min for the complete degradation of PFAS. Furthermore, as the boiling point of PFOA is 189ºC, heat treatment (e.g. 200ºC) can be applied for the regeneration of the catalyst to be efficiently reused.

In the present study, the photodegradation of perfluorooctanoic acid (PFOA) and perfluorooctane sulfonic acid (PFOS) were aimed with heterogeneous In_2O_3/Ga_2O_3 nanocomposites under different operational conditions. The characterizations and morphological properties of samples were measured with XRD, EDX, XPS, FTIR, ICP-OES, STEM and FESEM analyses, respectively.

2 Materials and Methods

2.1 Materials

Indium (III) chloride tetrahydrate ($InCl_3.4H_2O$), Aldrich), ethanol and gallium nitrate hydrate ($Ga(NO_3)_3.H_2O$) were purchased from Sigma-Aldrich, Germany. All chemicals were all of analytical grade and used without further purification. The number of water molecules in $Ga(NO_3)_3.H_2O$ determined by thermogravimetric analysis (TGA).

2.2 Preparation of In_2O_3 Porous Nanoplates (PNPs)

The precursor of In_2O_3, i.e. $In(OH)_3$ PNPs were synthesized by a simple ethylenediamine-assisted hydrothermal process. In a typical synthesis, 10 ml aqueous $In(NO_3)_4.5H_2O$ solution (0.5 M) and 10 ml of ethylenediamine were mixed with vigorous stirring. After being stirred for 15 min, the mixture was transferred into a 25 ml Teflon-lined stainless-steel autoclave. The autoclave was sealed and maintained at 180°C for 16 h. After being naturally cooled down to room temperature, the white precipitates, i.e. $In(OH)_3$ were collected by centrifugation and washed with deionized water and ethanol. In_2O_3 PNPs were obtained by calcining $In(OH)_3$ precursor at 270°C for 2 h in air. For comparison, non-porous In_2O_3 nanoplates were also synthesized by calcining porous $In(OH)_3$ at 500°C for 2 h.

2.3 Preparation of Ga_2O_3 Nanoparticles (NPs)

All reagents were analytical grade and were used as received. Ga_2O_3 was synthesized by a hydrothermal method followed by calcination. In a typical procedure, 2 g (5 mmol) of $Ga(NO_3)_3.H_2O$ and 0.1173 g of PVA (M_W=22000) were dissolved in 20 ml pure water, and the pH was adjusted to 6.4 using NaOH solution. After heating at 90°C for 10 min, the mixture was transferred into a 25 ml Teflon-lined stainless-steel autoclave and maintained at 200°C for 8 h. After the autoclave was naturally cooled at room temperature.

2.4 Synthesis of In_2O_3/Ga_2O_3 Nanocomposites

The 18 × 18 mm^2 silicon (Si) (100) samples with 100 nm oxide layer deposited by Plasma-Enhanced Chemical Vapor Deposition (PECVD) method were used in the study. On the samples, the 1, 3, 5 and 10 nm thick Au layer was evaporated thermally (K. J. Lesker, PVD 225). These Au layers served as a catalyst for nanowires growth in the Vapor-Liquid-Solid (VLS) method.

The Ga_2O_3 and In_2O_3 nanowires were synthesized in a high-temperature furnace with a horizontal quartz tube. Precursors of aluminium ions (AI^{+2}) atoms were metallic gallium (5N) and metallic indium (6N). During processes, the samples were arranged in a reactor at different ways and distances from the metallic source. To synthesis Ga_2O_3 nanowires the distance was 10 mm, and the samples were placed vertically in the tube. To synthesis In_2O_3 nanowires the distance was 50 mm and the samples were arranged horizontally. The growth of nanostructures was conducted at high temperature (Ga_2O_3 – 1012ºC, 2 min; In_2O_3 – 800ºC, 10 min) at atmospheric pressure. During the process, a gas mixture consisting of nitrogen (N_2) and deionized water (DI water) vapor was flowing through the reactor with a constant flow of 1300 sec/cm.

2.5 Characterizations

2.5.1 X-Ray Diffraction (XRD) Analysis

Powder XRD patterns were recorded on a Shimadzu XRD-7000, Japan diffractometer using Cu Kα radiation (λ=1.5418 Å, 40 kV, 40 mA) at a scanning speed of 1º /min in the 10-80º 2θ range. Raman spectrum was collected with a Horiba Jobin Yvon-Labram HR UV-Visible NIR (200-1600 nm) Raman microscope spectrometer, using a laser with the wavelength of 512 nm. The Raman spectrum was collected from 10 scans at a resolution of 2 /cm. The zeta potential was measured with a SurPASS Electrokinetic Analyzer (Austria) with a clamping cell at 300 mbar.

2.5.2 Energy Dispersive X-Ray Analysis (EDX) Analysis

To investigate the morphological properties and structure of the synthesized catalyst and the composition of the elements present in the synthesized catalyst; an EDX spectrometry instrument (TESCAN Co., Model III MIRA) was used.

2.5.3 X-Ray Photo Spectroscopy (XPS) Analysis

The valence state of the samples was investigated and was analyzed using XPS (ESCALAB 250Xi, England). XPS used an Al Kα source and surface chemical composition and reduction state analyses was done, with the core levels recorded using a pass energy of 30 eV (resolution ≈ 0.10 eV). The peak fitting of the individual core-levels was done using XPS-peak 41 software, achieving better fitting and component identification. All binding energies were calibrated to the C 1s peak originating from C–H or C–C groups at 284.6 eV.

2.5.4 Fourier Transform Infrared Spectroscopy (FTIR) Analysis

The FTIR spectra of samples was recorded using the FT-NIR spectroscope (RAYLEIGH, WQF-510). Experimental In_2O_3/Ga_2O_3 nanocomposite samples were scanned using infrared light and their chemical properties were obtained in FTIR spectra.

2.5.5 Inductively Coupled Plasma Optical Emission Spectrometry (ICP-OES) Analysis

ICP-OES analysis was employed to determine In and Ga contents and measured on a Varian 720-ES (Varian Inc., Palo Alto, CA, USA). Solutions from the powder were prepared via acidic leaching. Respective metals were detached from silica in a sealed container using saturated hydrochloric acid (HCl) (35%) at 120ºC. The spectroscope was three-point calibrated with a commercially available, diluted standard for In and Ga. Mass fractions of carbon, hydrogen, nitrogen, and sulfur were determined by combustion analysis (CHN), executed on a EuroEA Elemental Analyzer (HEKAtech GmbH, Wegberg, Germany).

2.5.6 Scanning Transmission Electron Microscopy (STEM) Analysis

STEM analysis was performed on an FEI Talos F200X (Thermo Fisher Scientific, Waltham, MA, USA) with an XFEG field emission gun and acceleration voltage of 200 kV.

2.5.7 Field Emission Scanning Electron Microscope (FESEM) Analysis

The morphological features and structure of the synthesized catalyst were investigated by FESEM (FESEM, Hitachi S-4700). To investigate the composition of the elements, present in the synthesized In_2O_3, Ga_2O_3 and In_2O_3/Ga_2O_3 nanocomposites; FESEM images were used.

2.6 Determination of Perfluorinated Compounds

About 1 ml of the sample was homogenised with 5 ml of high-purity Milli-Q water. On emillilitre of 0.5 M tetrabutylammonium hydrogen sulphate solution and 2 ml of sodiumcarbonate buff er (0.25 M, pH=10.0) were added to 1 ml of the homogenate samples ina polypropylene (PP) tube and thoroughly mixed for extraction. Five millilitres of methyltert-butyl ether (MTBE) was added to the prepared mixture and shaken for 20 min. Theorganic and aqueous layers were separated by centrifugation, and an exact volume of MTBE (4 ml) was removed from the solution. The aqueous mixture was rinsed with MTBE and separated twice; both the rinses were combined in a second PP tube. The solvent wasevaporated under nitrogen and replaced with 0.5 ml of methanol. This extract was passedthrough a nylon mesh filter (0.2 μm) into a high-performance liquid chromatography (HPLC) vial. The extraction blanks were prepared using Milli-Q water.

2.7 LC-MS/MS Analysis

Liquid chromatography–tandem mass spectrometry (LC-MS/MS) analysis was performedon an AB SCIEX 3200 QTRAP instrument. Betasil C18 column (50 × 2.1 mm i.d., 5 μm) wasused. Ten microlitres of each extract was injected in the LC-MS/MS with 2 mM ammoniumacetate/methanol as the mobile phase starting at 10% methanol. At a flow rate of 300 μl/min, the gradient increased to 95% methanol at 10 min before reverting to original conditions at 15 min. The column temperature was maintained at 25ºC. PFOA and PFOS amounts were determined by comparing their peak areas with those ofstandards in LC-MS/MS. All analyses were repeated three times for each sample. Under theapplied LC-MS/MS conditions, the retention times of PFOA and PFOS were 2.59 and 2.66 min, respectively. Calibration standards were prepared in methanol in the range of0.05–110 ng/ml for PFOA and 0.001–1.0 ng/ml for PFOS. The calibration curves werecreated from six calibration standards. Ten blank wheat grain samples (previously analysed and found to be not contaminated) were fortified with an amount of standard PFOA and PFOS able to produce signal-to-noise ratios ranging from 0.5 to 2.5. All of the blank valueswere averaged, and the average value was

subtracted from the detected PFOA and PFOS values. The limit of detection (LOD) was determined to be three times the standard deviation of the blank test values. The limit of quantification (LOQ) was taken as three times the LOD. Due to the problem of contaminants in the standards, recoveries ofnative chemicals were tested in a series of preliminary experiments instead of using internal standards. C-PFOA was used only for checking the overall recovery of target chemicals during the analytical procedure. All target chemicals were spiked into test samples, and the samples were extracted and analysed following the same procedures as described earlier. Recoveries were evaluated by subtracting the background levels from the detected concentrations. The values of retention time, correlation coefficient, and recovery, LOD and LOQ of PFOA and PFOS are listed in Table 1.

* Table 1 can be found in the Appendix section.

2.8 Quantification of Fluoride Concentrations

Fluoride concentrations were analyzed using the Spectroquant® Fluoride test reagent (Supelco, 1.17236.0001). Fluoride ions react with part of an arsenic-free red zirconium-dye solution to form a colorless complex, which in turn results in a bleaching of the red color (SPADNS method). The concentration of the unconsumed zirconium-dye solution is subsequently determined photometrically at 575 nm. The method is analogous to USEPA 340.1. Samples containing 1 to 19 µg/l fluoride were mixed with the SPADNS reagent solution in a volume ratio of 10/1 and the absorbance was measured after 20 min.

2.9 Mechanism of Photodegradation Process

When the catalyst absorbs a hv with energy equal to or greater than its band gap, an e^- - h^+ pair is generated (Figure 4). So, the band gap energy is critical for this process, too wide or too narrow band gap will be ineffective for photocatalysis. When the band gap of the catalyst is too wide, the light irradiation can only induce a few or even no e transition from valence band to conduction band. Although, the generated e^- - h^+ pair has strong oxidizing-reduction ability, its efficacy for contaminant removal is limited due to the small quantity. With the band gap narrowing, the quantity of e^- - h^+ pairs are raised. However, when the band gap is too narrow, the efficacy is reduced because the oxidizing-reduction ability of e^- - h^+ pair is too weak even though its quantity is increased. Thus, a suitable band gap of the catalyst is essential for its photocatalysis efficiency, [58].

* Figure 4 can be found in the Appendix section.

Once generated, the e^- - h^+ pair will separate into a free e^- and a free h^+. The h^+ in the valence band has high oxidation capacity which can degrade PFAS directly, [59]. In addition, h^+ reacts with H_2O in the solution and produces $OH^\bullet$ radicals which also have a well-known degradation ability for a wide range of organic compounds through an H-atom abstraction to form water. However, in the case of PFAS especially PFOA, all H atoms have been replaced by F-atoms in the carbon chain, thus PFOA is inert to $OH^\bullet$ attack ($k^\bullet OH_{+PFOA} \leq 10^5$ 1/M.s), [60]. Therefore, the less transformation from h^+ to $OH^\bullet$ occurs in the photocatalytic system, the better efficacy will be achieved for PFOA degradation. Besides, e^- moves to the surface of the catalyst and reacts with adsorbed water to form hydrated electrons (e_{aq}^-). PFAS molecules adsorbed on the catalyst surface can be attacked by the e_{aq}^- and degraded into shorter-chain compounds. The specific reaction mechanism is presented in Figure 4. The heterogeneous photocatalysis process can be described in Equations 1-10, [61], [62]:

PFOA decomposed by h^+

$$F(CF_2)_nCOOH + H_2O \rightarrow F(CF_2)_nCOO^- + H_3O^+ (1)$$

$$F(CF_2)_nCOO^- + h^+ \rightarrow F(CF_2)_nCOO^\bullet (2)$$

$$F(CF_2)_nCOO^\bullet \rightarrow F(CF_2)_n^\bullet + CO_2 \uparrow (3)$$

$$F(CF_2)_n^\bullet + O_2 + H_2O \rightarrow F(CF_2)_{n-1}COOH + 2F^- (4)$$

PFOA decomposed by e^-

$$F(CF_2)_nCOOH + e^- \rightarrow (CF_2)_nCOOH^\bullet + F^- (5)$$

$$(CF_2)_nCOOH^\bullet + H_2O \rightarrow (CF_2)_nHCOOH + OH^\bullet (6)$$

$$(CF_2)_nHCOOH + e^- \rightarrow C_nF_{2n-1}COOH^\bullet + F^- (7)$$

$$C_nF_{2n-1}COOH^\bullet + H_2O \rightarrow C_nF_{2n-1}H_2COOH + OH^\bullet (8)$$

$$C_nF_{2n-1}H_2COOH \rightarrow C_{n-1}F_{2n-1}^\bullet + CH_2^\bullet + COOH^\bullet (9)$$

$$C_{n-1}F_{2n-1}^\bullet + COOH^\bullet \rightarrow F(CF_2)_{n-1}COOH (10)$$

where $F(CF_2)_nCOOH$ = $F(CF_2)_7COOH$, $F(CF_2)_6COOH$,….or $F(CF_2)_2COOH$.

Overall, the photo-generated e^- - h^+ pairs take the main responsibility for the contaminant degradation so their quantity and oxidizing-reduction ability decide the degradation efficacy of photocatalysis, [63]. The specific efficacy influenced by e^- - h^+ pairs and discussed based on the particular catalyst and ambient controlling factors.

2.10 Photodegradation Kinetics

Based on the conclusions drawn from the literature, the photodegradation of PFAS follows the pseudo first order kinetics, and the Langmuir-Hinshelwood approach can be introduced to simulate the reaction kinetics during the photocatalysis process, [64], [65], (Eq. 11):

$$r = k\frac{KC}{1+KC} (11)$$

where r is the reaction rate, k is a reaction rate constant, C is the concentration of PFAS, and K is the equilibrium absorption constant. When the chemical concentration C is of micromolar level, namely $KC \ll 1$, Eq. (11) can be simplified as follows (Eq. 12):

$$r = kC = k_{app}C (12)$$

The pseudo-first order kinetics are calculated below in Eq. (13):

$$ln\left(\frac{C}{C_0}\right) = -k_t t (13)$$

Where, k_t is the pseudo time-based first-order rate constant of PFOA degradation. The fluence-based first-order rate constant k_f (cm^2/mJ) is calculated as follows, [66], (Eq. 14):

$$k_f = \frac{k_t}{I_E} (14)$$

Where, I_E is the average light intensity (mW/cm^2). The half-life ($\tau_{1/2}$) of the reactants is described below (Eq. 15):

$$\tau_{1/2} = \frac{ln2}{k_t} (15)$$

The defluorination ratio of PFOA (D_f) is calculated as follows (Eq. 16):

$$D_f = \frac{C_{F^-}}{C_0 \, x \, 15} \, x \, 100\% (16)$$

Where, C_{F^-} is the molar concentration of fluoride ion, C_0 is the initial concentration of PFOA, and the factor of 15 corresponds to the number of fluorine atoms (F^-) in one PFOA molecule. As only very limited literature provided the I_E values in their research, k_t is the most common value for comparing among different catalyst systems, therefore, the data should be read in conjunction with the source and strength of light.

2.11 Oxidants in the Photochemical reactions

Photochemical oxidants are essential in enhancing the efficiency of photocatalysis, particularly in the degradation of persistent organic pollutants like PFAS. Activated by UV light, oxidants such as persulfate and hydrogen peroxide generate highly reactive radicals, including $OH^\bullet$ and $SO_4^{-\bullet}$ radicals. These radicals are highly effective in breaking down complex PFAS molecules into simpler, less harmful compounds, significantly increasing the mineralization rates. In addition to accelerating reaction kinetics, the present of oxidants improves the overall degradation process, [67]. For example, persulfate has been shown to enhance the dissociation of PFOA, resulting in higher mineralization rates compared to processes without oxidants. Moreover, oxidants help reduce the recombination of photogenerated electrons and holes in photocatalytic systems, enabling more electrons and holes to participate in degradation reactions, further improving mineralization, [68], [69], [70]. Oxidants also facilitate the sequential degradation of PFAS into shorter-chain perfluorinated acids, which are more easily mineralized, improving overall efficiency. When combined with photocatalysts, oxidants can lead to synergistic effects, as demonstrated by the use of phosphor-tungstic acid with UV light, which has shown improved PFAS mineralisation in water treatment. These strategies underscore the importance of photochemical oxidants in optimizing photocatalytic processes for environmental remediation, [32].

The application of photochemical oxidants has gained considerable attention for the degradation of recalcitrant contaminants, such as PFAS, which are resistant to conventional treatment methods. Uwayezu et al., [71], found that combining ultraviolet (UV) light at 185 and 254 nm with persulfate effectively degrades PFAS by breaking the car bon-fluorine bonds. This approach generates reactive $SO_4^{-\bullet}$ radicals, facilitating the breakdown of PFAS into less harmful by-products in both controlled and real-world water samples. However, the presence of competing contaminants, such as nitrate and chloride, reduces degradation efficiency by scavenging $SO_4^{-\bullet}$ radicals. These findings highlight the importance of optimizing persulfate concentrations and operational parameters to enhance performance in complex wastewater matrices, [71]. Esfahani and Mohseni, [72],

investigated PFOS degradation using vacuum ultraviolet (VUV) irradiation combined with a fluence-based approach, quantifying degradation by total energy absorbed. VUV irradiation at 185 and 254 nm generated high- energy photons, breaking C-C and C-F bonds with hydrated electrons (e_{ag}^-) playing a key role. The addition of sulfite enhanced degradation rates, while advanced mass spectrometry analyses revealed wavelength- specific effects, with 185 nm improving fluorine recovery. Optimizing parameters such as sulfite concentration, pH, and dissolved oxygen further enhanced system efficiency. These findings highlight the potential of photochemical oxidation for PFAS remediation and the need for parameter optimization in complex matrices, [72].

2.12 Semiconductor based Photocatalysis for Charge Transfer Mechanisms

Semiconductors have emerged as pivotal materials for the photo catalytic degradation of PFAS due to their unique electronic properties and tuneable characteristics, [73]. A semiconductor's bandgap, defined as energy differential between its conduction and valence band, is a key determinate of its photocatalytic performance, [74]. Optimizing the bandgap facilitates efficient electron excitation under light irradiation, leading to the formation of ROS essential for PFAS degradation. This can be achieved through precise modifications to the semiconductor's size, structure, and composition, enabling enhanced photocatalytic activity. Upon light activation, semiconductors generate electron-hole pairs, which interact with water and oxygen molecules to produce ROS, such as $OH^{\bullet}$ and $O^{-2\ \bullet}$ ions radicals. These species play a critical role in cleaving the robust carbon-fluorine (C–F) bonds present in PFAS molecules, [75]. The incorporation of metal nanoparticles, such as silver, into semiconductor frameworks further enhances photocatalytic performance by introducing electron traps and facilitating increased ROS production, [76].

Recent studies have highlighted the potential of semiconductor-based photocatalysts for PFAS degradation, particularly metal oxides with reduced bandgaps that extend light absorption into a broader spectrum. In_2O_3 and Ga_2O_3 have demonstrated promising performance for PFOA degradation. Nano structured metal oxides with reduced bandgaps, such as In_2O_3, extend light absorption into a broader spectrum, further improving photocatalytic activity under diverse irradiation conditions. Additionally, the introduction of foreign metals on semiconductor sur faces promotes charge carrier separation, minimizing electron-hole recombination and sustaining the photocatalytic process, ultimately resulting in more efficient PFAS degradation, [32], [75], [77].

To evaluate the practical applicability of metal-modified semiconductors, Wen et al., [78], synthesized Fe-doped zeolite using zeolite β via a wet-impregnation method and investigated its PFAS degradation under UV light. Complete degradation of PFOA and PFOS was achieved within 7 h, whereas GenX showed a lower removal efficiency of 79%. The limited degradation of GenX was attributed to its more stable molecular structure and stronger C-F bonds, which reduce its reactivity under photocatalytic conditions. Fe doping facilitated the formation of reactive species, such as radicals and oxidants, that effectively cleave C-F bonds in PFOA and PFOS. However, these reactive species were significantly less effective against the more recalcitrant structure of GenX. While 254 nm UV irradiation played a significant role in driving the degradation, GenX likely requires higher energy input for effective breakdown. These findings suggest that although Fe-doped zeolites offer promise for PFAS degradation, further optimization is necessary to address persistent and structurally resistant compounds such as GenX, [78]. These findings emphasize the potential of semiconductor-based photo catalysts as effective tools for PFAS remediation, while also highlighting the necessity for continued research to enhance their performance against diverse PFAS structures. Li et al., [79], developed a composite photocatalyst, Fe/TNT@AC, by combining iron-modified titanate nanotubes with activated carbon to enhance PFAS degradation. Under UV light, the material generates electron–hole pairs that produce reactive species, such as $OH^{\bullet}$ and perfluoroalkyl radicals, which drive oxidative and decarboxylation reactions to break strong C-F bonds in compounds like PFOA. This system achieved over 90% PFOA removal and 62% defluorination within 4 h, due to the synergistic effects of adsorption and photocatalysis. The composite also exhibits self- regeneration, maintaining performance over multiple cycles while minimizing the need for chemical regenerants. These features make Fe/TNT@AC a promising and sustainable approach for PFAS removal in water treatment. Fe/TNT@AC exhibits a notable self-regeneration capability owing to its integrated “concentrate-and-destroy” mechanism, in which PFAS molecules are initially adsorbed onto the activated carbon surface and subsequently degraded via photocatalysis under UV irradiation. This process not only eliminates contaminants but also re stores active sites without requiring chemical regenerants. The composite maintains high structural stability, showing negligible titanium leaching and minimal iron loss (~2.53wt%)

across multiple cycles. Furthermore, the material sustains over 99% PFOA removal efficiency through repeated adsorption–degradation cycles, supported by the progressive defluorination of intermediates that enhances catalytic activity. These features underscore Fe/TNT@AC as a sustainable and cost-effective photocatalytic adsorbent for long-term PFAS remediation in water treatment systems, [79].

In a study performed by Qanbarzadeh et al., [80], hexagonal boron nitride (hBN) was investigated as a photocatalyst for PFAS degradation, hBN adsorbs PFAS mainly via hydrophobic interactions rather than electrostatic forces and this interaction is crucial because it allows for the effective clustering of PFAS molecules on the hBN surface, facilitating their degradation. hBN achieved over 99% PFOA degradation in 15 min and 65% PFOS degradation in 1 h using a 5 liters UVC/VUV photoreactor under realistic water conditions, outperforming previous photocatalysts, [80]. Furthermore, boron nitride (BN) has been explored as a PFAS photocatalyst, overcoming its wide bandgap limitation through surface defects introduced by ball milling. Duan et al., [81], explored boron nitride (BN) for PFOA degradation under UVC light, despite its wide band gap being considered a limitation. Remarkably, BN outperformed TiO_2, achieving degradation rates up to four times higher. This success was linked to a hole-initiated reaction pathway and surface defects introduced by ball milling, enhancing UVC light absorption. BN efficiently degraded PFOA, releasing 52% of fluorine as fluoride ions in 240 min and maintained performance over multiple cycles unlike TiO_2. In simulated drinking water, BN achieved a 60% PFOA degradation rate, demonstrating practical potential. These findings highlight the promise of photocatalysts like Fe-doped zeolite, Fe/TNT@AC, and BN while emphasizing the need for innovations in material design and process optimization to tackle real-world water treatment challenges, [81]. These advancements underscore the potential of semiconductor-based photocatalysts in PFAS remediation, while also highlighting the necessity for further optimization to improve performance across diverse PFAS structures. The incorporation of heterojunctions, metal modifications, and nano-structuring strategies remains critical for enhancing charge carrier separation, extending light absorption, and maximizing ROS generation.

2.13 Statistical Analysis

ANOVA analysis of variance between experimental data was performed to detect F and P values. The ANOVA test was used to test the differences between dependent and independent groups, [82]. Comparison between the actual variation of the experimental data averages and standard deviation is expressed in terms of F ratio. F is equal (found variation of the date averages/expected variation of the date averages). p reports the significance level, and d.f indicates the number of degrees of freedom. Regression analysis was applied to the experimental data in order to determine the regression coefficient R^2, [83]. The aforementioned test was performed using Microsoft Excel Program.

All experiments were carried out three times and the results are given as the means of triplicate samplings. The data relevant to the individual pollutant parameters are given as the mean with standard deviation (SD) values.

2.14 Reusability studies for In2O3/Ga2O3 Heterogenous Nanocomposite

Reusability is crucial for the commercial application of photocatalysts. The reusability of the In_2O_3/Ga_2O_3 nanocomposite was evaluated through photocatalytic degradation of PFOS and PFAS under sunlight for 100 cycles. The matrix contained 0.75 mg/l In_2O_3/Ga_2O_3 nanocomposite and 1000 mg/l PFOS and PFAS, maintained for 5 min. In each cycle, the recovered nanocomposite was isolated from the reaction medium using a pump. After treatmen with distilled water containing 1% NaCl, approximately 2 liters of the nanocomposite mixture was exposed to alkaline water. The nanocomposite was used 100 times, and PFOS and PFAS concentrations were measured. Additionally, the recovered In_2O_3/Ga_2O_3 nanocomposite was weighed to check for mass loss, and its continued usability was verified through 100 cycles.

3 Results and Discussions

3.1 XRD Analysis Results

Powder XRD analysis was employed to rule out the formation of crystalline agglomerates greater than the typical detection limit of around 2 nm. XRD images of In_2O_3, Ga_2O_3 and In_2O_3/Ga_2O_3 nanocomposite to indicate calcination at 500°C in 20%O_2 for 3 h. In_2O_3 (27 wt%) in In_2O_3/Ga_2O_3 and Ga_2O_3 (19 wt%) in In_2O_3/Ga_2O_3 were synthesized via incipient wetness impregnation (IWI) (Figure 5). The XRD of the as-deposited Ga_2O_3 show no crystalline phase, thus being XRD amorphous (Figure 5). Moreover, the broad reflection at 21.80^o (2θ), which accounts for amorphous In_2O_3/Ga_2O_3, and the diffractograms provide no defined intensity features.

* Figure 5 can be found in the Appendix section.

XRD pattern of In_2O_3/Ga_2O_3 displays a number of peaks at 2θ = 20.50°, 30.40°, 36.11°, 52.37°, and 60.02°, respectively, corroborated respectively to (221), (222), (400), (440) and (622) lattice planes of monoclinic WO_3 (JCPDS # 08–0459) (Figure 5a).

X-ray amorphous GaO_x films were also deposited by Donmez et al., [84], until 500 cycles of Trimethylgallium ($Ga(CH_3)_3$ / O_2-plasma. In their case, the transition to crystalline Ga_2O_3 only occurred under annealing in N_2 gas. However, calcination of the three-cycle sample at 500°C (20% O_2) did not result in the formation of detectable crystallites. This underlines the stability and dispersion of the layer despite a mass-fraction of 35 wt% GaO_x. As a reference, 19 wt% Ga_2O_3 was supported on silica using the incipient wetness impregnation method with gallium nitrate. After calcination at 500°C, the impregnated sample exhibited broad signals characteristic of α- or β-Ga_2O_3, [85].

In the case of InO_x atomic layer deposition, the x-ray diffractograms exhibited no distinct reflections, being also XRD amorphous (Figure 5). On the contrary, an additional phase centered around 31.6° (2θ) emerged in the diffractogram of the three-cycle sample after calcination. It lies close to the reflection of the (222) plane of cubic In_2O_3 typically located around 30.6° (2θ), [86]. It might also be an indication for the (200) facet of $In(OH)_3$ lying between 31 and 32, [87]. However, the new phase might still be nanocrystalline and only the starting point for the formation of $In(OH)_3$ or In_2O_3 crystallites.

These findings agree with the literature, as Elam et al., [88], showed that defined reflections of the (222) plane of In_2O_3 only appear upon 800 cycles after annealing or at higher deposition temperatures. For comparison, 27 wt% In_2O_3 was supported on silica via incipient wetness impregnation and calcined at 500°C (In_2O_3). The impregnated sample showed sharp reflections characteristic of cubic In_2O_3. Therefore, the impregnated In_2O_3 was clearly agglomerated and crystallized, while it is provided a more dispersed InO_x species.

3.2 EDX Analysis Results

EDX-mappings of the atomic layer deposition samples of In_2O_3 and Ga_2O_3 on In_2O_3/Ga_2O_3 nanocomposites demonstrate the opposite, without changes in morphology compared to the underlying support material (Figure 6). Consequently, the atomic ratios between silicium and indium varied significantly between 25:1 and 2:1 within the mapping (Figure 6a). In the case of Ga_2O_3, the atomic ratio of Ga_2O_3 and Ga varied between 6/1 to 8/1 in selected areas after one cycle (Figure 6b).

* Figure 6 can be found in the Appendix section.

The ratio of element composition was determined by EDS analysis. Figure 6 shows the EDS spectrum and the atomic ratio of the thin film. The In/Ga ratios with In_2O_3 target powers of 40 W were 69.80% in the In_2O_3/Ga_2O_3 nanocomposites (Figure 6c). Spectrums of oxygen, gallium and indium were measured at 64.31%, 21.02% and 14.67%, respectively, in the In_2O_3/Ga_2O_3 nanocomposites (Figure 6c). We can observe that when the In_2O_3 target power increases, the ratio of indium to gallium also increases, which means that the proportion of indium increases, and the conductivity will improve.

3.3 XPS Analysis Results

XPS analysis was conducted to determine the oxidic species of as-deposited In_2O_3 and Ga_2O_3 on In_2O_3/Ga_2O_3 nanocomposites (Figure 7). The peaks associated with the electron binding energies of the spin-orbit-coupled In3d orbitals (J=3/2 and 5/2) are shifted to the lower binding energy with increasing cycle number (Figure 7a). After oneatomic layer deposition cycle of InO_x, the $In3d_{5/2}$ signal appeared at binding energy of 445.1 eV which can be assigned to $In(OH)_3$ (445.2 eV, [89]). After two cycles, the peak was located at 444.9 eV and after three cycles at 444.8 eV, while the latter is matching the binding energy as in In_2O_3 (444.7 eV, [89]). Therefore, the deposited InO_x species might transition from $In(OH)_x$ to In_2O_3 species with increasing cycle number.

* Figure 7 can be found in the Appendix section.

Additionally, increasing content of In_2O_3 could be observed within the O1s region (Figure 7b). The related signal was fitted into two peaks at about 532.2 eV and 530.2 eV after the third cycle. The former can be assigned to the oxygen of Indium (O-ln), [90], and the second corresponds to oxygen as in In_2O_3 (O-In), [91]. Thereby, the ratio between In_2O_3/Ga_2O_3 and In_2O_3-related oxygen increased from 20:1 after the first cycle to 3:1 after the third cycle.

The photoemission spectra of the Ga3d region showed two overlapping peaks on In_2O_3/Ga_2O_3 (Figure 7c). One can be assigned to Ga, bound with oxygen as in Ga_2O_3, located at 20.8 eV. The second derives from the O2s orbital, around 24.8 eV, [92]. With increasing Ga_2O_3 cycle number, the intensity of the Ga_2O_3-related peak (Ga3d) increases in relation to the O2s peak. Decreasing contribution of the O2s signal might be the result of the increased degree of

coverage of substrate oxygen by gallium oxide species on In_2O_3/Ga_2O_3 nanocomposites. An alteration of hydroxylated Ga content was not observed (typ. around 19.6 eV), [93].

The peaks associated with the electron binding energies of the spin-orbit-coupled In3d orbitals (J=3/2 and 5/2) are shifted to the lower BE with increasing cycle number (Figure 7b). After one atomic layer deposition cycle of InOx, the $In3d_{5/2}$ signal appeared at BE of 445.1 eV which can be assigned to $In(OH)_3$ (445.2 eV, [89]). After two cycles, the peak was located at 444.9 eV and after three cycles at 444.8 eV, while the latter is matching the binding energy as in In_2O_3 (444.7 eV, [89]). Therefore, the deposited InO_x species might transition from $In(OH)_x$ to In_2O_3 species with increasing cycle number. Additionally, increasing content of In_2O_3 could be observed within the O1s region (Figure 7c). The related signal was fitted into two peaks at about 532.2 eV and 530.2 eV after the third cycle. The former can be assigned to the oxygen of silica (O-Si) and the second corresponds to oxygen as in In_2O_3 (O-In). Thereby, the ratio between Si and In_2O_3-related oxygen increased from 20/1 after the first cycle to 3/1 after the third cycle.

3.4 FTIR Analysis Results

The question arises where the carbon species is deposited and of which nature it is. In addition to the typical absorption bands of In_2O_3/Ga_2O_3 nanocomposites, the FTIR spectra of In_2O_3/Ga_2O_3 showed no features in the C - H stretching regions (Figure 8). The silanol band around 3740 cm^{-1} and 977 cm^{-1} decreased in intensity with higher cycle numbers as Trimethylindium [$(In(CH_3)_3$], chemisorbed on In-OH. Still, the silanol-related bands persisted as weak shoulders after the third cycle. This indicates unreacted ln-OH groups that might be sterically blocked or in the bulk.

* Figure 8 can be found in the Appendix section.

In_2O_3 wavenumbers are shown at 1100 cm^{-1}, 985 cm^{-1}, 760 cm^{-1}, 500 cm^{-1}, respectively, after 3 cycles on In_2O_3/Ga_2O_3 nanocomposites using TMX (X=G, I) and water at 150°C (Figure 8a).

Ga_2O_3 wavenumbers are determined at 1200 cm^{-1}, 977 cm^{-1}, 742 cm^{-1}, 596 cm^{-1} and 562 cm^{-1}, respectively, after 3 cycles on In_2O_3/Ga_2O_3 nanocomposites using TMX (X=G, I) and water at 150°C (Figure 8b).

3.5 ICP-OES Analysis Results

Additionally, assuming a stoichiometry of $Metal_2Oxide_3$ (M_2O_3) (M=Ga or In), the estimated metal contents were 14.50wt%(Ga) and 23.10wt%(In) after the first atomic layer deposition cycle in the magnetic suspension balance (Table 2). The contents determined by ICP-OES were 14.60wt%(Ga) and 21.10wt%(In) which points to a stoichiometry of $Metal_2Oxide_3$ for Ga_2O_3. Therefore, condensation of $Ga(OH)_2$ species might already occur in the first cycle. However, the mass fraction of indium is over estimated for the first cycle, indicating that the actual deposited species has a lower mass fraction of indium than in In_2O_3.

* Table 2 can be found in the Appendix section

Considering chemisorbed $In(OH)_2$ instead delivered an estimated indium content of 21.50wt% which matches the measured content of 21.10wt%(In). For subsequent cycles, the estimated indium contents have a better fit to ICP-OES when In_2O_3 is assumed. Hence, chemisorbed $In(OH)_2$ might resist condensation and do not collapse towards oxidic species in the first cycle. In subsequent cycles, the formation of In_2O_3 is favoured during the reaction with Trimethylindium [$(In(CH_3)_3$], and water (Table 2).

Thermogravimetric and ICP-OES data suggested a stoichiometry of Ga_2O_3 being present already after the first cycle. In the case of InO_x, the transition from $In(OH)_x$ to In_2O_3 with increasing cycle number was observed by XPS and confirmed by calculations based on thermogravimetric data and ICP-OES.

3.6 STEM Analysis Results

STEM images revealed agglomeration of the impregnated In_2O_3 and Ga_2O_3 samples with particle sizes between 20 and 100 nm (Figure 9). The calculated crystal diameter based on the 35.5° (2θ) reflection was approximately 21 nm, applying the Debye–Scherrer equation (FWHM =0.82° (2θ)) (Figure 9).

* Figure 9 can be found in the Appendix section.

The STEM images of In_2O_3, Ga_2O_3 and In_2O_3/Ga_2O_3 nanocomposites were shown in Figure 9a, 9b and 9c. The impregnated In_2O_3/Ga_2O_3 nanocomposites samples with particle size between 40 and 120 nm (Figure 9c). The calculated crystal diameter based on the 41.20° (2θ) reflection was nearly 33 nm, applying the Debye-Scherrer equation (FWHM=0.94° (2θ) (Figure 9c).

Despite their high mass fractions, the oxides were found to be highly dispersed and amorphous by STEM EDX-mappings and XRD. Additionally, the processes led to specific surface areas of 260–340 m^2/g for GaO_x and 140–280 m^2/g for InO_x determined by N_2 physisorption analysis. The layer thicknesses were

estimated based on thermogravimetric data which revealed a grows per cycle on average (gpc) of 0.7 Å for GaO_x and 1.5 Å for InO_x.

3.7 FESEM Analysis Results

FESEM analysis were applied to In_2O_3 (Figure 10a) and Ga_2O_3 (Figure 10b) and In_2O_3/Ga_2O_3 (Figure 10c) nanocomposites after photodegradation of PFOA and PFOS, respectively. The morphologies of the calcined samples, i.e. as-obtained In_2O_3 products were also observed by FESEM. Figure 10 shows that the In_2O_3 porous microsphere with a diameter of 180 nm is built of several nanoparticles with diameters of 5–15 nm, which indicates that the nanoparticles consisting microsphere aggregated during calcination and became bigger. The obtained In_2O_3 nano-cubes have a side length of about 40–150 nm, which indicates that during calcination most of $In(OH)_3$ nano-cubes collapsed into smaller fractures due to loss of water and the interstices in $In(OH)_3$ nano-cubes (Figure 10a). Although, In_2O_3 samples obtained from $In(OH)_3$ nano-cubes agglomerated and their morphology distorted, many particles still had a cube-like shape as indicated by white arrows in Figure 10a. Hence, the morphologies and structures of$In(OH)_3$ precursors play an important role in the transformation from $In(OH)_3$ to In_2O_3 during calcination.

* Figure 10 can be found in the Appendix section.

The pore-size distribution obtained from the isotherm indicates the existence of a number of pores around 6 nm in the sample. These pores presumably arise from the spaces among nanoparticles consisting the microspheres, as observed in FESEM image (Figure 10a). The larger pores around 25 nm are attributed to the spaces among microspheres. TheBrunauer–Emmett–Teller (BET) surface area of In_2O_3 microspheres was found to be 42.3 m^2/g. While the BET values of In_2O_3 nano-cubes and nanoplates were 13.60 and 18.90 m^2/g, respectively. The relatively higher BET surface area of the microspheres further confirms that the In_2O_3 microspheres have a porous structure. Usually, a high surface area can offer more active adsorption and reaction centers, and thus has a beneficial effect on the activity (Figure 10a).

The average crystallite sizes of In_2O_3 nanoparticles determined from XRD patterns were 100 nm and 20 nm respectively, which are larger than FESEM measured values of 90 nm (i.e., diameter of nanorods) and 8 nm (i.e., nanoparticles) due to antistrophic strains (Figure 10a).

The average crystallite sizes of-Ga_2O_3 nanoparticles measured from XRD patterns were 120 nm and 32 nm, respectively, which are larger than FESEM measured values of 100 nm (i.e., diameter of nanorods) and 10 nm (i.e., nanoparticles) due to antistrophic strains (Figure 10b).

The FESEM images of In_2O_3/Ga_2O_3 nanocomposites were seen at Figure 10c after photodegradation of PFOA and PFOS, respectively. The average crystallite size of In_2O_3/Ga_2O_3 nanocomposites determined from XRD patterns were 200 nm and 50 nm, respectively, which are larger than FESEM obtained values of 125 nm and 40 nm because of antistrophic strains (Figure 10c).

3.8 PL Spectrum and Oxygen Vacancies in In_2O_3/Ga_2O_3 Nanocomposite

PL spectrum of In_2O_3/Ga_2O_3 nanocomposite would exhibit emissions relative to various defects. The excitation wavelength was 269.0 nm, and the PL spectrum was shown in Figure 11.

* Figure 11 can be found in the Appendix section.

A broadband emission with a strong peak at 468.1 nm was observed, then the spectrum fitted with Gaussian function, corresponding peaks at 328.0, 359.1, 469.1, 549.7 and 608.2 nm. The emissions at 325.0 and 358.1 nm originated from the recombination between the lowest donor oxygen vacancies and the maximum energy level of the valance band. The emissions peaks at 469.1 and 548.7 nm were attributed to transitions from the donor band due to oxygen vacancy to the acceptor band due to gallium vacancy called donor–acceptor pairs), [94]. Other impurities in the growth caused the emission at 609.2 nm. The PL spectrum confirmed many oxygen vacancies in the In_2O_3/Ga_2O_3 nanomaterials due to the broad emissions, consistent with the stoichiometric proportion illustrated by the EDS results and XRD pattern refinement. The sensing mechanism of the In_2O_3/Ga_2O_3 nanomaterials is based on the adsorption and desorption of oxygen gas, which lead to a change in the resistance of the nanocomposite, [95]. Generally, In_2O_3/Ga_2O_3 nanomaterials present n-type conductivity due to oxygen vacancies, [95], whose amount significantly affects the sensitivities of the nanocomposites. The oxygen species, such as O, O_2, and O_3, [96], trap the electrons presenting in the conducting band of the In_2O_3/Ga_2O_3 nanomaterials. This phenomenon leads to electron depletion on the surface, causing an increase in the resistance of the nanocomposite. However, the amount of oxygen species was limited, and the time interval in response and recovery was not rapid. All these decreased can be affected the sensitivity of nanocomposite. As it was well known, the carrier concentration in In_2O_3/Ga_2O_3 material could be rapidly and extensively modulated

by the ultraviolet light due to quickly electron-hole generation and recombination. In the study performed by Gou et al., [94], it was investigated the PL of Ga_2O_3. The excitation wavelength for the aforementioned nanocomposite was recorded as was 261.0 nm. A broadband emission with a strong peak at 467.1 nm was observed, then the spectrum fitted with Gaussian function, corresponding peaks at 324.0, 356.1, 467.1, 543.7 and 601.2 nm. The emissions at 324.0 and 356.1 nm originated from the recombination between the lowest donor oxygen vacancies and the maximum energy level of the valance band. The emissions peaks at 469.1 and 548.7 nm were attributed to transitions from the donor band due to oxygen vacancy to the acceptor band.

Generally, the resistances of nanocomposites increased due to carrier depletion by two ways. One is that an oxygen molecule traps an electron forming an oxygen ion. The other is that an oxygen ion recombines with a photogenerated hole and releases an oxygen molecule. In both processes, the amount of the carrier decreases, [95]. The adsorption and desorption of an oxygen molecule under the ultraviolet light illumination were written as the following reactions Eq. 17, Eq. 18, Eq. 19, Eq. 20, Eq. 21, Eq. 22:

$$O_2(ads) + e^- \rightarrow O_2^-(ads) \quad (17)$$

$$O_2^-(ads) + e^- \rightarrow 2O^-(ads) \quad (18)$$

$$O^-(ads) + e^- \rightarrow O^{2-}(ads) \quad (19)$$

$$O_2^-(ads) + hole^+ \rightarrow O_2(g) \quad (20)$$

$$O^{2-}(ads) + 2hole^+ \rightarrow \frac{1}{2}O_2(g) \quad (21)$$

$$O^-(ads) + hole^+ \rightarrow \frac{1}{2}O_2(g) \quad (22)$$

In the chemical reactions, ads are the abbreviation of adsorption, the sign of g means gas. The responsivity of nanocomposite was defined as; $(R_{UV}-R_{dark})/R_{dark}$, Where, RUV refers to the resistance under ultraviolet light, and Rdark refers to the resistance without ultraviolet illumination. We tuned ultraviolet light intensity by controlling the power supply.

Fig. 12: a shows the responsivity of the In2O3/Ga2O3 nanocomposite at various oxygen concentrations under darkness, 3.0, 6.0 and 12.0 V ultraviolet light. Fig. 12b exhibits the responsivity to 50 ml oxygen injected into a sealed box under various ultraviolet light intensities, and Fig. 12c presents the responsivity to the diverse concentrations of oxygen under 12.0 V ultraviolet light. The In2O3/Ga2O3 nanocomposite was observed to have a weak response to oxygen gas without ultraviolet light. With the intensities increase of ultraviolet light illumination, the response to oxygen gas gradually improved. It confirmed the ultraviolet light illumination promoted the electron-hole recombination

* Figure 12 can be found in the Appendix section.

After the analysis of XRD pattern and Rietveld refinement, the obtained sample was monoclinic crystalline In_2O_3/Ga_2O_3 nanocomposite. In terms of SEM images, the In_2O_3/Ga_2O_3 nanomaterials nanocomposite were predominantly rod shaped, with a width in the hundreds of nanometers and a length in the tens of microns. The surface of the rods was smooth, while the cross-section was flat, indicating that the nanorods would be an ideal fit for the interdigitated electrodes. EDS showed that the material contained Ga, O, and Au, and the atomic number ratio of Ga and O was close to 2/3, with a slight excess of Ga, consistent with the evaluation of XRD refinement calculation. PL spectrum showed broad band emission, reflecting many oxygen vacancies in In_2O_3/Ga_2O_3 nanocomposite, consistent with the previous EDS and XRD results. The sensitivity of In_2O_3/Ga_2O_3 nanocomposite was improved significantly due to photogenerated electron-hole caused by ultraviolet light illumination. Both adsorption and desorption depleted carries resulting in the resistance of the sensors increasing.

3.9 Charge Transfer Mechanisms of In_2O_3/Ga_2O_3 Nanocomposite

3.9.1 Electrical Properties: DC Conductivity

Temperature dependencies of dc conductivity of In_2O_3/Ga_2O_3 nanocomposite samples with nanocrystals different in sizes are presented in Figure 13.

* Figure 13 can be found in the Appendix section.

It can be seen that the $\sigma_{dc}(T)$ dependencies consist of two specific regions. The first one occupies a temperature region from ~210°K to 300°K where the

conductivity increases with the rise in temperature. This may suggest that a simple thermal activation process dominates the electrical conduction in the In_2O_3/Ga_2O_3 samples. For the thermally activated band conduction, the conductivity (σ_{dc}) can be expressed as Eq. 23:

$$\sigma_{dc} = \sigma_0 exp(-E_A/k_B T) (23)$$

Where, E_A denotes the thermal activation energy of electrical conduction, σ_0 represents a parameter depending on the semiconductor nature and k is the Boltzmann constant.

The conductivity decrease and the activation energy increase are observed with the reduction of the nanocrystal size (the activation energy values are represented in Table 3).

* Table 3 can be found in the Appendix section.

The dependence described by Eq. 23 is typical for charge carrier transport over delocalized states in semiconductors, [97]. In the case of electron transport over the conduction band the thermal activation energy of electrical conductivity is defined as the energy difference between the bottom of the conduction band E_C and Fermi level E_F extrapolated to absolute zero temperature. Since there are potential barriers on the boundaries of nanocrystals the activation energy of conductivity E_A must also be defined by potential barriers' heights E_B. In the case of the existence of potential barriers at the grain boundaries and thermionic emission, [98], drift charge carrier mobility μ is thermally activated, [99], [100], (Eq. 24):

$$\mu \propto \mu_0 exp(-E_B/k_B T) (24)$$

Thus, the activation energy of conductivity can be expressed as Eq. 25:

$$E_A = (E_C - E_F)_0 + E_B (25)$$

Consequently, the decrease of the activation energy E_A with the increase of the nanocrystal size can be explained by Fermi level shift closer to the bottom of the conduction band and reduction of potential barriers' heights.

The decrease in the charge carrier concentration and mobility leads to the decrease of the electrical conductivity according towhere e is the electron charge, n is the charge carrier concentration and μ is the electron mobility.

It is possible that electrons can prefer to move to a more energetically similar remote site. In this regime, the following conduction law is expected for the variation of the conductivity σ_{VRH} of disordered systems, [101], (Eq. 26):

$$\sigma_{VRH} = \sigma_0' exp[-(T_0/T)^s] (26)$$

Where, σ_0' is pre-exponential factor and T_0 is a characteristic temperature.

The value of the exponent s depends critically on the nature of hopping process. Hopping theory, [102], [103], predicts that $\sigma_0'(T)=\sigma_0' T^{-2s}$. When the VRH mechanism dominates the conduction, the condition $0 < s < 1$ is fulfilled. If the density of states around Fermi level is assumed to be constant, s becomes s=1/4 (Mott VRH).

Figure 14 shows the plot of against in the range of low temperatures ($T < 200^oK$ for In_2O_3/Ga_2O_3 nanocomposite -300, $T < 170^oK$ for In_2O_3/Ga_2O_3 nanocomposite -500 and $T < 160^oK$ for In_2O_3/Ga_2O_3 nanocomposite -700).

* Figure 14 can be found in the Appendix section.

This indicates that the conduction in nanocrystalline In_2O_3/Ga_2O_3 samples is governed by Mott's VRH conductivity instead of activated conductivity at high temperatures. It is caused by hopping conduction between localized states in the grain boundary space-charge region. The existence of the localized states for such a conduction process may be a consequence of imperfections associated with nanostructured samples.

Since the obtained activation energy values E_A are too small, the Fermi level is located close to the conduction band E_C. Therefore, the charge carrier transport takes place by the localized states at low temperatures, which are also close to the conduction band.

The values of Mott's characteristic temperature T_0 and the pre-exponential factor σ_0' are obtained considering the slopes and intercepts of the curves in Figure 14 and are given in Table 4.

The values of T_0 and σ_0' decrease with the increase in nanocrystal size. The characteristic temperature T_0 for a three-dimensional hopping transport is given by [101], [104], Eq. 27:

$$T_0 = \frac{16}{k_B a^3 N(E_F)} (27)$$

Where, k_B is the Boltzmann's constant, a is the localization length and $N(E_F)$ is the density of states at the Fermi level. As T_0 is inversely proportional to a^3, the degree of disorder of the systems reduces with lowering of T_0 — consequently, with the increase in

nanocrystal size. The values of $N(E_F)$ are calculated assuming that the localization length of the In_2O_3 is about 10 Å, [105], [106]. The values of $N(E_F)$ are given in Table 4.

The obtained values indicate that the density of localized states $N(E_F)$ at the Fermi level increases with the increase in nanocrystal size. The localized states may have different physical nature, for example, due to the introduction of impurities or defects in the crystal lattice associated with sample nanostructuring. We assume that in our case defects introduce the greatest contribution to the appearance of localized states. It's seen that the density of states at the Fermi level in the In_2O_3/Ga_2O_3 nanocomposite samples is different. Since we can't contend that the Fermi level for different samples is at the same distance from the conduction band bottom, these densities of states cannot be compared. That is, likely, for each sample, the density of states is determined in different energy points. Thus, the difference in the obtained values of $N(E_F)$ most likely can be an evidence of inhomogeneous distribution of the localized states in the band gap.

The average hopping distance R_{hop} between two sites and the activation energy W_{hop} are, [106], Eq. 28 and Eq. 29:

$$R_{hop} = \frac{3}{8}\left(\frac{T_0}{T}\right)^{1/4} a \quad (28)$$

$$W_{hop} = \frac{1}{4} k_B T \left(\frac{T_0}{T}\right)^{1/4} \quad (29)$$

The values of the R_{hop} and W_{hop} at T=150°K are also listed in Table 3. The average hopping distance and hopping energy increase with the decrease in nanocrystal size. Unfortunately, it is impossible to establish precisely the nature of the localized states from the conductivity analysis. The localized states associated with defects may be in the bulk nanocrystal as well as at the grain boundaries. The carrier transport occurs over them.

It is worth mentioning that the requirements $R_{hop}/a \geq 1$ and $W_{hop} \geq k_B T$, which are essential for the validity of Mott's VRH model, are clearly satisfied. This indicates that the conduction in the considered temperature range is due to VRH in the investigated samples.

3.9.2 Electrical Properties: AC Conductivity

The ability to gather various kinetic and mechanistic information has made impedance spectroscopy a favorite tool for material characterization. The impedance spectroscopy, which involves measurement of impedance Z with respect to frequency, can give details about the physical processes taking place in the material through their electrical analog, [107]. This coupled with structural characterization can yield a complete physical picture of the various phenomena occurring in the sample under different conditions. The most important advantage of these ac measurements is that they can distinguish individual contributions to electrical conduction arising from different regions like bulk, intergranular contact regions, grain boundaries, and electrode–sample interface regions whereas dc measurement shows only the overall effect of all these contributions. Besides, frequency dependencies of conductivity are different for the conductivity in the band of delocalized states and for transport due to jumping over localized states.

In Figure 15Cole–Cole plots of the In_2O_3/Ga_2O_3 samples obtained at temperature T=300°K are presented. To describe the impedance of polycrystalline semiconductors an equivalent circuit where resistance of the bulk material in the grains is connected in series with capacitance and resistance of nanocrystal grain boundaries connected in the parallel is generally used. But in our case due to the small nanocrystal size such representation may not be justified and we can't separately introduce parameters such as resistance of the grain bulk and their boundaries since the mean free path for electron scattering is large compared with the nanocrystal size, [103]. Thus we have proposed equivalent circuit model for the behavior observed in our samples and it is shown in the inset of Figure 15.

* Figure 15 can be found in the Appendix section.

R_s and C_s present the contribution to resistance and capacitance arising from the grain boundaries, and resistance R_c has been added to the parallel capacitance–resistance combination to represent the contribution of the electrode–sample interface to the resistance, [108]. The admittance Y=1/Z of this circuit can be written as, [109], Eq. 30 and Eq. 31:

$$Y = \frac{\left(1+\frac{R_C}{R_S}\right)\frac{1}{R_S} + R_C\omega^2 C_S^2}{\left(1+\frac{R_C}{R_S}\right)^2 + \omega^2 C_S^2 R_C^2} + i\omega \frac{C_S}{\left(1+\frac{R_C}{R_S}\right)^2 + \omega^2 C_S^2 R_C^2} \quad (30)$$

The conductivity being studied in the present work:

$$\sigma_{ac} = \frac{l}{S} Re(G) = \frac{l}{S} \frac{\left(1+\frac{R_C}{R_S}\right)\frac{1}{R_S} + R_C\omega^2 C_S^2}{\left(1+\frac{R_C}{R_S}\right)^2 + \omega^2 C_S^2 R_C^2} \quad (31)$$

The right inset of this figure represents Cole–Cole plot for the In_2O_3/Ga_2O_3-300 sample and the left inset of this figure represents an equivalent electric circuit.

The conductivity being studied in the present work where l is the thickness of the In_2O_3 samples and S is the contact area. Under the condition $R_s \gg R_c$ we get:

$$1)\ \sigma_{\propto}(\omega) = \frac{l}{S}\frac{1}{R_S}\ when\ \omega(R_C R_S)^{1/2}\ C_S < 1;$$

$$2)\ \sigma_{\propto}(\omega) \approx \frac{l}{S}\omega^2 R_C C_S^2\ when\ \omega R_C C_S < 1 < \omega(R_C R_S)^{1/2}\ C_S;$$

$$3)\ \sigma_{\propto}(\omega) = \frac{l}{S}\frac{1}{R_C}\ when\ \omega R_C C_S > 1$$

The frequency dependencies of conductivity obtained from the In_2O_3/Ga_2O_3 samples at T=300°K are presented in Figure 16. According to the cases considered above, the measured conductivity σ_{ac} at low frequencies reflects the sample bulk conductivity. One can see that the conductivity is independent of frequency in this case. This fact indicates that the transport of carriers takes place over delocalized states which corresponds to the above-mentioned assumptions that the electron transport at high temperatures occurs over the conduction band. At high frequencies the conductivity increases.

The frequency dependencies of conductivity in the temperature range corresponding to Mott's VRH model are presented in Figure 16.

* Figure 16 can be found in the Appendix section.

The frequency range is limited by the condition. Hopping conduction in low-frequency regime (below 100 MHz) is described by the power law, [110], (Eq. 32):

$$\sigma_{ac}(\omega) = \sigma_{dc}\left[1 + \left(\frac{\omega}{\omega^*}\right)^P\right] (32)$$

Where, we have written the equation in a form such that the crossover frequency marking the onset of ac conduction, ω*, is given by $\sigma_{ac}(\omega^*)=2\sigma_{dc}$. Eq. 32 is referred to as the Almond–West formula, [110].

As we can see in Figure 17 all spectra could be well approximated by Eq. 32. Exponent p≈0.6 for the In_2O_3/Ga_2O_3 -300 and In_2O_3/Ga_2O_3 -500 samples and p≈0.5 for the In_2O_3/Ga_2O_3 -700 sample. Although, the power frequency dependence of conductivity is not the direct proof of hopping conduction mechanism it can be regarded as a serious indication that transport processes could be associated with the hops of carriers over localized states, [101].

* Figure 17 can be found in the Appendix section.

We used random barrier model, [101], for a qualitative interpretation of our results. This model considers the particles that can only take positions on a simple cubic lattice, having equal energies, and ignore interactions between them. The electrons can only move by hopping between the nearest sites. In the extreme disorder limit, when the frequency of hops from a given lattice point to a neighbor point varies by several orders of magnitude, the frequency dependence of conductivity has a universal character: (Eq. 33) where (Eq. 34 and Eq. 35):

$$ln\sigma_{ac} = \frac{i\omega}{\sigma_{ac}}\left(1 + \frac{8}{3}\frac{i\omega}{\sigma_{ac}}\right)^{-1/3} (33)$$

$$\sigma_{ac}(\omega) = \frac{\sigma_{ac}(\omega)}{\sigma_{dc}} (34)$$

$$\tilde{\omega} = 2\pi\frac{\omega}{\omega^*} (35)$$

The frequency dependency of conductivity of the In_2O_3/Ga_2O_3 samples in dimensionless values is presented in Figure 18. The fact that experimental dots lay on the universal curve indicates the uniform hopping mechanism taking place in our samples. Thus, nanocrystalline In_2O_3/Ga_2O_3 can be regarded as a disordered system.

* Figure 18 can be found in the Appendix section.

The results of this study indicate that nanostructured In_2O_3/Ga_2O_3 exhibits two mechanisms of the charge carrier transport. At high temperatures conductivity is determined by the electron transport over the conduction band. In this case the conductivity decreases and the activation energy increases with the reduction in nanocrystal size. The observed increase in the activation energy can be explained by Fermi level shift toward the midgap energy and by the growth of potential.

At low temperatures the Mott conduction mechanism associated with the charge carrier transport over the localized states at the Fermi level has been established. In contrast to the case of high temperatures, when the conductivity is independent on frequency, the value of σ_{ac} varies with frequency in accordance with a power law.

3.10 Advantageous of Heterogenous Structure of In_2O_3/Ga_2O_3 Nanocomposites

Through the reaction with residual oxygen in the reaction system, Ga_2O_3 and In_2O_3 clusters are simultaneously formed and act as the nuclei for Ga_2O_3 and In_2O_3 nanowires. Then the heteroepitaxial growth of 1D Ga_2O_3/In_2O_3 nanowires occurs due to the lattice match between the two crystals at specific orientations. As aforementioned, the, [101], zone axis of the Ga_2O_3 nanowire is parallel to the, [101], zone axis of the In_2O_3 nanowire. At the same time, the excessive Ga_2O_3 clusters may deposit on the side surface of the formed Ga_2O_3 nuclei to ensure low energy growth, [110].

With an increase in reaction time, the present In_2O_3-decorated Ga_2O_3 heterostructures are formed. Typical SEM images of products obtained after different reaction times clearly indicate that the heteroepitaxial growth of 1D heterostructures takes place at very early stages and then finally yields a product with a high aspect ratio.

Field-effect transistors (FETs) based on individual In_2O_3-decorated Ga_2O_3 heterostructures were fabricated, and their electrical properties were studied. This is illustrated in Figure 19a.

* Figure 19 can be found in the Appendix section.

Fig. 19: b presents the gate-dependent drain-source current (Ids) versus voltage (Vds) curves recorded on a representative single FET device. The FET device exhibits notable gate dependence and is conductive, reaching a current of 3.4 μA with a Vds of 10 V and a gate volt-age (Vg) of 40 V. The nonlinear curves indicate that Schottky barriers form between the Ga2O3 and the heterostructure. With a positively increasing Vg (-40 V …… 40 V), the conductance of the heterostructure increases, revealing an n-type conductivity. It has been reported that the pure Ga2O3 nanowires are normally n-type semiconductors due to oxygen vacancies, [111], [112]

In this work, the In_2O_3-decorated Ga_2O_3 hetero-structures exhibit similar n-type semiconducting behavior. In addition, we also studied the electrical properties of the fabricated devices at different temperatures, in vacuum. Figure 19c displays Ids ≥ Vds curves measured from 300 to 10^oK with Vg =0 V. It can be seen that the conductance of a device decreases as the temperature decreases.

We further estimate the carrier concentration and mobility in the heterostructures. The conventional method to obtain such parameters is to analyze its field-effect behavior using a FET setup. However, herein the Schottky barriers play an important role in the electron transport and the FET model may result in an underestimate of the mobility. Considering the tunneling current to become dominant under a reverse bias in a low-dimensional system, thermionic field emission theory is proposed for analyzing the present semiconductor parameters from the two-terminal I - V curves, [113], [114].

In detail, the reverse-biased Schottky barrier dominates the total current Iin the intermediate bias regime of the Ids – Vds curve (Vg=0), Eq. 36:

$$\ln I = \ln(SJ) = Ln\ S + V\left(\frac{q}{kT} - \frac{1}{E_0}\right) + lnJ_S (36)$$

Where, J is the current density through the Schottky barrier, S is the contact area, Js is a slowly varying function of an applied bias, and $E_0 = E_{00} \coth(qE_{00}/kT)$ with $E_{00} = h/2[n/(m_n^* \varepsilon_s \varepsilon_0)]1/2$, n is the electron concentration, m_n^* and ε_s are the effective mass of an electron and relative permittivity of the material, respectively, and ε_0 is the permittivity of free space.

The logarithmic plot of a current I as a function of a bias V gives approximately a straight line with a slope q= (kT) - $1/E_0$, as shown in Figure 19d. Then n can be obtained via E_0, and the electron mobility can be calculated using $\mu = 1/(nqp\ )$, with p being the resistivity of the heterostructure, which can be estimated to be 0.49 ω.cm. Applying this procedure to the I-V curves and assuming the relevant physical constants, such as m_n^* and E_S (for Ga_2O_3, m_n^*= 0.347 m_e, ε_S =9.97; for In_2O_3, mn* =0.28 m_e, ε_S =8.86, mebeing the free electron mass 29-31), the electron concentration of the heterostructure is estimated to be (4.21-5.45) x10 ^{17} cm^3, and the electron mobility is calculated to be 22-28 cm^2/V.s.

The resistivity, electron concentration, and mobility in the synthesized In_2O_3/Ga_2O_3 nanocomposite was estimated to be 10.87 ω.cm., 1.77 x 10^{17} cm^3, and 3.2 cm^2/V.s, respectively. It clearly indicates that the In_2O_3/Ga_2O_3 heterostructures possess significantly lower resistivity (0. 49 ω.cm) (higher conductivity) compared with pure Ga_2O_3 nanobelts (10.87 ω.cm) as well as Ga_2O_3 nanowires (300-500 ω.cm. In addition, the electron concentration in an In_2O_3/Ga_2O_3 heterostructure is much higher than in a pure Ga_2O_3 nanobelt. The present carrier mobility in the In_2O_3/Ga_2O_3 heterostructures (24-31 cm^2/V.s, is about 1 order of magnitude higher than in a standard Ga_2O_3 nanobelt (3.19 cm^2/V.s) and is also larger than in normal Ga_2O_3 nanowires (6.56 cm^2/V.s), [115]. Therefore, on the basis of the above com-parison, it is believed that the electrical behavior of the present heterostructures is greatly modulated by the In_2O_3 nanowire decoration. In particular, the In_2O_3 nanowires likely participate in the electron transport to-gether with the Ga_2O_3 nanobelts.

We can conclude that In_2O_3/Ga_2O_3 heterostructures showed an enhancement of electron mobility and conductivity. It has been reported that nanostructures with lower resistivity have a better field-emission performance, which is due to the better supply of electrons to the emitting surface, [114].

Fig. 20: a shows the emission current density as a function of the electrical field (J-E plot) measured at different spacings (d) between the anode and a sample

* Figure 20 can be found in the Appendix section.

When the gap is increased from 0.13 to 0.78 mm, the turn-on field (E_{to}), which is defined as the field required to produce a current density of 9.98 μA/cm^2, decreases monotonously from 6.49 to 1.33 V/ μm (Table 4).

* Table 4 can be found in the Appendix section.

Therefore, the electrical study results imply that the heterostructure may be a valuable field emitter. In order to study the performance of the In_2O_3-decorated Ga_2O_3 heterostructures as a field emitter, field-emission properties were measured in a high vacuum of 6.0 x 10^{-6} Pa.

The current density at 6.4 V/μm was as high as 4.99 μmA/cm^2 at d=0.19 mm, and no current saturation is observed. It worth noting that the muchlower turn-on field and higher current density of field-emission have been obtained for the present hetero-structures, compared with either pure Ga_2O_3 nanostructures, [111], [116], [117], or In_2O_3 nanostructures, [118], [119], as summarized in Table 4. The data suggest that the newly prepared material is a highly valuable field-emitter that rivals previously reported ZnO, ZnS, SiC, Si, and AlN nanowires/nanobelts, [120]. The field-emission current⩾voltage characteristicswere further analyzed using the Fowler-Nordheim (FN) theory (Eq. 37 and Eq. 38).

$$J = (A\beta^2E^2/\emptyset)exp\left(-B\emptyset^{3}/_{2}/\beta E\right) \quad (37)$$

or

$$ln(J/E^2) = ln(A\beta^2/\emptyset) - B\emptyset^{3}/_{2}/\beta E \quad (38)$$

Where, A=1.58 A eV/V^2, B= 6. 99 x 10 ^{3} eV$^{3/2}$ V mμ^{-1}, β is the field-enhancement factor, and φ is the work function of an emitting material.

Fig. 20: b shows the FN plots with different vacuum gaps. The plots are approximately linear, indicating that the FN theory well fits the field-emission behavior of thesample. We can calculate β from the slope of the FN plots in Fig. 20b. Considering that the work function of Ga2O3 is 4.86 eV, β increases from 796 to 5060 under an increasing vacuum gap from 0.11 to 0.74 mm (Table 4). The β value is significantly larger than for other re-ported Ga2O3 or In2O3 nanostructures, as also illustrated in Table 5

* Table 5 can be found in the Appendix section.

β is an important parameter in describing field emis-sion. Generally, the β values are related to the emitter geometry, crystal structure, vacuum gaps, and spatial distribution of emitting centers. Structures with a higher aspect ratio would exhibit stronger field emissions from a given nanostructured material, [120], [121]. The re-lationship between β and d is crucial for fabrication field-emission devices. Figure 20c is a relationship of 1/β and 1/d. It shows that β obviously depends on d with a relationship of 1/ β -1/d. On the basis of the two-region field-emission model, we found that the experi-mental data are almost fitted to a straight line and can be approximated by 1/ β =h/d ± 1/ β_0, where h is a width of the field-emission region near the whisker surface and β_0 is the absolute amplification factor, which is intrinsically determined by the emitting surface and independent of h, and d is an applied voltage. By fitting the slope and intercept value, the hand β_0 can be determined as 139 nm and 4.99 x10^4, respectively. The value of β_0 is remarkably larger than that of a carbon nano tubes (CNT) on an Fe tip (β_0 =2.5 x 10^4) or a CNT film growing on a Si substrate (β_0 =7990), [122], ZnO nanorods grown on a Si sub-strate (β_0 =3798), [123] and aligned CdS nanocone arrays (β_0 =4938), [121], indicating excellent field enhancement in the present In_2O_3-decorated Ga_2O_3 structures.

3.11 Photodegradation Metabolites of PFOA and PFOS

During the heterogeneous photocatalysis process, long chain PFAS will be degraded into various shorter chain compounds e.g. perfluoroheptanoic acid (PFHpA), perfluorohexanoic acid (PFHxA), perfluoropentanoic acid (PFPeA), perfluorobutanoic acid (PFBA), and trifluoroacetic acid (TFA), as the main intermediates with In_2O_3 catalysts. Where the intermediates show a concentration increasing followed by declining with their concentrations (Table 6). The concentrations of all intermediates except PFHpA are under 5 mg/l after 5 min photodegradation.

The concentrations of PFHpA all increase initially and reach a plateau within 2-3 min followed by a decreasing trend. Of the 4 different catalysts tested, In_2O_3 NPNS and needle-like Ga_2O_3 show the best performance. During the photodegradation process, C - F bonds are destroyed so that the concentration of F as a product is increasing with the reaction time. The PFOA and PFOS intermediates we found in our experimental studies for In_2O_3/Ga_2O_3 nanocomposites after photodegradation process are shown in Table 6.

* Table 6 can be found in the Appendix section.

3.12 Effects of Operational Conditions on PFOA and PFOS Photodegradation Yields

The operating parameters effects on photocatalytic degradation in wastewater pollutant using $(In_2O_3)/(Ga_2O_3)$ Nanocomposite based photocatalyst are presented in this paper. The findings are used to identify and explain the individual influence of different parameters, such as the photocatalyst loading, initial pH, pollutant concentration, light intensity and temperature, on wastewater pollutants photocatalytic degradation.

3.12.1 Effect of In_2O_3/Ga_2O_3 Nanocomposite Loading

The maximum PFOA and PFOS photodegradation yields was detected at a 0.75 mg/l In_2O_3/Ga_2O_3 nanocomposite concentration as 99% and 98%, then the yields decreased to 85% and 84% with an increase of nanocomposite concentration to 1.20 mg/l at 1000 mg/l PFOA and PFOS concentrations after 5 min photodegradation time (Table 7). Extensive studies have been conducted signifying the pollutant photodegradation rate depends substantially on the catalyst loading. , An initial increase, followed by a decrease in the degradation rate can be observed in conjunction with an increase in the catalyst loading because of the light scattering and screening effects. A linear dependency holds true to a certain extent when the reaction rate starts to intensify until a limit is reached. Thereafter, it becomes independent of the In_2O_3/Ga_2O_3 nanocomposite photocatalyst concentration. This limit depends on the geometry and working conditions of the photo-reactor.

* Table 7 can be found in the Appendix section.

With an increase in the amount of In_2O_3/Ga_2O_3 nanocomposite above the saturation limit, particles agglomeration and accumulation are prompted. These subsequently reduce the photocatalyst surface area available for light absorption and eventually aggravate the photocatalytic activity. Therefore, an optimal dose of photocatalyst is important to achieve maximal photocatalytic degradation efficiency, [124]. However, some researchers have claimed that the direct comparison of the photocatalytic degradation rate in variations of catalyst loading is inconclusive because of differences in photon wavelengths, light intensity, radiation fluxes and working geometry, [125]. Despite, from the perspective of industrial applications, such as in wastewater treatment applications, where the presence of uncertainties is inevitable, the amount or concentration of In_2O_3/Ga_2O_3 heterogenous nanocomposite has seen a direct influence on the entire system efficiency at low concentrationa, [126].

A significant linear regression was detected between In_2O_3/Ga_2O_3 nanocomposite concentration and PFOA photodegradation yields. As the In_2O_3/Ga_2O_3 concentration was increased from 0.1 up to 0.75 mg/l the PFOA yields increased from 89% to 99% ($F=0.098$, $p=0.99$, $R^2=0.99$). Further increasing of the nanocomposite concentration from 1.2 mg/l up to 2.0 mg/l the PFOA yields decreasd from 85% to 76%. For these increasing values a significant linear regression was not observed between nanocomposite concentration and PFOA yiels ($F=9.67$, $p=0,65$, $R^2=0.67$). Similar results were detected for PFOS. As the In_2O_3/Ga_2O_3 nanocomposite concentration increased up to 0.75 mg/l, the PFOS yields increased from 86% to 98%. A significant linear correlation was detected between In_2O_3/Ga_2O_3 nanocomposite concentration and PFOA photodegradation yields% ($F=0.097$, $p=0.99$, $R^2=0.99$). Further increase of nanocomposite dose decrease the PFOA yields. A significant linear regression was not observed between nanocomposite concentration and PFOA yields ($F=9.69$, $p=0,63$, $R^2=0.66$).

3.12.2 Effect of pH

From Table 8 it can be seen that PFOA and PFOS contaminants have optimal pH levels for maximal photocatalytic degradations. The maximal photodegradation rates PFOA and PFOS weredetected at a neutral pH of 7.0. As the pH was increased from 2.0 up to 7.0 the yields in PFOA and PFOS increased from 66% up to 99%. A significant linear regression between increasing pH and pollutant yields were detected under these conditions ($F=0.098$, $p=0.004$, $R^2=0.99$). Under alkaline conditions the PFOA and PFOS photodegradation efficiencies decreased to 76% and 73%, respectively. F test istatistic showed that a significant linear correlation was not found between pollutant yields and alkaline pH levels ($F=9.98$, $p=1.310$, $R^2=0.69$).

* Table 8 can be found in the Appendix section.

Organic pollutants have differences in terms of speciation behaviour, water solubility and hydrophobicity. At a common pH, some compounds are uncharged, such as waste or natural water. This is different from the other compounds with varied speciation and physicochemical properties. Owing to the nature of In_2O_3/Ga_2O_3 photocatalyst used, variations in the operating pH led to variations in the isoelectric point or surface charge of the photocatalyst used. The pH value at which the surface charge is completely neutralized is known as the point of zero charge, or PZC. No many researchers have been using the PZC of In_2O_3, Ga_2O_3 and In_2O_3/Ga_2O_3 nanocomposite to study the effect of pH on the photocatalytic oxidation performance, [127], [128].

One of the effective operating parameters in heterogeneous photocatalytic processes as well as other photochemical processes is the pH as it affects the catalyst surface charge, the catalyst particle size and the conditions of the valence band and conduction band. Organic pollutants have differences in terms of speciation behaviour, water solubility and hydrophobicity. At a common pH, In_2O_3, Ga_2O_3 and In_2O_3/Ga_2O_3 nanocomposite have a PZCs of between 4.7 and 7.2, depending on its type and composition. At the PZC values, due to the absence of electrostatic force, the interaction between water contaminants and photocatalyst particles is minimal. At an operating pH less than the PZC, the photocatalyst surface is positively charged and it gently exerts an electrostatic attraction force towards the negatively charged compounds, [128]. This is specifically discernible when the concentration level of anionic organic compounds is low. On the contrary, at a pH more than the PZC, the photocatalyst surface is negatively charged which, subsequently exorcising anionic compounds. Furthermore, the solution pH plays a significant role in the photocatalytic oxidation and adsorption of pollutants because of the different pH effects on the surface charge density of In_2O_3/Ga_2O_3 photocatalyst. The surface ionization state of photocatalyst can be protonated under acidic conditions and deprotonated under alkaline conditions according to the following water equilibrium equations (Eq. 39 and Eq. 40):

$$pH < + pHPZC \quad InOH \leftrightarrow iOH^{+2} \quad (39)$$

$$pH > + pHPZC \quad GaOH \leftrightarrow InO^{+} + GaO + OH^{-2} \quad (40)$$

Typically, the PZC of In_2O_3 is about 6.29 while the PZC of Ga_2O_3 is approximately 7.03, [129]. In acidic media (pH < 6.25), the surface of In_2O_3/Ga_2O_3 photocatalyst is positively-charged, whereas it is negatively-charged in alkaline conditions (pH > 6.5). In addition, the pH of the solution has seen an effect on the $OH^{\bullet}$ radicals. There is a reaction between the induced holes and OH^- ions on the surface of the neutral pH of positive holes is important during the oxidation phases besides the high pH, [130], [131]. It would be expected that due to the presence of more available OH^- ions, the generation of $OH^{\bullet}$ radicals are higher on the surface of In_2O_3/Ga_2O_3. At a high pH, the procedure degradation efficiency will be decreased. With the change in pH, the degree of electrostatic attraction or repulsion between organic molecule ionic forms and the surface of photocatalyst can be varied. Hence, the pH can be used as the controlling variables for the enhancement or inhibition of organic pollutants degradation depending on one's need.

In addition, it is of great importance to determine the pK_a values of pollutants for a better prediction of the catalytic activity at a specific pH, because these affect the adsorption property of the catalyst as well as the stability of the pollutant's molecules. Basically, the pK_a value measures the acidity of pollutants present in the solution. The strength of acidity is said to be inversely proportional to the pK_a value, such that the weaker the acidity of a pollutant, the larger its pK_a. Therefore, to attain high photocatalytic reaction in wastewater treatment applications, it is imperative to perform suitable pH control strategies with the provision of the pK_a values, [130], [131].

3.12.3 Effect of PFOA and PFOS Concentrations

Up to 1000 mg/l PFOA and PFOS concentrations the yields was detected as 99% and 98%, respectively (Table 9). After this pollutant concentrations the yields decreased to around 73% and 76%. With increasing of substrate concentration up to a level, the probability of collision between pollutants and the surface of photocatalyst will be higher. Consequently, this increases the degradation rate due to very short lifetime of the $OH^{\bullet}$ radicals, which are responsible in oxidizing the organic pollutants, [132], [133]. However, when the substrate concentration increases to a certain extent, more intermediates will probably be generated and adsorbed on the photocatalyst surface since the photo-degradation process is a non-selective process and thus, the decomposition of the pollutants as well as the obtained intermediates will take place concurrently by the produced $OH^{\bullet}$ and $O^{-2\bullet}$ radicals. As a result, active sites on the photocatalyst are partially compromised and hence, incurring a slower adsorption rate, which eventually leading to a drop in the overall degradation rate. In short, it can be deduced that at low substrate concentrations, the

degradation rate is dependent on the number of catalytically active sites, [133], [134].

* Table 9 can be found in the Appendix section.

A significant linear regression was detected between PFOA concentration and PFOA photodegradation yields. As the PFOA concentration was increased from 50 up to 1000 mg/l the PFOA yields increased from 89% to 99% (F=0.099, p=0.98, R^2=0.99). Further increasing of the PFOA concentration from 1000 mg/l up to 1500 mg/l the PFOA yields decreased from 85% to 76%. For these increasing values a significant linear regression was not observed between nanocomposite concentration and PFOA yiels (F=9.67, p=0,65, R^2=0.67). Similar results were detected for PFOS. As the PFOS concentration increased up to 1000 mg/l, the PFOS yields increased from 76% to 97%. Under these conditions a significant linear correlation was detected between pollutant concentration and PFOS photodegradation yields (F=0.096, p=0.97, R^2=0.99). Further increase of PFOS dose decrease the PFOA yields. A significant linear regression between PFOS concentration and PFOS yields was not detected (F= 9.65, p= 0,62, R^2= 0.66).

Langmuir–Hinshelwood (LH) kinetics is the most commonly used kinetic expression to explain the kinetics of the heterogeneous catalytic processes. The Langmuir–Hinshelwood (LH) expression that explains the kinetics of heterogeneous catalytic systems. Langmuir–Hinshelwood (LH) kinetics is the most commonly used kinetic expression to explain the kinetics of the heterogeneous catalytic processes. The Langmuir–Hinshelwood (LH) expression that explains the kinetics of heterogeneous catalytic systems is given by Eq. 41:

$$\tau = -\frac{dC}{dt} = \frac{k_\tau . KC}{1+KC} \quad (41)$$

Where, τ represents the rate of reaction that changes with time. The term τ in Eq. (41) was represented in terms of initial reaction rate, τ_0, as a function of the initial PFOA and PFOS concentrations, C_0, or in terms of C_e, where C_e is the equilibrium PFOA and PFOS concentrations in solution after the completion of dark experiments. The initial rate of reaction as a function of C_0 and C_e is given by Eq. (42) and Eq. (43), respectively:

$$\tau_0 = \frac{k_\tau .KC_0}{1+KC_0} \quad (42)$$

$$\tau_0 = \frac{k_\tau . KC_e}{1+KC_e} \quad (43)$$

The parameters k_τ and K which are a function of C_0 or C_e can be predicted by linearizing the Eq. (43) or Eq. (44) as follows:

$$\frac{1}{\tau_0} = \frac{1}{k_\tau} + \frac{1}{k_\tau .KC_0} \quad (44)$$

Plot of τ_0 versus C_e for the photocatalytic degradation of 1000 mg/l PFOA and PFOS in the presence of 0.75 mg/l In_2O_3/Ga_2O_3 nanocomposite for different K values (0.087, 0.089, 0.090 and 0.099 min^{-1}) were shown in Figure 21.

* Figure 21 can be found in the Appendix section.

3.12.4 Effect of Temperature

Table 10. indicates that the maximum PFOA and PFOS photodegradation yields was detected at temperatures between 30oC and 40oC. Furher increase of temperature did not affect the PFOA and PFOS photodegradation. A number of researchers have also discussed the dependency of the photocatalytic reaction on the reaction temperature to activate the surface of In2O3/Ga2O3 nanocomposite the only presence of heat energy is insufficient when operating the process under illumination of natural sunlight. However, the perception of such dependency could be extrapolated. Studies have shown that an increase in temperature of the photocatalytic reaction (more than 80ºC) promotes recombination of charge carriers and thus, inhibiting the adsorption of organic compounds onto the surface of In2O3/Ga2O3 nanocomposite, [134]. In most cases, photocatalytic systems are operated at room temperature and heating is not required. The recommended range of operating temperature favouring the photo-decomposition process is generally between 20ºC and 80ºC, [135]

* Table 10 can be found in the Appendix section.

At temperatures less than 0ºC, the desorption rate of the final product will be reduced and hence, inducing an increase in the apparent activation energy. On the contrary, at temperatures more than 80ºC, the adsorption of reactant will be the limiting factor, causing the apparent activation energy to become negative. An increase in the photo-decomposition rate has been observed with the reaction temperature augmented within the temperature range of between 30ºC and 40ºC. A significant linear regression was detected between PFOA and PFOA photodegradation yields and increase of temperature from 20ºC up to 30ºC and 40ºC (F=0.099, p=0.98, R^2=0.99 and F=0.098, p=0.97, R^2=0.99, respectively). Further

increasing of the temperature did not improve the PFOA and PFOA yields (F=9.67, p=0,64, R^2=0.57 and F=9.63, p=0,67, R^2= 0.52).

3.12.5 Effect of Sun Light Power

The effect of light power on the removal efficiency of PFOA and PFOS was investigated. The positioning of the sunlight in top the photoreactor was performed. The optimal location for the light source was determined to be on the left side of the rotating cylinder, at a distance of approximately 1 cm from the substrate. As the cylinder rotates clockwise, it carries a thin layer of the PFOA and PFOS solution along its surface, and positioning the light source in the left side ensures maximum exposure to sun light irradiation. This configuration provides the highest intensity of radiation to the thin film of the pollutant solution, thereby enhancing the photocatalytic degradation process. The close proximity of the light source to the substrate also ensures more effective photon absorption by the photocatalyst, further contributing to improved dye removal efficiency.

Light is an imperative source that initiates heterogeneous photocatalytic processes and other photochemical processes. In a photochemical process, the formation of electron-hole pairs as well as the initiation rate of photocatalysis depends considerably on the intensity of light, [132]. The light distribution in a reactor basically decides the pollutant conversion efficiency as well as the pollutant degradation rate. Hence, extensive studies have been conducted in investigating the effect of light intensity on the pollutant degradation rate. In most studies, the pollutant degradation rate depends linearly on the light intensity, while in some cases, it demonstrates a square root dependency on the light intensity, [130]. Notably, at high intensity, the reaction rate is independent of the light intensity. This is likely to happen because at low intensity, the reactions involving electron-hole formation are much more significant than that involving electron-hole recombination. With increasing light intensity, the rate of electron-hole formation at the surface of In_2O_3/Ga_2O_3 nanocomposite rises and consequently, enhancing its ability to oxidize organic pollutants. It was found to be directly proportional to the photon flux when the flux is below 2000 photon 1/s.cm^2 corresponding to sun light power of 80 W/m^2 (Table 11).

* Table 11 can be found in the Appendix section.

Increasing of sun light power to 80 W/m^2 improved the PFOA and PFOS photodegradation rates (F=0.099, p=0.98, R^2=0.99 and F=0.098, p=0.97, R^2=0.99, respectively). Further increase of sun light power did not improve the photodegradation yields of both pollutants (F=8.99, p=0.68, R^2=0.67 and F=7.88, p=0.67, R^2=0.59, respectively). At low flux, the oxidizable organic substrate concentration is higher than the formation rate of electron-hole pairs within the photocatalyst, and thus, exhibiting a linear relationship between the degradation rate and the photo flux. On the contrary, at elevated photon flux (above 2000 photon 1/s.cm^2), the rate constant varies with the square root of the flux, in which the degradation rate experiences an immense reduction due to the significant effect of electron-hole recombination, [132], [134], [135].

To obtain a high photocatalytic reaction rate in wastewater treatment applications, a relatively abundant light intensity is required to sufficiently provide the titanium dioxide surface active sites with adequate photons energy.

3.12.6 Effect of Rotating Speed

The rotational speed of the disk plays a critical role in mass transfer and affects the thickness of the aqueous Effect of rotating speed the rotational speed of the disk plays a critical role in mass transfer and affects the thickness of the aqueous film formed on the cylinder surface. Table 12 illustrates the impact of rotation speed on the removal efficiencies of PFOA and PFOS 5 min of treatment. An increase in the cylinder's rotation speed correlates with an improvement in pollutant degradation, up to an optimal speed of 6 rpm. This enhancement is attributed to the improved mass transfer of both the pollutant and oxygen across the cylinder's surface at higher speeds, [134], [135]. However, beyond 6 rpm, the removal efficiency decreases, likely due to the reduced contact time between the pollutant and the photocatalyst surface, as the increased speed causes the pollutant solution to pass more rapidly over the substrate. Additionally, higher rotation speeds lead to increased energy consumption by the motor, with the maximum power usage observed at speeds of 7 rpm or higher. Based on the balance between pollutant removal efficiency and energy consumption, 5 rpm was identified as the optimal rotation speed for the photoreactor in subsequent experiments.

* Table 12 can be found in the Appendix section.

3.12.7 Effect of Contact Time

The effect of contact time on the photocatalytic degradation of PFOA and PFOS were carried out at different contact times (1, 2, 5, 10, 20, and 25 min) at constant PFOA and PFOS concentrations of 1000 mg/l a fixed dose of catalyst (0.75 mg/l), and an optimum pH value of 7.0 (Table 13). The maximum photo-

degradation efficiency was recorded after 5 min of direct sunlight irradiation as 99% and 98% for PFOA and PFOS, respectively. Increasing of contact time from 1 min, 2 and 5 min improved the PFOA and PFOS photodegradation rates (F=0.098, p= 0.98, R^2=0.99 and F=0.098, p=0.97, R^2=0.99, respectively). Further increase of time did not improve the photodegradation yields of both pollutants (F=8.95, p= 0.66, R^2=0.63 and F=7.80, p= 0.63, R^2=0.59, respectively).

* Table 13 can be found in the Appendix section.

In order to simulate the real environmental conditions, the PFOA and PFOS concentrations measured in a river were chosen as the lowest concentrations and the treatability studies were performed according to these values and the operational conditions were rearranged. The maximum concentrations of PFOA and PFOS were measures around 20µg/l. The photodegradation time, the In_2O_3/Ga_2O_3 nanocomposite loading and the pH was chosen as 3 min, 2 µg/l and 7.0, respectively. Sun light power and temperature was kept constant as 5 W/m^2 and 18^{o}C, respectively. 99% photoremoval efficiencies were detected for PFOA and PFOS for 20 cycles (Table 14).

* Table 14 can be found in the Appendix section.

3.13 Aqueous Fluoride Ions Formation

The measurement of aqueous fluoride ions and fluorine mass balance is essential to evaluate the extent of PFOS and PFOA defluorination and mineralization. Total fluorine was assessed by summing the contributions from both free inorganic fluoride and organically bound fluorine. While free fluoride was released it was directly measured and the fluorine content in parent PFOS and PFOA were estimated based on measured PFOS and PFOA concentrations. As shown in Table 15, over the treatment duration, the concentration of floride ions (F^-) in the aqueous increased.

* Table 15 can be found in the Appendix section.

3.14 Recovery and Reusability of In_2O_3/Ga_2O_3 Heterogenous Nanocomposite

To assess the reusability of the In_2O_3/Ga_2O_3 nanocomposite, photocatalytic degradation experiments were conducted over 100 cycles with the recovered nanocomposite. Table 16 presents the photodegradation percentages of PFOA and PFOS after each cycle. From the 1st to the 60th cycle, the photodegradation efficiencies for both PFOA and PFOS were consistently recorded at 99%. After the 80th cycle, the efficiency slightly decreased to 98%, and after 100 cycles, it was recorded at 97% (Table 16). These results demonstrate that the reusability of the heterogenous In_2O_3/Ga_2O_3 nanocomposite is maintained with minimal decrease in photocatalytic activity over 100 cycles. The ability of the nanocomposite to be reused multiple times without significant loss of performance is crucial for practical applications, as it reduces the cost of photodegradation processes and minimizes environmental impact.

* Table 16 can be found in the Appendix section.

In our study, we observed a high reusability yield of 97% after 100 cycles for the same nanocomposite.

3.15 The Effect of PFAS Chain Length on Photocatalytic Removal Yield

The photocatalytic degradation efficiency of PFAS is significantly influenced by their carbon chain length. PFAS can be classified into four categories based on their chain length - short-chain, medium-chain, long-chain, and ultra-long-chain. Short-chain PFAS, such as perfluorobutanoic acid (PFBA) and perfluoropentanoic acid (PFPeA), exhibit high removal efficiencies due to their higher solubility and mobility, which result in reduced adsorption onto photocatalysts and hinder the degradation process, [136], [137], [138]. Nevertheless, advanced oxidation processes (AOPs) have been shown to effectively degrade these compounds, although, the degradation rate is slower compared to longer-chain PFAS, [139].

In contrast, long-chain PFAS, such as PFOA and PFOS, demonstrate significantly higher degradation efficiencies. Studies have reported PFOA removal efficiencies of up to 93% using TiO_2-reduced graphene oxide (rGO) composites under UV–vis irradiation, [140], and more than 98.90% degradation with titanium-based metal-organic frameworks (MOFs), [141]. This enhanced degradation efficiency is attributed to the greater hydrophobicity of long-chain PFAS, which facilitates increased adsorption onto photocatalysts and promotes the generation of reactive species, such as $SO_4^{-2\bullet}$ and $OH^\bullet$ radicals, that contribute to the cleavage of chemical bonds, [136]. The degradation process frequently leads to the formation of shorter-chain PFAS intermediates, which can experience further mineralization, releasing fluoride ions as a byproduct, [140], [142].

Ultra-long-chain PFAS, while less extensively studied, are anticipated to follow similar degradation pat terns as long-chain PFAS due to their larger molecular size and hydrophobicity. The efficiency of photocatalytic degradation is further influenced by

several factors, including the selection of photocatalysts, the presence of co-existing substances such as dissolved organic matter, and environmental parameters such as pH and temperature. For instance, short-chain PFAS, like 6/2 FTS, can achieve nearly complete removal, while medium-chain compounds, such as perfluorononanoic acid (PFNA), also demonstrate high removal efficiencies. Long-chain PFAS, such as PFOA, exhibit up to 95% removal, whereas substances like PFOS and GenX show lower degradation rates, with GenX achieving only 37% removal, [136]. The functional group of PFAS plays a critical role in degradation rates, as perfluorocarboxylic acids (PFCAs) are more reactive compared to perfluorosulfonic acids (PFSAs). Additionally, defluorination rates tend to lag behind overall removal, which suggests greater resistance to complete mineralization, particularly in longer-chain PFAS. These findings underscore the significance of considering chain length, functional groups, and molecular structure in optimizing photocatalytic processes for the treatment of PFAS-contaminated water.

As a result, an approach that is specifically designed to address the distinct characteristics of each PFAS category is essential for the effective photocatalytic treatment of these contaminants, particularly for short-chain and ultra-long-chain PFAS. Further research is required to enhance the degradation efficiency of short-chain PFAS and to gain deeper insights into the mechanisms governing the degradation of ultra- long-chain compounds.

3.16 Fundamentals of PFAS Degradation by AOPs

In comparison with conventional homogeneous AOPs, heterogeneous AOPs for PFAS degradation are improved systems with incorporated catalysts. Heterogeneous AOPs use catalysts to activate oxidating agents (e.g., H_2O_2, O_3, persulfate), which contribute to the generation of powerful ROS such as $OH^{\bullet}$ and $SO_4^{-2\bullet}$ radicals, [143], [144]. Defluorination and the elimination of head groups (e.g., carboxylate and sulfonate groups) are linked, depending on the dominant ROS, contributing to the loss of head groups or breaking C - F bonds in perfluoroalkyl chains, [145]. Identifying effective ROS and their transformation pathways during oxidation reactions may provide insights into PFAS degradation mechanisms, which are fundamental for the design of heterogeneous AOPs [146].

3.16.1 General Pathways and ROS for PFAS Degradation

The degradation by AOPs of PFASs occurring in water environments starts with their hydrolysis products (Eq. 45). Below, perfluorocarboxylic acid (PFCA, $C_nF_{2n+1}COOH$) represents the PFAS, while the effective ROS is represented by $OH^{\bullet}$ radicals. The degradation mechanisms of PFASs by AOPs are closely linked to ROS and their effective sites of action. However, these pathways can be summarized as a general reaction course, [147]. Specifically, the oxidation of $C_nF_{2n+1}COO^-$ to $C_nF_{2n+1}COO^{\bullet}$ (Eq. 46) is initiated by radicals (e.g., $OH^{\bullet}$) generated from activated oxidizing agents, [148]. Light and electrical energy can also trigger this reaction, utilizing, for example, photogenerated holes (h^+) under ultraviolet radiation or the electron transfer process at the anode, [149]. Subsequently, spontaneous decarboxylation of $C_nF_{2n+1}COO^{\bullet}$ occurs due to its instability (Eq. 47), and the resulting perfluoralkyl radicals $C_nF_{2n+1}^{\bullet}$ transform into $C_nF_{2n+1}OH$ via hydroxylation (Eq. 48), [150]. After the spontaneous elimination of HF from $C_nF_{2n+1}OH$ (Eq. 49), the resulting acyl halide, $C_{n-1}F_{2n-1}COF$, undergoes a hydrolysis process (Eq. 50), generating a short-chain PFCA ($C_{n-1}F_{2n-1}COO^-$). Afterwards, this decarboxylation hydroxylation-elimination-hydroxylation (DHEH) procedure is performed repeatedly, with the remove of a CF_2 unit and the release of CO_2 and HF in each cycle (Eq. 46–50) until complete mineralization is achieved, [151], [152]. The general degradation pathways of perfluorosulfonic acid (PFSA) are similar, but with the initial oxidation of $C_nF_{2n+1}SO_3^-$ to $C_nF_{2n+1}^{\bullet}$ by ROS attacking the C−S bond, [153]. The resulting product then enters the defluorination cycle, similarly to PFCA.

$$C_nF_{2n+1}COOH \rightarrow C_nF_{2n+1}COO^- + H^+ \quad (45)$$

$$C_nF_{2n+1}COO^- + OH^{\bullet}(/ + h^+/ - e^-) \rightarrow C_nF_{2n+1}COO^{\bullet} + OH^- \quad (46)$$

$$C_nF_{2n+1}COO^{\bullet} \rightarrow C_nF_{2n+1}^{\bullet} + CO_2 \quad (47)$$

$$C_nF_{2n+1}^{\bullet} + OH^{\bullet} \rightarrow C_nF_{2n+1}OH \quad (48)$$

$$C_nF_{2n+1}OH + C_{n-1}F_{2n-1}COF + HF \quad (49)$$

$$C_{n-1}F_{2n-1}COF + H_2O \rightarrow C_{n-1}F_{2n-1}COO^- + HF + H^+ \quad (50)$$

Effective ROS in AOPs of PFASs vary based on the oxidizing agents and their activation methods. Free radicals, such as $OH^{\bullet}$, $SO_4^{-\bullet}$ and $O_2^{-\bullet}$ radicals, as well

as nonradicals like singlet oxygen ($^1O_2$) and holes (h^+), have been identified as dominant ROS that contribute individually or synergistically to the defluorination and destruction of PFASs through advanced oxidation, [154]. Fenton and Fenton-like processes, using hydrogen peroxide (H_2O_2) as the oxidant, generate $OH^•$ as the effective ROS when activated by Fe^{+2} or other transition metal-based chemicals or materials. Activated persulfate systems, utilizing persulfate (PDS, $S_2O_8^{-2}$) or peroxymonosulfate (PMS, HSO_5^-), primarily generate $SO_4^{-•}$ as the dominant ROS and exhibit reactivity due to the high redox potential (+ 2.5 V~3.1 V) and long lifetime (3.4×10^{-5} s) of $SO_4^{-•}$, [155], [156]. Meanwhile, it should be noted that the activation methods of PMS make a big difference to the types of ROS, e.g., $SO_4^{-•}$ via activation with carbon materials, $SO_4^{-•}$ and •OH via thermal and radiation activation, $SO_4^{-•}$ and peroxymonosulfate anion radicals ($SO_5^{-•}$) via transition metal activation, and $O_2^{-•}$ and $^1O_2$ via alkali activation, [157]. In addition, photogenerated h^+ acts as a powerful ROS that directly oxidizes PFASs or converts H_2O/O_2 to $OH^•/O_2^{-•}$, thereby generating more ROS, [158]. Electrochemical processes induce the rapid generation of different ROS at the anode or facilitate electron transfer to the anode, [158]. Hence, the application of light or electrical energy in AOPs has the potential to promote PFAS degradation by providing more powerful ROS or accelerating the oxidation processes. Photocatalytic or electrocatalytic AOPs are promising systems for highly effective PFAS remediation, deserving in-depth analysis and further research.

3.17 Comparative Assessment of the Efficiency of the Innovation Methods

Recent developments in the photocatalytic degradation of PFAS have led to the development of innovative materials and strategies, each offering distinct mechanisms and performance characteristics. Traditional semiconductor-based photocatalysts, such as TiO_2, Ga_2O_3, and In_2O_3, have been widely studied for their strong oxidative potential, [54]. However, their efficiency is often limited by their wide bandgaps, which restrict activation to UV light, reducing practicality under natural sunlight. In contrast, bismuth-based photocatalysts, particularly BiOCl and its composites, offer enhanced visible-light responsiveness due to their layered structures and internal electric fields, resulting in higher degradation efficiencies under solar irradiation compared to conventional metal oxides. Hybrid materials such as Fe/TNTs@AC exemplify the "concentrate-and-destroy" strategy by combining high adsorption capacity with photocatalytic degradation, achieving over 90% PFOA removal under UV light, outperforming many traditional catalysts by effectively concentrating pollutants at the reactive sites, [79]. Carbon-based materials such as biochar and graphene derivatives are also gaining attention for their dual roles as adsorbents and electron-conducting supports, [159].

Although their standalone photocatalytic activity is lower than that of engineered semiconductors, their integration into hybrid systems enhances charge transfer and reduces energy input, making them attractive for scalable, energy-efficient designs. Furthermore, AOPs, including photo- and electrocatalytic systems, have demonstrated high PFAS degradation rates by generating ROS (e.g., $OH^•$, $SO_4^{-2•}$) and facilitating electron transfer. These processes offer a cost- effective and robust pathway for breaking strong C - F bonds, although their efficiency depends heavily on catalyst composition, oxidant selection, and reactor design. MOFs like MIL-125-NH_2 have shown over 98.90% PFOA degradation, utilizing both reduction and oxidation processes. The coordinated action of hydrated electrons and $OH^•$ radicals is crucial for effective PFAS breakdown, [141]. Overall, while traditional photocatalysts like TiO_2 offer simplicity and stability, recent innovations such as oxygen defect engineered heterojunctions, adsorptive photocatalyst hybrids, and ROS driven AOPs consistently outperform them in terms of degradation efficiency and operational flexibility.

Comparative assessments suggest that the most effective strategies integrate multiple functionalities, including adsorption, light absorption, charge separation, and radical generation, into a single system. These approaches pave the way for scalable and high performance PFAS remediation technologies.

4 Conclusions

In this study, heterogenous In_2O_3/Ga_2O_3 nanocomposite was generated to remove PFOA and PFOS via photodegradation. The effects of some operational parameters on the photocatalytic activity of In_2O_3/Ga_2O_3 nanocomposite was investigated. Under optimized experimental conditions, the use of In_2O_3/Ga_2O_3 nanocomposite has often led to higher degradation rate for PFOA and PFOS under sun ligth. For maximum 99% PFOA and 98% PFOS photodegradation yields the optimized conditions were as follows: 0.75 mg/l In_2O_3/Ga_2O_3 nanocomposite concentration, 5 min time, 1000 mg/l PFOA and PFOS concentrations, pH=7.0, a rotating speed of 5 rpm and a temperature of 40°C, respectively. The PFOA and PFOS photodegradation

kinetic was according to Langmuir–Hinshelwood equation with k values of 0.087 and 0.099 min^{-1}.

Reusability studies showed that from the 1st to the 60th cycle, the photodegradation efficiencies for both PFOA and PFOS were consistently recorded as 99%. After the 80th cycle, the efficiency slightly decreased to 98%, and after 100 cycles, it was recorded at 97%.

The measurement of aqueous fluoride ions and fluorine mass balance is essential to evaluate the extent of PFOS and PFOA defluorination and mineralization. As the fluoride concentrations in the aqueous samples increased the PFOA and PFOS levels decreased.

In_2O_3-decorated Ga_2O_3 heterostructures, possess excellent field-emission characteristics. The improved electrical properties (increased conductivity and mobility) are important for the observed field emission behavior. We conconclude that a high aspect ratio, good crystallinity, special geometry, and enhanced conductivity are responsible for these field-emission characteristics.

Despite their high mass fractions, the oxides were found to be highly dispersed and amorphous by STEM EDX-mappings and XRD. Additionally, the processes led to specific surface areas of 260–340 m^2/g for GaO_x and 140–280 m^2/g for InO_x determined by N_2 physisorption analysis. The layer thicknesses were estimated based on thermogravimetric data which revealed a grows per cycle on average (gpc) of 0.7 Å for GaO_x and 1.5 Å for InO_x.

In conclusion, this study provides new insights into GaO_x and InO_x on mesoporous supports with high surface area. Both processes can potentially be applied for catalyst synthesis. Supported In_2O_3/Ga_2O_3 heterogenous nanocomposite photocatalysts might be further investigated for the treatment of other industrial wastewater containing refractory/ toxic organics.

Acknowledgement:
Experimental analyzes in this study were performed at the Laboratories of the Canada Research Center, Ottawa, Canada. The authors would like to thank this body for providing financial support.

References:

[1] P. Aditi, A.H.M.A. Sadmani, R. Debra, C. Ni-Bin, G. Ramesh, Per and Polyfluoroalkyl Substances (PFAS) as a Contaminant of Emerging Concern in Surface Water: A Transboundary Review of Their Occurrences and Toxicity Effects, Journal of Hazardous Materials, Vol.419, 2021, 126361.

[2] J.B. Brown, J.M. Conder, J.A. Arblaster, C.P. Higgins, Assessing Human Health Risks from Per- and Polyfluoroalkyl Substance (PFAS)-Impacted Vegetable Consumption: A Tiered Modelling Approach, Environmental Science & Technology, Vol.54, 2020, pp. 15202–15214.

[3] M. Sadia, I. Nollen, R. Helmus, T.L. Ter Laak, F. Been, A. Praetorius, A.P. van Wezel, Occurrence, Fate, and Related Health Risks of PFAS in Raw and Produced Drinking Water, Environmental Science & Technology, Vol.57, No.8, 2023, pp. 3062–3074.

[4] R.B. Jain, Association Between Thyroid Profile and Perfluoroalkyl Acids: Data from NHNAES 2007–2008, Environmental Research, Vol.126, 2013, pp. 51–59.

[5] M.B. Rosen, K.P. Das, J. Rooney, B. Abbott, C. Lau, J.C. Corton, PPARα-Independent Transcriptional Targets of Perfluoroalkyl Acids Revealed by Transcript Profiling, Toxicology, Vol.387, 2017, pp. 95–107.

[6] J. Liu, S. Mejia Avendano, Microbial Degradation of Polyfluoroalkyl Chemicals in the Environment: A Review, Environment International, Vol.61, 2013, pp. 98–114.

[7] Y. Li, Y. Zhang, X. Liu, X. Zhou, T. Ye, Q. Fu, M. Du, Q. Lu, Y. Zheng, D. Wang, Per- and Polyfluoroalkyl Substances Exacerbate the Prevalence of Plasmid-Borne Antibiotic Resistance Genes by Enhancing Natural Transformation, In Vivo Stability, and Expression in Bacteria, Water Research, Vol.272, 2025, 122972.

[8] N. Yashir, Q. Sun, X. Zhang, M. Ma, D. Wang, Y. Feng, X. Song, Co-Occurrence of Microplastics, PFASs, Antibiotics, and Antibiotic Resistance Genes in Groundwater and Their Composite Impacts on Indigenous Microbial Communities: A Field Study, Science of the Total Environment, Vol.961, 2025, 178373.

[9] I.J. Neuwald, D. Hübner, H.L. Wiegand, V. Valkov, U. Borchers, K. Nödler, M. Scheurer, S.E. Hale, H.P.H. Arp, D. Zahn, Ultra-Short-Chain PFASs in the Sources of German Drinking Water: Prevalent, Overlooked, Difficult to Remove, and Unregulated, Environmental Science & Technology, Vol.56, No.10, 2022, pp. 6380–6390.

[10] E. Gorrochategui, E. Perez-Albaladejo, J. Casas, S. Lacorte, C. Porte, Perfluorinated Chemicals: Differential Toxicity, Inhibition of Aromatase Activity and Alteration of Cellular Lipids in Human

Placental Cells, Toxicology and Applied Pharmacology, Vol.277, No.2, 2014, pp. 124-130.

[11] B.J. Yates, R. Darlington, R. Zboril, V.K. Sharma, High-Valent Iron-Based Oxidants to Treat Perfluorooctanesulfonate and Perfluorooctanoic Acid in Water, Environmental Chemistry Letters, Vol.12, No.3, 2014, pp. 413-417.

[12] Y. Wang, P. Zhang, G. Pan, H. Chen, Ferric Ion Mediated Photochemical Decomposition of Perfluorooctanoic Acid (PFOA) by 254 nm UV light, Journal of Hazardous Materials, Vol.160, No.1, 2008, pp. 181-186.

[13] C. Gallen, C. Baduel, F.Y. Lai, K. Thompson, J. Thompson, M. Warne, J.F. Mueller, Spatio-Temporal Assessment of Perfluorinated Compounds in the Brisbane River System, Australia: Impact of A Major Flood Event, Marine Pollution Bulletin, Vol.85, No.2, 2014, pp. 597-605.

[14] J.M. Armitage, M. MacLeod, I.T. Cousins, Comparative Assessment of the Global Fate and Transport Pathways of Long-Chain Perfluorocarboxylic Acids (PFCAs) and Perfluorocarboxylates (PFCs) Emitted from Direct Sources, Environmental Science & Technology, Vol.43, No.15, 2009, pp. 5830-5836.

[15] G.B. Post, P.D. Cohn, K.R. Cooper, Perfluorooctanoic Acid (PFOA), An Emerging Drinking Water Contaminant: A Critical Review of Recent Literature, Environmental Research, Vol.116, 2012, pp. 93–117.

[16] A. Pistocchi, R. Loos, R., A Map of European Emissions and Concentrations of PFOS and PFOA, Environmental Science & Technology, Vol. 43, No.24, 2009, pp. 9237-9244.

[17] C. Flores, F. Ventura, J. Martin-Alonso, J. Caixach, Occurrence of Perfluorooctane Sulfonate (PFOS) and Perfluorooctanoate (PFOA) in NE Spanish Surface Waters and Their Removal in A Drinking Water Treatment Plant that Combines Conventional and Advanced Treatments in Parallel Lines, Science of the Total Environment, Vol.461, 2013, pp. 618-626.

[18] W. Zhang, Y. Zhang, S. Taniyasu, L.W. Yeung, P.K. Lam, J. Wang, X. Li, N. Yamashita, J. Dai, Distribution and Fate of Perfluoroalkyl Substances in Municipal Wastewater Treatment Plants in Economically Developed Areas of China, Environmental Pollution, Vol.176, 2013, pp. 10-17.

[19] H. Chen, X. Wang, C. Zhang, R. Sun, J. Han, G. Han, W. Yang, X. He, Occurrence and Inputs of Perfluoroalkyl Substances (PFAS) from Rivers and Drain Outlets to the Bohai Sea, China, Environmental Pollution, Vol.221, 2017, pp. 234-243.

[20] M. Murakami, C. Morita, T. Morimoto, H. Takada, Source Analysis of Perfluorocarboxylates in Tokyo Bay during Dry Weather and Wet Weather Using Sewage Markers, Environmental Chemistry, Vol.8, No.4, 2013, pp. 2017, 355.

[21] J.E. Naile, J.S. Khim, T. Wang, C. Chen, W. Luo, B.O. Kwon, J. Park, C.H. Koh, P.D. Jones, Y. Lu, J.P. Giesy, Perfluorinated Compounds in Water, Sediment, Soil and Biota from Estuarine and Coastal Areas of Korea, Environmental Pollution, Vol.158, No.5, 2010, pp. 1237-1244.

[22] A. Podder, A. Sadmani, D. Reinhart, N. Chang, R. Goel, Per- and Poly-Fluoroalkyl Substances (PFAS) as a Contaminant of Emerging Concern in Surface Water: A Transboundary Review of Their Occurrences and Toxicity Effects, Journal of Hazardous Materials, Vol.419, 2021, 126361.

[23] J. Domingo, M. Nadal, Human Exposure to Per- and Polyfluoroalkyl Substances (PFAS) through Drinking Water: A Review of the Recent Scientific Literature, Environmental Research, Vol.177, 2019, 108648.

[24] USEPA, National Primary Drinking Water Regulations, 2024, pp. 1-9, https://www.mallard-inc.com/wp-content/uploads/2019/05/Drinking-Water-Standards.pdf, (accessed on 05 November 2025).

[25] USEPA, Interim Updated PFOA and PFOS Health Advisories. 2022. Available online: https://www.epa.gov/sdwa/drinking-water-health-advisories-pfoa-and-pfos, (accessed on 07 November 2025).

[26] Eurofins, PFAS in the Revised Drinking Water Directive (DWD), 2023. Available online: https://www.eurofins.se/tjaenster/miljoeoch-vatten/nyheter-miljo/pfas-in-the-revised-drinking-water-directive-dwd/, (accessed on 09 November 2025).

[27] S.C.E. Leung, P. Shukla, D. Chen, E. Eftekhari, H. An, F. Zare, N. Ghasemi, D. Zhang, N.-T. Nguyen, Q. Li, Emerging Technologies for PFOS/PFOA Degradation and Removal: A Review, Science of the Total Environment, Vol.827, 2022, 153669.

[28] M. Ateia, A. Maroli, N. Tharayil, T. Karanfil, The Overlooked Short- and Ultrashort-Chain Poly- and Perfluorinated Substances: A Review, Chemosphere, Vol.220, 2019, pp. 866–882.

[29] T. Mastropietro, R. Bruno, E. Pardo, D. Armentano, Reverse Osmosis and Nanofiltration Membranes for Highly Efficient PFAS Removal: Overview, Challenges and Future Perspectives, Dalton Transactions, Vol.50, 2021, pp. 5398–5410.

[30] O.C. Olatunde, A.T. Kuvarega, D.C. Onwudiwe, Photo-Enhanced Degradation of Polyfluoroalkyl and Perfluoroalkyl Substances, Heliyon, Vol.6, 2020, e05614.

[31] Y.-L. Zhang, W.-L. Wang, M.-Y. Lee, Z.-W. Yang, Q.-Y. Wu, N. Huang, H.-Y. Hu, Promotive Effects of Vacuum-UV/UV (185/254 nm) Light on Elimination of Recalcitrant Trace Organic Contaminants by UV-AOPs during Wastewater Treatment and Reclamation: A Review, Science of the Total Environment, Vol.818, 2022, 151776.

[32] S. Verma, B. Mezgebe, C.A. Hejase, E. Sahle-Demessie, M.N. Nadagouda, Photodegradation and Photocatalysis of Per- and Polyfluoroalkyl Substances (PFAS): A Review of Recent Progress, Next Materials, Vol.2, 2024, pp. 1–12.

[33] H. Wang, L. Zhang, Z. Chen, J. Hu, S. Li, Z. Wang, J. Liu, X. Wang, Semiconductor Heterojunction Photocatalysts: Design, Construction, and Photocatalytic Performances, Chemical Society Reviews, Vol.43, 2014, pp. 5234–5244.

[34] J. Luo, W. Li, R. Yin, Q. Liu, X. Xin, L. Yang, K. He, D. Ma, S. Lv, D. Xing, Photocatalyst Degradation of Perfluorooctanoic Acid in Water: Mechanisms, Approaches, and Perspectives, Separation and Purification Technology, Vol.338, 2024, 126503.

[35] V. Kitsiou, N. Filippidis, D. Mantzavinos, I. Poulios, Heterogeneous and Homogeneous Photocatalytic Degradation of the Insecticide Imidacloprid in Aqueous Solutions, Applied Catalysis B: Environment and Energy, Vol.86, 2009, pp. 27-35.

[36] R. Giri, H. Ozaki, T. Morigaki, S. Taniguchi, R. Takanami, UV Photolysis of Perfluorooctanoic Acid (PFOA) in Dilute Aqueous Solution, Water Science and Technology, Vol.63, No.2, 2011, pp. 276-282.

[37] N. Merino, Y. Qu, R.A. Deeb, E.L. Hawley, M.R. Hoffmann, S. Mahendra, Degradation and Removal Methods for Perfluoroalkyl and Polyfluoroalkyl Substances in Water, Environmental Engineering Science, Vol.33, No.9, 2016, pp. 615-649.

[38] B. Zhao, X. Li, L. Yang, F. Wang, J. Li, W. Xia, W. Li, L. Zhou, C. Zhao, b-Ga2O3 Nanorod Synthesis with A One-step Microwave Irradiation Hydrothermal Method and Its Efficient Photocatalytic Degradation for Perfluorooctanoic Acid, Photochemistry and Photobiology, Vol.91, 2015, pp. 42-47.

[39] X. Li, P. Zhang, L. Jin, T. Shao, Z. Li, J. Cao, Efficient Photocatalytic Decomposition of Perfluorooctanoic Acid by Indium Oxide and Its Mechanism, Environmental Science & Technology, Vol.46, 2012, pp. 5528–5534.

[40] Z. Li, P. Zhang, T. Shao, X. Li, In2O3 Nanoporous Nanosphere: A Highly Efficient Photocatalyst for Decomposition of Perfluorooctanoic Acid, Applied Catalysis B: Environment and Energy, Vol.125, 2012, pp. 350-357.

[41] Z. Li, P. Zhang, J. Li, T. Shao, J. Wang, L. Jin, Synthesis of In2O3 Porous Nanoplates for Photocatalytic Decomposition of Perfluorooctanoic Acid (PFOA), Catalysis Communications, Vol.43, 2014, pp. 42-46.

[42] C. Xu, P. Qiu, H. Chen, F. Jiang, X. Wang, Fabrication of Two-Dimensional Indium Oxide Nanosheets with Graphitic Carbon Nitride Nanosheets as Sacrificial Templates, Materials Letters, Vol.242, 2019, pp. 24–27.

[43] F. Jiang, H. Zhao, H. Chen, C. Xu, J. Chen, Enhancement of Photocatalytic Decomposition of Perfluorooctanoic Acid on CeO2/In2O3, RSC Advances, Vol.6, 2016, pp. 72015–72021.

[44] Y. Wu, Y. Li, C. Fang, C. Li, Highly Efficient Degradation of Perfluorooctanoic Acid over a MnOx-Modified Oxygen-Vacancy-Rich In2O3 Photocatalyst, ChemCatChem, Vol.11, No.9, 2019, pp. 2297–2303.

[45] M. Qin, J. Ma, W. Ke, P. Qin, H. Lei, H. Tao, X. Zheng, L. Xiong, Q. Liu, Z. Chen,

J. Lu, G. Yang, G. Fang, Perovskite Solar Cells Based on Low-Temperature Processed Indium Oxide Electron Selective Layers, ACS Applied Materials & Interfaces, Vol.8, 2016, pp. 8460–8466.

[46] B. Xu, J.L. Zhou, A. Altaee, M.B. Ahmed, M.A.H. Johir, J. Ren, X. Li, Improved Photocatalysis of Perfluorooctanoic Acid in Water and Wastewater by Ga2O3/UV System Assisted by Peroxymonosulfate, Chemosphere, Vol.239, 2020, 124722. [

[47] H. Ryou, T.H. Yoo, Y. Yoon, I.G. Lee, M. Shin, J. Cho, B.J. Cho, W.S. Hwang, Hydrothermal Synthesis and Photocatalytic Property of Sn-doped-Ga2O3 Nanostructure, ECS Journal of Solid State Science and Technology, Vol.9, 2020, 045009.

[48] X. Tan, G. Chen, D. Xing, W. Ding, H. Liu, T. Li, Y. Huang, Indium-Modified Ga2O3 Hierarchical Nanosheets as Efficient Photocatalysts for the Degradation of Perfluorooctanoic Acid, Environmental Science: Nano, Vol.7, 2020, pp. 2229–2239.

[49] A.V. Almaev, E.V. Chernikov, N.A. Davletkildeev, D.V. Sokolov, Oxygen Sensors Based on Gallium Oxide Thin Films with Addition of Chromium, Superlattices and Microstructures, Vol.139, 2020, 106392.

[50] A. Habib, M. S. Khan, M. Zubair, I. U. Hasan, Ni-Doped In2O3 Nanoparticles and Their Composite with rGO for Efficient Degradation of Organic Pollutants in Wastewater under Visible Light Irradiation, International Journal of Molecular Sciences, Vol.24, 2023, 7950.

[51] T. Shao, P. Zhang, L. Jin, Z. Li, Photocatalytic Decomposition of Perfluorooctanoic Acid in Pure Water and Sewage Water by Nanostructured Gallium Oxide, Applied Catalysis B: Environment and Energy, Vol.142, 2013a, pp. 654-661.

[52] J. Chen, S. Wang, S. Wang, R. Tang, H. Chen, Facilely Prepared Bi4O7 Commercial Ga2O3 Modified with Optimized Photocatalytic Efficiency for Perfluorooctanoic Acid Degradation, Applied Surface Science, Vol.673, 2024, 160877.

[53] C. Fu, X. Xu, C. Zheng, X. Liu, D. Zhao, W. Qiu, Photocatalysis of Aqueous PFOA by Common Catalysts of In2O3, Ga2O3, TiO2, CeO2 and CdS: Influence Factors and Mechanistic Insights, Environmental Geochemistry and Health, Vol.44, 2022, pp. 2943–2953.

[54] R. Fernandes, A. Silva, B. Cardoso, P.J.G. Coutinho, L. Pereira, Potential of Photocatalytic Nanomaterials for PFOA and PFOS Degradation: Challenges and Opportunities, Journal of Environmental Chemical Engineering, Vol.13, 2024, 115201.

[55] X.J. Lyu, W.W. Li, P.K.S. Lam, H.Q. Yu, Photodegradation of Perfluorooctane Sulfonate in Environmental Matrices, Separation and Purification Technology, Vol.151, 2015, pp. 172-176.

[56] T. Shao, P. Zhang, Z. Li, L. Jin, Photocatalytic Decomposition of Perfluorooctanoic Acid in Pure Water and Wastewater by Needle-Like Nanostructured Gallium Oxide, Chinese Journal of Catalysis, Vol.34, No.8, 2013, pp. 1551-1559.

[57] Z. Zsilak, E. Szabo-Bardos, O. Fonagy, O. Horvath, K. Horvath, P. Hajos, Degradation of Benzenesulfonate by Heterogeneous Photocatalysis Combined with Ozonation, Catalysis Today, Vol.230, 2014, pp. 55-60.

[58] M.J. Chen, S.L. Lo, Y.C. Lee, C.C. Huang, Photocatalytic Decomposition of Perfluorooctanoic Acid by Transition-Metal Modified Titanium Dioxide, Journal of Hazardous Materials, Vol.288, 2015, pp. 168-175.

[59] M.R. Hoffmann, S.T. Martin, W. Choi, D.W. Bahnemann, Environmental Applications of Semiconductor Photocatalysis, Chemical Reviews, Vol.95, 1995, pp. 69-96.

[60] S. Kutsuna, Y. Nagaoka, K. Takeuchi, H. Hori, TiO2-Induced Heterogeneous Photodegradation of a Fluorotelomer Alcohol in Air, Environmental Science & Technology, Vol.40, 2006, pp. 6824-6829.

[61] S. C. Panchangam, A. Y. Lin, K. L. Shaik, C. F. Lin, Decomposition of Perfluorocarboxylic Acids (PFCAs) by Heterogeneous Photocatalysis in Acidic Aqueous Medium, Chemosphere, Vol.77, No.2, 2009, pp. 242-248.

[62] Y. Qu, C. Zhang, F. Li, J. Chen, Q. Zhou, Photo-Reductive Defluorination of Perfluorooctanoic Acid in Water, Water Research, Vol.44, No.9, 2010, pp. 2939-2947.

[63] Y. Wang, P. Zhang, Photocatalytic Decomposition of Perfluorooctanoic Acid (PFOA) by TiO2 in the Presence of Oxalic Acid, Journal of Hazardous Materials, Vol.192, No.3, 2011, pp. 1869-1875.

[64] K. Okitsu, K. Iwasaki, Y. Yobiko, H. Bandow, R. Nishimura, Y. Maeda, Sonochemical Degradation of Azo Dyes in Aqueous Solution: A New Heterogeneous Kinetics Model taking into Account the Local Concentration of OH Radicals and Azo Dyes, Ultrasonics Sonochemistry, Vol.12, No.4, 2005, pp. 255-262.

[65] C. Vecitis, H. Park, J. Cheng, B. Mader, M. Hoffmann, Enhancement of Perfluorooctanoate and Perfluorooctanesulfonate Activity at Acoustic Cavitation Bubble Interfaces, Journal of Physical Chemistry C, Vol.112, No.43, 2008, pp. 16850-16857.

[66] Y. Zhang, J. Zhang, Y. Xiao, V.W. Chang, T. T. Lim, Direct and Indirect Photodegradation Pathways of Cytostatic Drugs under UV Germicidal Irradiation: Process Kinetics and Influences of Water Matrix Species and Oxidant Dosing, Journal of Hazardous Materials, Vol.324, 2017, pp. 481-488.

[67] J. Liang, L. Guo, B. Xiang, X. Wang, J. Tang, Y. Liu, Research Updates on the Mechanism and Influencing Factors of the Photocatalytic Degradation of Perfluorooctanoic Acid (PFOA) in Water Environments, Molecules, Vol.28, 2023, 4489.

[68] X. Liu, X. Duan, T. Bao, D. Hao, Z. Chen, W. Wei, D. Wang, S. Wang, B.-J. Ni, High-Performance Photocatalytic Decomposition of PFOA by BiOX/TiO2 Heterojunctions: Self-Induced Inner Electric Fields and Band Alignment, Journal of Hazardous Materials, Vol.430, 2022, 128195.

[69] Z. Liu, Z. Chen, J. Gao, Y. Yu, Y. Men, C. Gu, J. Liu, Accelerated Degradation of Perfluorosulfonates and Perfluorocarboxylates by UV/Sulfite + Iodide: Reaction Mechanisms and System Efficiencies, Environmental Science & Technology, Vol.56, No.6, 2022, pp. 3699–3709.

[70] P. Yin, Z. Hu, X. Song, J. Liu, N. Lin, Activated Persulfate Oxidation of Perfluorooctanoic Acid (PFOA) in Groundwater under Acidic Conditions, International Journal of Environmental Research and Public Health, Vol.13, No.6, 2016, 602.

[71] J. N. Uwayezu, I. Carabante, P. van Hees, P. Karlsson, J. Kumpiene, Validation of UV/Persulfate as a PFAS Treatment of Industrial Wastewater and Environmental Samples, Journal of Water Process Engineering, Vol.53, 2023, 103614.

[72] B. Esfahani, M. Mohseni, Fluence-Based Photo-Reductive Decomposition of PFAS Using Vacuum UV (VUV) Irradiation: Effects of Key Parameters and Decomposition Mechanism, Journal of Environmental Chemical Engineering, Vol.10, 2022, 107050.

[73] A. Mills, R. H. Davies, D. Worsley, Water Purification by Semiconductor Photocatalysis, Chemical Society Reviews, Vol.22, No.6, 1993, pp. 417–425.

[74] H. Wang, L. Zhang, Z. Chen, J. Hu, S. Li, Z. Wang, J. Liu, X. Wang, Semiconductor Heterojunction Photocatalysts: Design, Construction, and Photocatalytic Performances, Chemical Society Reviews, Vol.43, No.15, 2014, pp. 5234–5244.

[75] E. Bouteh, M. J. Bentel, E. L. Cates, Semiconductor-Hydrophobic Material Interfaces as a New Active Site Paradigm for Photocatalytic Degradation of Perfluorocarboxylic Acids, Journal of Hazardous Materials, Vol.453, 2023, 131437.

[76] R. Cheng, J. Xia, J. Wen, P. Xu, X. Zheng, Nano Metal-Containing Photocatalysts for the Removal of Volatile Organic Compounds: Doping, Performance, and Mechanisms, Nanomaterials, Vol.12, 2022, 1335.

[77] C. Xia, X. Lim, H. Yang, B. M. Goodson, J. Liu, Degradation of Per- and Polyfluoroalkyl Substances (PFAS) in Wastewater Effluents by Photocatalysis for Water Reuse, Journal of Water Process Engineering, Vol.46, 2022, 102556.

[78] J. Wen, H. Li, L. D. M. Ottosen, J. Lundqvist, L. Vergeynst, Comparison of the Photocatalytic Degradability of PFOA, PFOS, and GenX Using Fe-Zeolite in Water, Chemosphere, Vol.344, 2023, 140344.

[79] F. Li, Z. Wei, K. He, L. Blaney, X. Cheng, T. Xu, W. Liu, D. Zhao, A Concentrate-and-Destroy Technique for Degradation of Perfluorooctanoic Acid in Water Using a New Adsorptive Photocatalyst, Water Research, Vol.185, 2020, 116219.

[80] M. Qanbarzadeh, L. DiGiacomo, E. Bouteh, E. Z. Alhamdan, M. M. Mason, B. Wang, M. S. Wong, E. L. Cates, An Ultraviolet/Boron Nitride Photocatalytic Process Efficiently Degrades Poly /Perfluoroalkyl Substances in Complex Water Matrices, Environmental Science &

Technology Letters, Vol.10, No.8, 2023, pp. 705–710.

[81] L. Duan, B. Wang, K. Heck, S. Guo, C. A. Clark, J. Arredondo, M. Wang, T. P. Senftle, P. Westerhoff, X. Wen, Y. Song, M. S. Wong, Efficient Photocatalytic PFOA Degradation Over Boron Nitride, Environmental Science & Technology Letters, Vol.7, No.8, 2020, pp. 613–619.

[82] J. H. Zar, Biostatistical Analysis, Prentice-Hall, Englewood Cliffs, 1984.

[83] Statgraphics Centurion XV, Sofware, StatPoint Inc, Statgraphics Centurion XV, Herndon, VA, USA, 2005.

[84] I. Donmez, C. Ozgit-Akgun, N. Biyikli, Low Temperature Deposition of Ga2O3 Thin Films Using Trimethylgallium and Oxygen Plasma, Journal of Vacuum Science and Technology A: Vacuum, Surfaces and Films, Vol.31, 2013, 01A110.

[85] A. Sharma, M. Varshney, H. Saraswat, S. Chaudhary, J. Parkash, H.-J. Shin, K.-H. Chae, S.-O. Won, Nano-Structured Phases of Gallium Oxide (GaOOH, -Ga2O3, -Ga2O3, -Ga2O3, -Ga2O3, and -Ga2O3): Fabrication, Structural, and Electronic Structure Investigations, International Nano Letters, Vol.10, 2020, pp. 71–79.

[86] S. Tan, L.B. Gil, N. Subramanian, D.S. Sholl, S. Nair, C.W. Jones, J.S. Moore, Y. Liu, R.S. Dixit, J.G. Pendergast, Catalytic Propane Dehydrogenation over In2O3–Ga2O3 Mixed Oxides, Applied Catalysis A: General, Vol.498, 2015, pp. 167–175.

[87] A.K. Nayak, S. Lee, Y. Sohn, D. Pradhan, Biomolecule-Assisted Synthesis of In(OH)3 Nanocubes and In2O3 Nanoparticles: Photocatalytic Degradation of Organic Contaminants and CO Oxidation, Nanotechnology, Vol.26, 2015, 485601.

[88] A.U. Mane, A.J. Allen, R.K. Kanjolia, J.W. Elam, Indium Oxide Thin Films by Atomic Layer Deposition Using Trimethylindium and Ozone, Journal of Physical Chemistry C, Vol.120, 2016, pp. 9874–9883.

[89] M. Faur, M. Faur, D.T. Jayne, M. Goradia, C. Goradia, XPS Investigation of Anodic Oxides Grown on P-type InP, Surface and Interface Analysis, Vol.15, 1990, pp. 641–650.

[90] M.L. Miller, W.R. Linton, X-ray Photoelectron Spectroscopy of Thermally Treated Silica (SiO2) Surfaces, Analytical Chemistry, Vol.57, 1985, pp. 2314–2319.

[91] L. Sun, R. Li, W. Zhan, Y. Yuan, X. Wang, X. Han, Y. Zhao, Double-Shelled Hollow Rods Assembled from Nitrogen/Sulfur Codoped Carbon Coated Indium Oxide Nanoparticles as Excellent Photocatalysts, Nature Communications, Vol.10, 2019, 2270.

[92] A. Navarro-Quezada, S. Alamé, N. Esser, J. Furthmüller, F. Bechstedt, Z. Galazka, D. Skuridina, P. Vogt, Near Valence-band Electronic Properties of Semiconducting Ga2O3 (100) Single Crystals, Physical Review B: Condensed Matter and Materials Physics, Vol.92, 2015, 195306.

[93] C. Huang, W. Mu, H. Zhou, Y. Zhu, X. Xu, Z. Jia, L. Zheng, X. Tao, Effect of OH on Chemical Mechanical Polishing of-Ga2O3 (100) Substrate using an Alkaline Slurry, RSC Advances, Vol.8, 2018, pp. 6544–6550.

[94] A. Gou, Y. Cheng, F. Zhu, T. Yu, H. Yin, L. Che, J. Chen, X. Zhang, Study on Oxygen Vacancies in Gallium Oxide Nanostructures, Journal of Materials Science: Materials in Electronics, Vol.34, No.12 2023, Article number:1052.

[95] Z. Liu, T. Yamazaki, Y. Shen, T. Kikuta, N. Nakatani, Y. Li, O2 and CO sensing of Ga2O3 multiple nanowire gas sensors, Sensors and Actuators, B: Chemical, Vol.129, No.2, 2008, pp. 666–670.

[96] A. Afzal, β-Ga2O3 Nanowires and Thin Films for Metal Oxide Semiconductor Gas Sensors: Sensing Mechanisms and Performance Enhancement Strategies, Journal of Materiomics, Vol.5, No.4, 2019, pp. 542-557.

[97] M. H. Brodsky, Amorphous Semiconductors, Springer-Verlag, Berlin, Heidelberg, New York, 1979.

[98] J. W. Orton, M. J. Powel, The Hall Effect in Polycrystalline and Powdered Semiconductors, Reports on Progress in Physics, Vol.43, 1980, 1263.

[99] J. Y. W. Seto, The Electrical Properties of Polycrystalline Silicon Film, Journal of Applied Physics, Vol.46, No.12, 1975, pp. 5247-5254.

[100] M. N. Martyshov, P. A. Forsh, V. Yu. Timoshenko, P. K. Kashkarov, Electrical Conductivity in Anisotropic Porous Silicon Films, Journal of Nanoelectronics and Optoelectronics, Vol.4, 2009, pp. 134-136.

[101] N. F. Mott, E. A. Devis, Electronic Properties in Non-crystalline Materials, Clarendon, Press, Oxford, 1971.
[102] R. Mansfield, S. Abboudy, P. Pozooni, Hopping Conduction in n-Type Indium Phosphide, Philosophical Magazine B, Vol.57, No.6, 1988, pp. 777-789.
[103] M. M. Abdul-Gader, M. A. Al-Basha, K. A. Wishah, Temperature Dependence of DC Conductivity of As-Deposited and Annealed Selenium Films, International Journal of Electronics, Vol.85, 1998, pp. 21-41.
[104] N. F. Mott, Conduction in Glasses Containing Transition Metal Ions, Journal of Non-Crystalline Solids, Vol.1, No.1, 1968, pp. 1-17.
[105] O. Bierwagen, J. S. Speck, High Electron Mobility In2O3 (001) and (111) Thin Films with Nondegenerate Electron Concentration, Applied Physics Letters, Vol.97, No.7, 2010, 072103.
[106] N. Serin, A. Yildiz, A.A. Alsaç, T. Serin, Estimation of Compensation Ratio by Identifying the Presence of Different Hopping Conduction Mechanisms in SnO2 Thin Films, Thin Solid Films Vol.519, No.7, 2011, pp. 2302-2307.
[107] E. Barsoukov, J. R. Macdonald, Impedance Spectroscopy: Theory, Experiment, and Applications, John Wiley & Sons, New Jersey, 2005.
[108] M. Ben-Chorin, F. Moller, F. Koch, W. Schirmacher, M. Eberhard, Hopping Transport on A fractal: AC Conductivity of Porous Silicon, Physical Review B, Vol.51, 1995, 2199.
[109] R. A. Street, G. Davis, A. D. Yoffe, The Square Law Dependence with Frequency of the Electrical Conductivity of As2Se3, Journal of Non-Crystalline Solids, Vol.5, No.3, 1971, pp. 276-278.
[110] J. C. Dyre, P. Maass, B. Roling, D. L. Sidebottom, Fundamental Questions Relating to Ion Conduction in Disordered Solids, Reports on Progress in Physics, Vol.72, No.4, 2009, 046501.
[111] Y. Huang, Z. Wang, Q. Wang, C. Gu, C. Tang, Y. Bando, D. Golberg, Quasi-Aligned Ga2O3 Nanowires Grown on Brass Wire Meshes and Their Electrical and Field-Emission Properties, Journal of Physical Chemistry C, Vol.113, 2009, pp. 1980–1983.
[112] J. Lin, Y. Huang, Y. Bando, C. Tang, C. Li, D. Golberg, Synthesis of In2O3 Nanowire-Decorated Ga2O3 Nanobelt Heterostructures and Their Electrical and Field-Emission Properties, ACS Nano, Vol.4, No.4, 2010, pp. 2452–2458.
[113] Z. Zhang, K. Yao, Y. Liu, C. Jin, X. Liang, Q. Chen, L. M. Peng, Quantitative Analysis of Current-Voltage Characteristics of Semiconducting Nanowires: Decoupling of Contact Effects, Advanced Functional Materials, Vol.17, 2007, pp. 2478–2489.
[114] Z. Y. Zhang, C. H. Jin, X. L. Liang, Q. Chen, L. M. Peng, Current-Voltage Characteristics and Parameter Retrieval of Semiconducting Nanowires, Applied Physics Letters, Vol.88, 2006, 073102.
[115] H. He, R. Orlando, M. A. Blanco, R. Pandey, First-Principles Study of the Structural, Electronic, and Optical Properties of Ga2O3 in its Monoclinic and Hexagonal Phases, Physical Review B: Condensed Matter and Materials Physics, Vol.74, 2006, 195123.
[116] J. Zhan, Y. Bando, J. Hu, Y. Li, D. Golberg, Synthesis and Field-Emission Properties of Ga2O3-C Nanocables, Chemistry of Materials, Vol.16, 2004, pp. 5158–5161.
[117] C. Cao, Z. Chen, X. An, H. Zhu, Growth and Field Emission Properties of Cactus-Like Gallium Oxide Nanostructures, Journal of Physical Chemistry C, Vol.112, 2008, pp. 95–98.
[118] S. Kar, S. Chaudhuri, Synthesis, Photoluminescence and Field Emission Properties of In2O3 Nanowires, Chemical Physics Letters, Vol.422, 2006, pp. 424–428.
[119] S. Q. Li, Y. X. Liang, T. H. Wang, Nonlinear Characteristics from In2O3 Nanowires Grown on InAs Substrate. Applied Physics Letters, Vol.88, 2006, 053107.
[120] X. Fang, Y. Bando, U. K. Gautam, C. Ye, D. Golberg, Inorganic Semiconductor Nanostructures and Their Field-Emission Applications, Journal of Materials Chemistry, Vol.18, 2008, pp. 509–522.
[121] T. Zhai, X. Fang, Y. Bando, Q. Liao, X. Xu, H. Zeng, Y. Ma, J. Yao, D. Golberg, Morphology-Dependent Stimulated Emission and Field Emission of Ordered CdS Nanostructure Arrays, ACS Nano, Vol.3, 2009, pp. 949–959.
[122] D. Y. Zhong, G. Y. Zhang, S. Liu, T. Sakurai, E. G. Wang, Universal Field-Emission Model for Carbon Nanotubes on a

Metal Tip, Applied Physics Letters, Vol.80, 2002, pp. 506–508.

[123] C. Li, G. J. Fang, N. S. Liu, J. Li, L. Liao, F. H. Su, G. H. Li, X. G. Wu, X. Z. Zhao, Structural, Photoluminescence, and Field Emission Properties of Vertically Well-Aligned ZnO Nanorod Arrays, Journal of Physical Chemistry C, Vol.111, 2007, pp. 12566–12571.

[124] D. Kaur, M. Kumar, A Strategic Review on Gallium Oxide Based Deep-Ultraviolet Photodetectors: Recent Progress and Future Prospects, Advanced Optical Materials, Vol.9, No.9, 2021, 2002160.

[125] X.H. Chen, F.F. Ren, S.L. Gu, J.D. Ye, Review of Gallium-Oxide-Based Solar-Blind Ultraviolet Photodetectors, Photonics Research, Vol.7, 2019, pp. 381-415.

[126] P. Li, H. Shi, K. Chen, D. Guo, W. Cui, Y. Zhi, S. Wang, Z. Wu, Z. Chen, W. Tang, Construction of GaN/Ga2O3 p-n Junction for An Extremely High Responsivity Self-Powered UV Photodetector, Journal of Materials Chemistry C, Vol.5, 2017, pp. 10562-10570.

[127] R. Raphael, S. Devasia, S. Shaji, E.I. Anila, Effect of Substrate Temperature on the Properties of Spray Deposited Ga2O3 Thin Films, for Solar Blind UV Detector Applications, Optical Materials, Vol.133, 2022, 112915.

[128] S. Chen, Y.-Z. Long, H.-D. Zhang, S.-L. Liu, L.-Z. Liu, J.-C. Zhang, G.-X. Liu, F.-K. Shan, Fabrication of Ultrathin In2O3 Hollow Fibers for UV Light Sensing, Physica Scripta, Vol.89, No.11, 2014, 115808.

[129] G. Tian, Y. Wu, S. Wu, S. Huang, J. Gao, Influence of Mn and Mg Oxides on the Performance of In2O3 Catalysts for CO2 Hydrogenation to Methanol, Chemical Physics Letters, Vol.786, 2022, 139173.

[130] K. Gu, Z. Zhang, K. Tang, J. Huang, M. Liao, L. Wang, Effects of Sputtering Pressure and Oxygen Partial Pressure on Amorphous Ga2O3 Film-Based Solar-Blind Ultraviolet Photodetectors, Applied Surface Science, Vol.605, 2022, 154606.

[131] T. Onuma, S. Saito, K. Sasaki, T. Masui, T. Yamaguchi, T. Honda, M. Higashiwaki, Valence Band Ordering in β-Ga2O3 Studied by Polarized Transmittance and Reflectance Spectroscopy, Japanese Journal of Applied Physics, Vol.54, No.11, 2015, 112601.

[132] T. Kim, B. Jang, S. Lee, W.-Y. Lee, J. Jang, Improved Negative Bias Stress Stability of Sol-Gel-Processed Mg-Doped In2O3 Thin Film Transistors, IEEE Electron Device Letters, Vol.39, No.12, 2018, pp. 1872–1875.

[133] S.-M. Sun, W.-J. Liu, Y.-P. Wang, Y.-W. Huan, Q. Ma, B. Zhu, S.-D. Wu, W.-J. Yu, R.-H. Horng, C.-T. Xia, Q.-Q. Sun, S.-J. Ding, D.W. Zhang, Band Alignment of In2O3/β-Ga2O3 Interface Determined by X-Ray Photoelectron Spectroscopy, Applied Physics Letters, Vol.113, No.3, 2018, 031603.

[134] J. A. Spencer, A. L. Mock, A. G. Jacobs, M. Schubert, Y. Zhang, M. J. Tadjer, A Review of Band Structure and Material Properties of Transparent Conducting and Semiconducting Oxides: Ga2O3, Al2O3, In2O3, ZnO, SnO2, CdO, NiO, CuO, and Sc2O3, Applied Physics Letters, Vol. 9, No.1, 2022, 011315.

[135] I. Isakov, H. Faber, A. D. Mottram, S. Das, M. Grell, A. Regoutz, R. Kilmurray, M. A. McLachlan, D. J. Payne, T. D. Anthopoulos, Quantum Confinement and Thickness-Dependent Electron Transport in Solution-Processed In2O3 Transistors, Advanced Electronic Materials, Vol.6, No.11, 2020, 2000682.

[136] N. Chowdhury, S. Prabakar, H.-K. Choi, Dependency of the Photocatalytic and Photochemical Decomposition of Per- and Polyfluoroalkyl Substances (PFAS) on their Chain Lengths, Functional Groups, and Structural Properties, Water Science & Technology, Vol.84, 2021, pp. 3738–3754.

[137] E. Gagliano, M. Sgroi, P. Falciglia, F. Vagliasindi, P. Roccaro, Removal of Poly- and Perfluoroalkyl Substances (PFAS) from Water by Adsorption: Role of PFAS Chain Length, Effect of Organic Matter and Challenges in Adsorbent Regeneration, Water Research, Vol.171, 2019, 115381.

[138] P. McCleaf, S. Englund, A. Ostlund, K. Lindegren, K. Wiberg, L. Ahrens, Removal Efficiency of Multiple Poly- and Perfluoroalkyl Substances (PFASs) in Drinking Water Using Granular Activated Carbon (GAC) and Anion Exchange (AE) Column Tests, Water Research, Vol.120, 2017, pp. 77–87.

[139] F. Li, J. Duan, S. Tian, H. Ji, Y. Zhu, Z. Wei, D. Zhao, Short-Chain Per- and Polyfluoroalkyl Substances in Aquatic Systems: Occurrence, Impacts and Treatment,

Chemical Engineering Journal, Vol.380, 2020, 122506.

[140] B. Gomez-Ruiz, P. Ribao, N. Diban, M.J. Rivero, I. Ortiz, A. Urtiaga, Photocatalytic Degradation and Mineralization of Perfluorooctanoic Acid (PFOA) Using a Composite TiO2-rGO Catalyst, Journal of Hazardous Materials, Vol.344, 2018, pp. 950–957.

[141] Y. Wen, Á. Rentería-Gómez, G. S. Day, M. F. Smith, T.-H. Yan, R. O. K. Ozdemir, O. Gutierrez, V. K. Sharma, X. Ma, H.-C. Zhou, Integrated Photocatalytic Reduction and Oxidation of Perfluorooctanoic Acid by Metal-Organic Frameworks: Key Insights into the Degradation Mechanisms, Journal of the American Chemical Society, Vol.144, 2022, pp. 11840–11850.

[142] E. Y. Fernando, D. Sarkar, C. Rodwihok, A. Satpathy, J. Zhang, R. Rahmati, R. Datta, C. Christodoulatos, M. Boufadel, S. Larson, Z. Zhang, Unrefined and Milled Ilmenite as a Cost-Effective Photocatalyst for UV-Assisted Destruction and Mineralization of PFAS, Materials, Vol.17, 2024, 3801.

[143] J. Wang, S. Wang, Reactive Species in Advanced Oxidation Processes: Formation, Identification and Reaction Mechanism, Chemical Engineering Journal, Vol.401, 2020, 126158.

[144] G. Yu, Y. Wang, H. Cao, H. Zhao, Y. Xie, Reactive Oxygen Species and Catalytic Active Sites in Heterogeneous Catalytic Ozonation for Water Purification, Environmental Science & Technology, Vol.54, 2020, pp. 5931–5946.

[145] B. Xu, J. L. Zhou, A. Altaee, M. B. Ahmed, M. A. H. Johir, J. Ren, X. Li, Improved Photocatalysis of Perfluorooctanoic Acid in Water and Wastewater by Ga2O3/UV System Assisted by Peroxymonosulfate, Chemosphere, Vol.239, 2020, 124722.

[146] J. Wang, C. Cao, Y. Zhang, Y. Zhang, L. Zhu, Underneath Mechanisms into the Super Effective Degradation of PFOA by BiOF Nanosheets with Tunable Oxygen Vacancies on Exposed (101) Facets, Applied Catalysis B: Environment and Energy, Vol.286, 2021, 119911.

[147] M. Samy, M. G. Ibrahim, M. Fujii, K. E. Diab, M. ElKady, M. Gar Alalm, CNTs/MOF-808 Painted Plates for Extended Treatment of Pharmaceutical and Agrochemical Wastewaters in a Novel Photocatalytic Reactor, Chemical Engineering Journal, Vol.406, 2021, 127152.

[148] M. H. Cao, B. B. Wang, H. S. Yu, L. L. Wang, S. H. Yuan, J. Chen, Photochemical Decomposition of Perfluorooctanoic Acid in Aqueous Periodate with VUV and UV Light Irradiation, Journal of Hazardous Materials, Vol.179, 2010, pp. 1143–1146.

[149] Z. Li, P. Zhang, T. Shao, X. Li, In2O3 Nanoporous Nanosphere: A Highly Efficient Photocatalyst for Decomposition of Perfluorooctanoic Acid, Applied Catalysis B: Environment and Energy, Vol.125, 2012, pp. 350–357.

[150] X. Liu, W. Wei, J. Xu, D. Wang, L. Song, B.-J. Ni, Photochemical Decomposition of Perfluorochemicals in Contaminated Water, Water Research, Vol.186, 2020, 116311.

[151] Z. Song, H. Tang, N. Wang, L. Zhu, Reductive Defluorination of Perfluorooctanoic Acid by Hydrated Electrons in a Sulfite Mediated UV Photochemical System, Journal of Hazardous Materials, Vol.262, 2013, pp. 332–338.

[152] M. J. Bentel, Y. Yu, L. Xu, Z. Li, B. M. Wong, Y. Men, J. Liu, Defluorination of Per- and Polyfluoroalkyl Substances (PFASs) with Hydrated Electrons: Structural Dependence and Implications to PFAS Remediation and Management, Environmental Science & Technology, Vol.53, 2019, pp. 3718–3728.

[153] X. Li, P. Zhang, L. Jin, T. Shao, Z. Li, J. Cao, Efficient Photocatalytic Decomposition of Perfluorooctanoic Acid by Indium Oxide and Its Mechanism, Environmental Science & Technology, Vol.46, 2012, pp. 5528–5534.

[154] E. Banayan Esfahani, F. Asadi Zeidabadi, S. Zhang, M. Mohseni, Photo-Chemical/Catalytic Oxidative/Reductive Decomposition of Per- and Poly-Fluoroalkyl Substances (PFAS), Decomposition Mechanisms and Effects of Key Factors: A Review, Environmental Science: Water Research & Technology, Vol.8, 2022, pp. 698–728.

[155] L. Eberson, Electron-Transfer Reactions in Organic Chemistry, Advances in Physical Organic Chemistry, Vol.18, 1982, pp. 79–185.

[156] H. Zhang, C. Xie, L. Chen, J. Duan, F. Li, W. Liu, Different Reaction Mechanisms of SO4−2 ● and OH● with Organic Compound

Interpreted at Molecular Orbital Level in Co(II)/Peroxymonosulfate Catalytic Activation System, Water Research, Vol.229, 2023, 119392.

[157] J. Wang, S. Wang, Activation of Persulfate (PS) and Peroxymonosulfate (PMS) and Application for the Degradation of Emerging Contaminants, Chemical Engineering Journal, Vol.334, 2018, pp. 1502–1517.

[158] F. C. Moreira, R. A. R. Boaventura, E. Brillas, V. J. P. Vilar, Electrochemical Advanced Oxidation Processes: A Review on Their Application to Synthetic and Real Wastewaters, Applied Catalysis B: Environment and Energy, Vol.202, 2017, pp. 217–261.

[159] D. Dey, T. Shafi, S. Chowdhury, B. Dubey, R. Sen, Progress and Perspectives on Carbon-Based Materials for Adsorptive Removal and Photocatalytic Degradation of Perfluoroalkyl and Polyfluoroalkyl Substances (PFAS), Chemosphere, Vol.351, 2024, 141164.

Contribution of Individual Authors to the Creation of a Scientific Article (Ghostwriting Policy)

Prof. Dr. Delia Teresa Sponza and Post-Dr. Rukiye Öztekin took an active role in every stage of the preparation of this article.

The authors equally contributed in the present research, at all stages from the formulation of the problem to the final findings and solution.

Sources of Funding for Research Presented in a Scientific Article or Scientific Article Itself

The experimental phases of this research study were conducted at the National Research Council (NRC) of Canada, Research Centers, Ontario, Canada. The authors would like to thank this body for providing financial support.

Conflict of Interest

The authors have no conflicts of interest to declare that are relevant to the content of this article.

APPENDIX

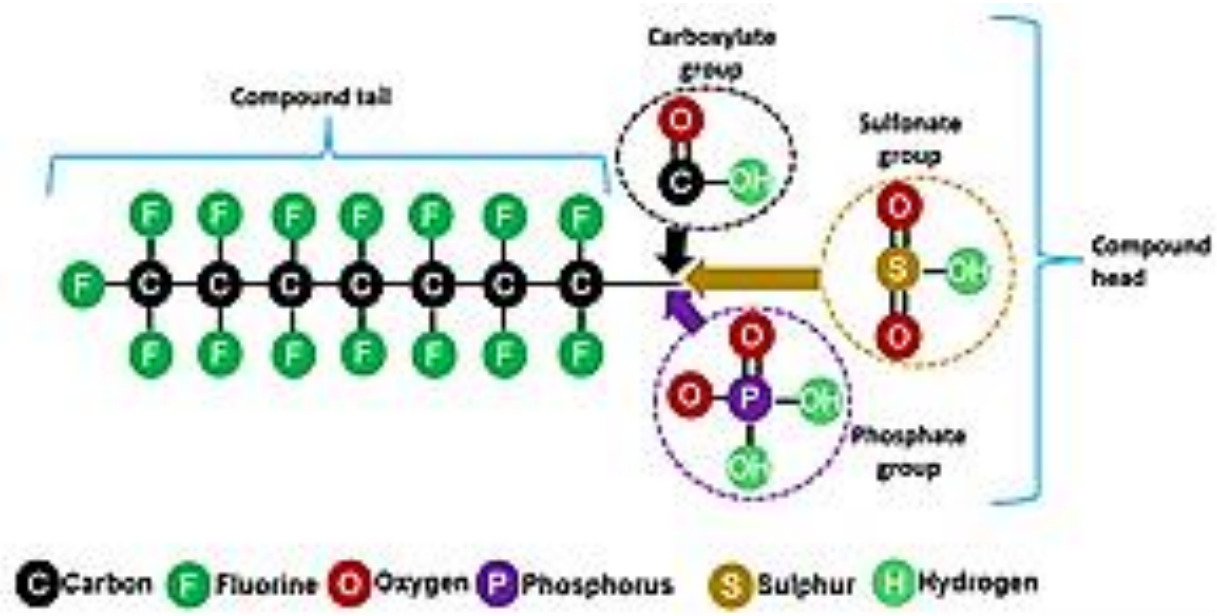

(a)

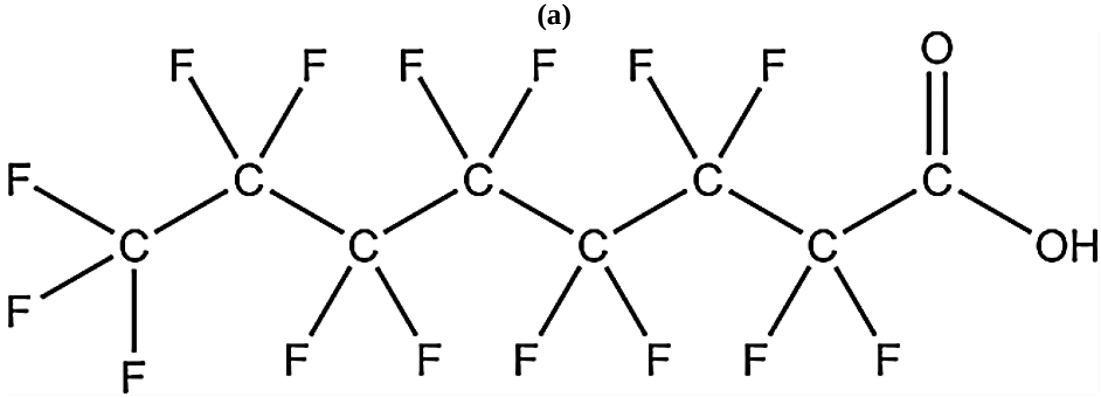

(b)

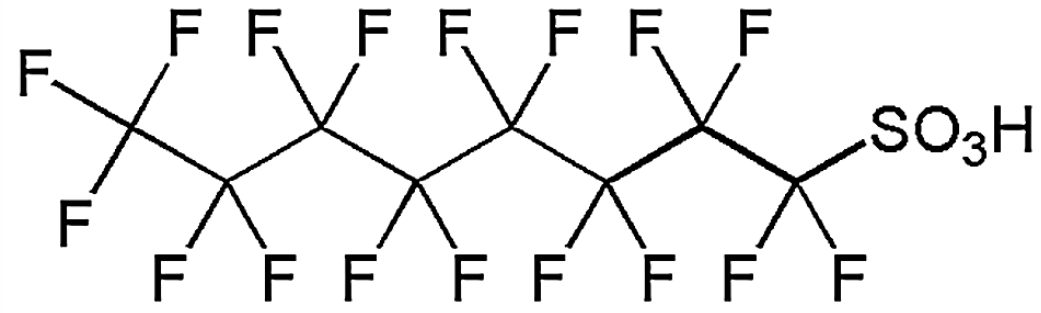

(c)

Fig. 1: Chemical structures of (a) PFAS, (b) PFOA and (c) PFOS, respectively

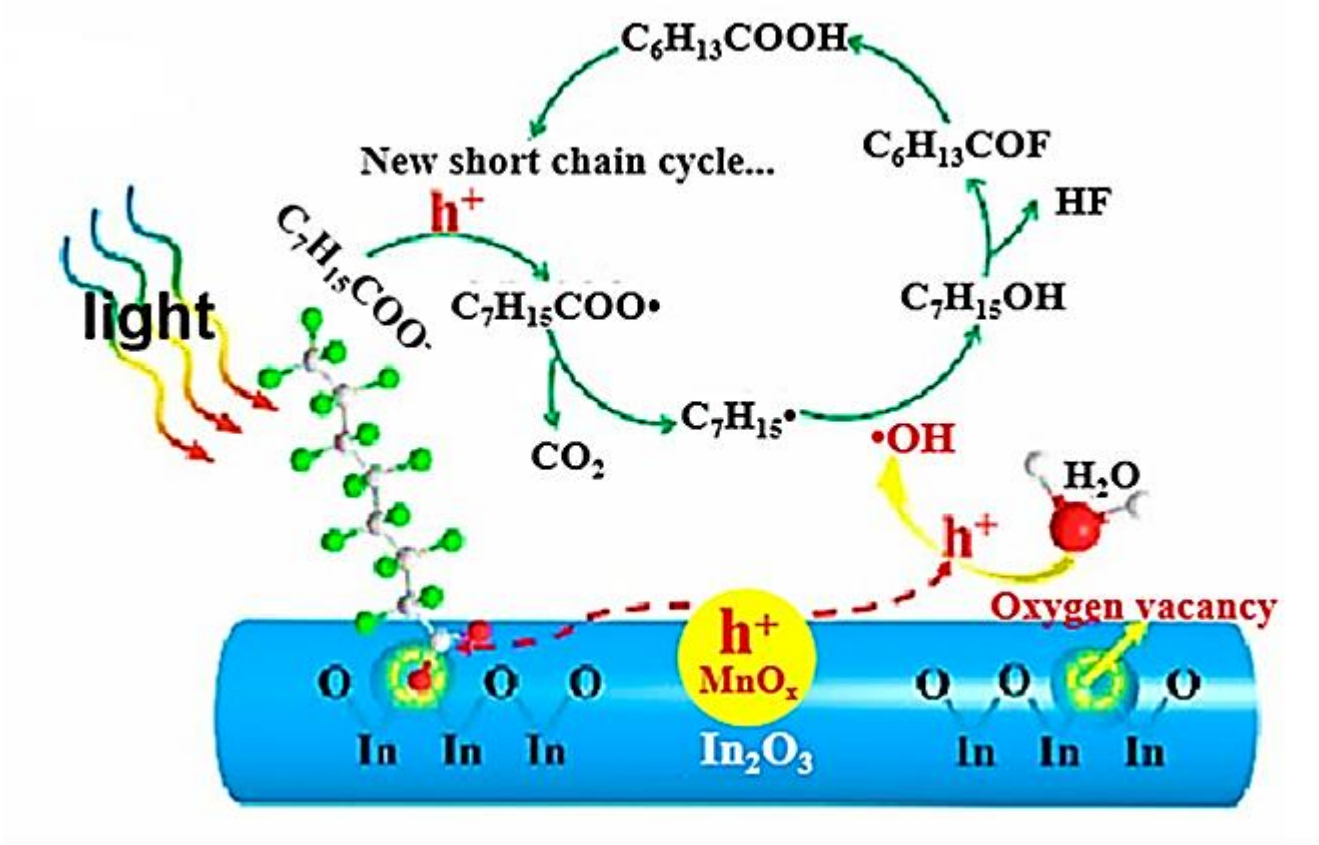

Fig. 2: MnOx modification enhances the photocatalytic degradation of PFOA on In2O3 by introducing oxygen vacancies and generating more ROS, [44]

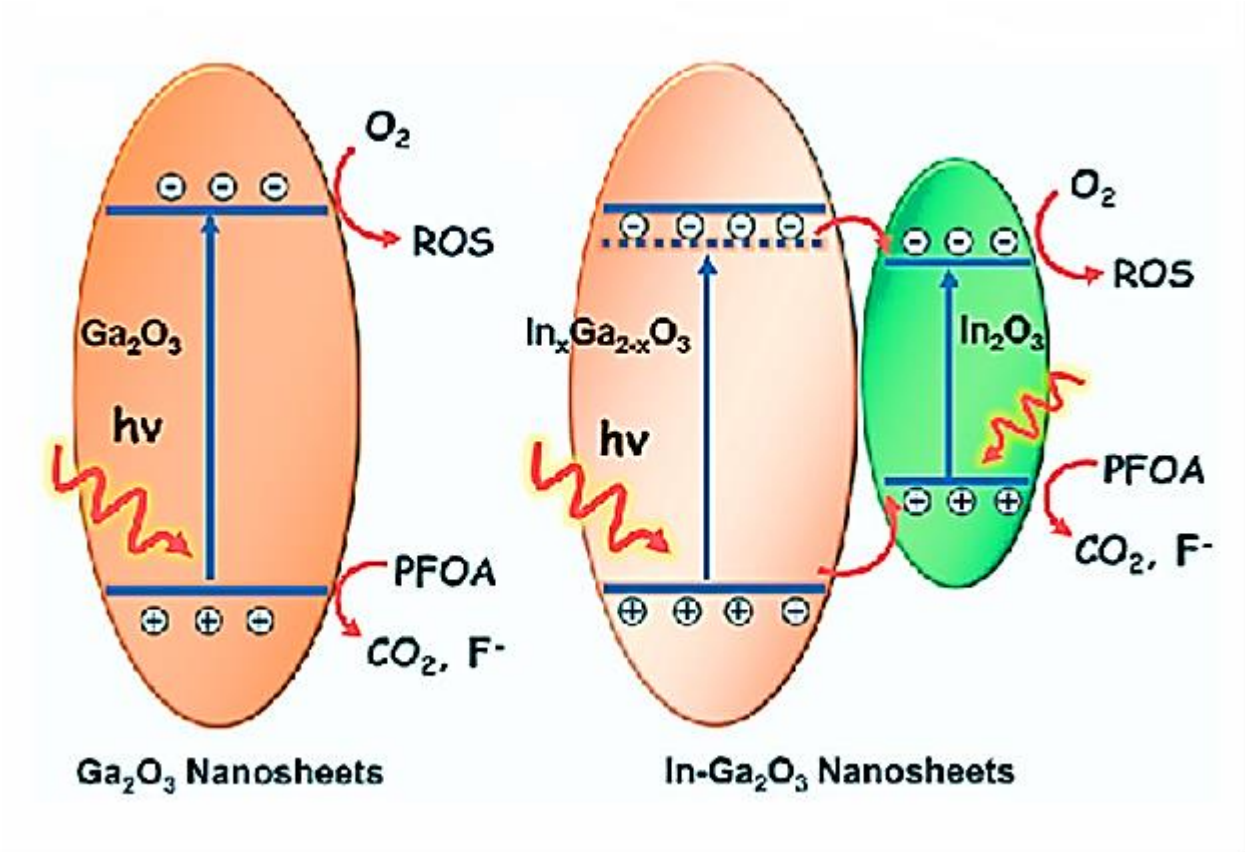

Fig. 3: The band structures and photodegradation mechanism of PFOA on Ga2O3, with and without In-doping, [48]

Table 1. The values of retention time, correlation coefficient, recovery, LOD and LOQ of PFOA and PFOS

Compound name	**Retention time (min)**	**Correlation coefficient (R^2)**	**Recovery (%)**	**LOD (ng/g)**	**LOQ (ng/g)**
PFOA	259	0.9999	94.8-101.6	0.012	0.040
PFOS	266	0.9999	96.2-99.4	3.10^{-4}	0.001

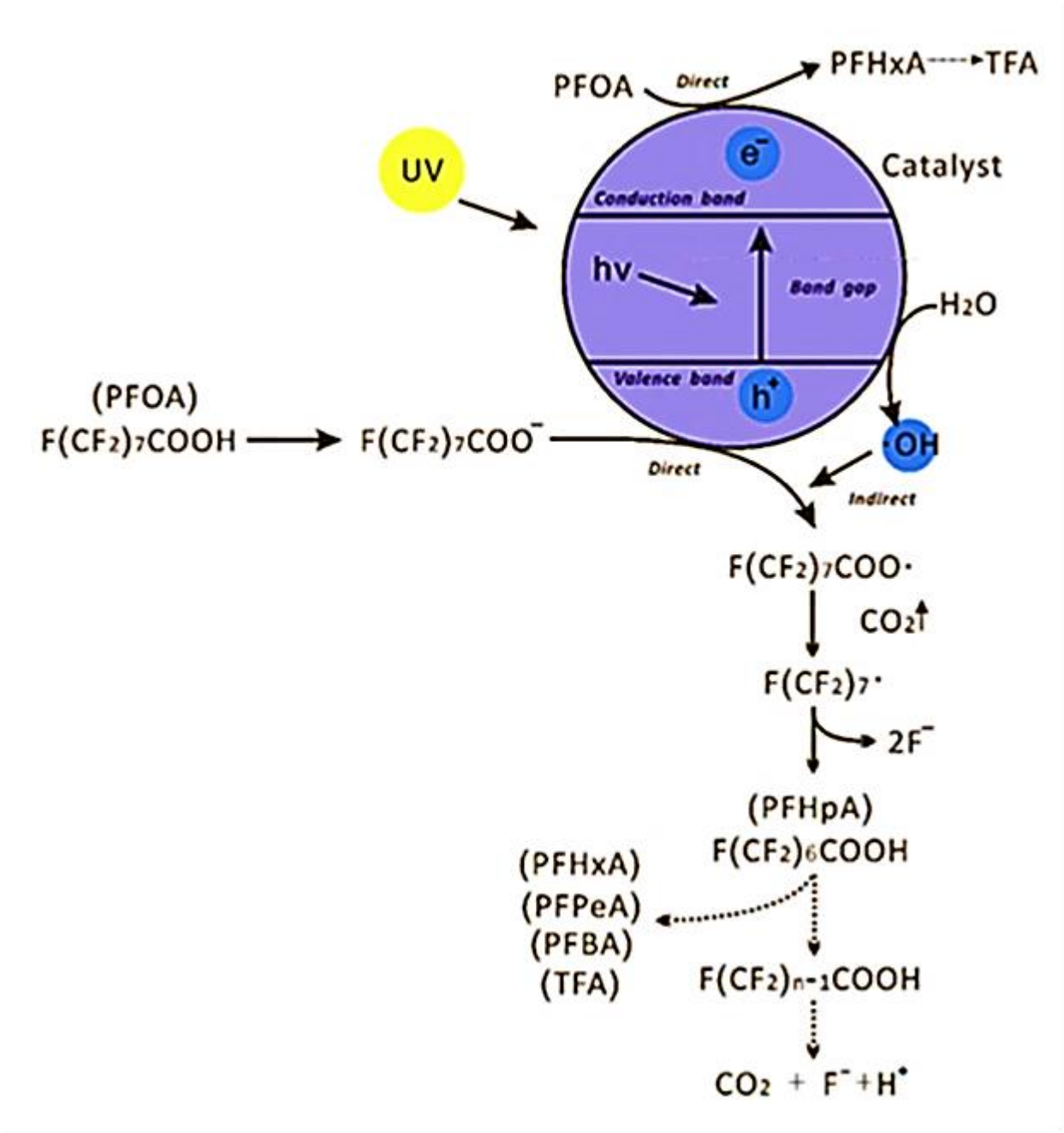

Fig. 4: The mechanism of photocatalytic degradation process for PFOA

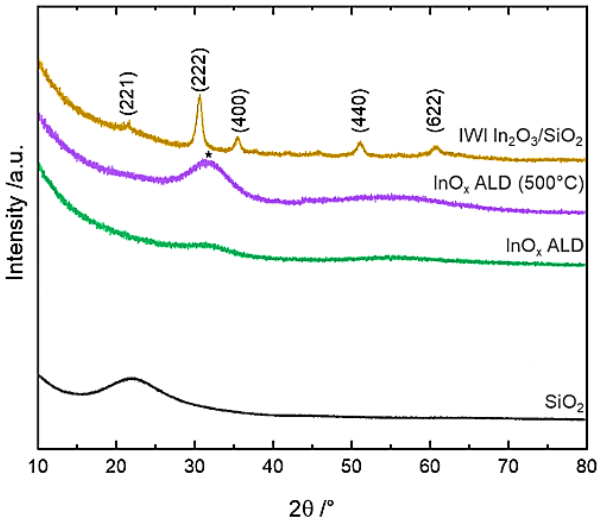

(a)

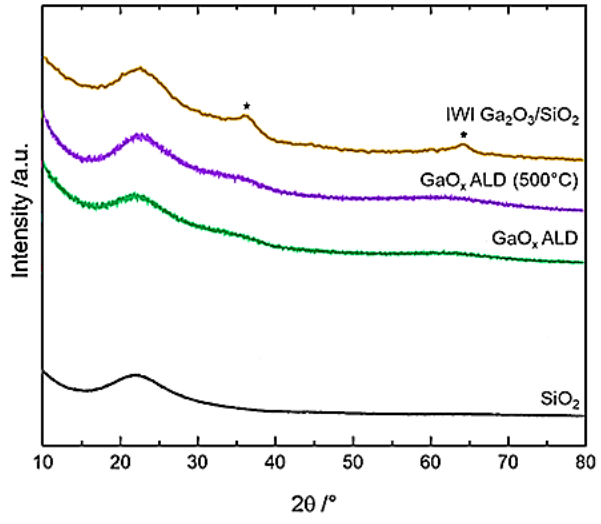

(b)

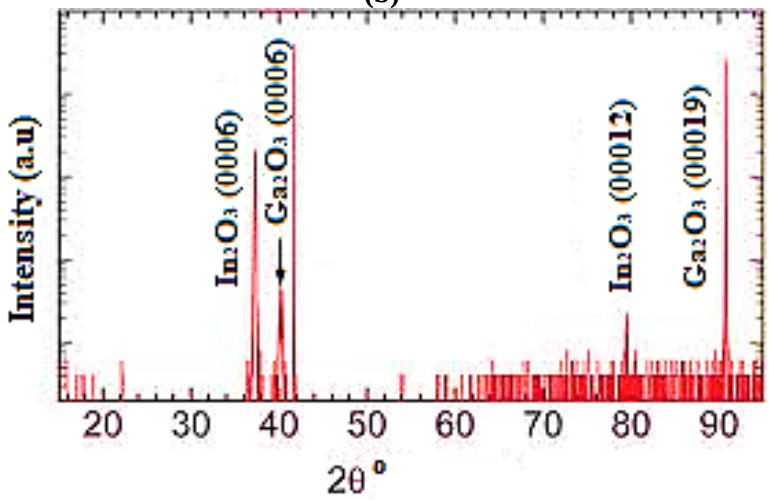

Fig. 5: XRD images of (a) In2O3 ALD, (b) Ga2O3 ALD and (c) In2O3/Ga2O3 nanocomposite on SiO2 (500°C) indicate calcination at 500°C in 20% O2 for 3 h. In2O3(27 wt%)/SiO2 and Ga2O3(19 wt%)/SiO2 were synthesized via incipient wetness impregnation (IWI)

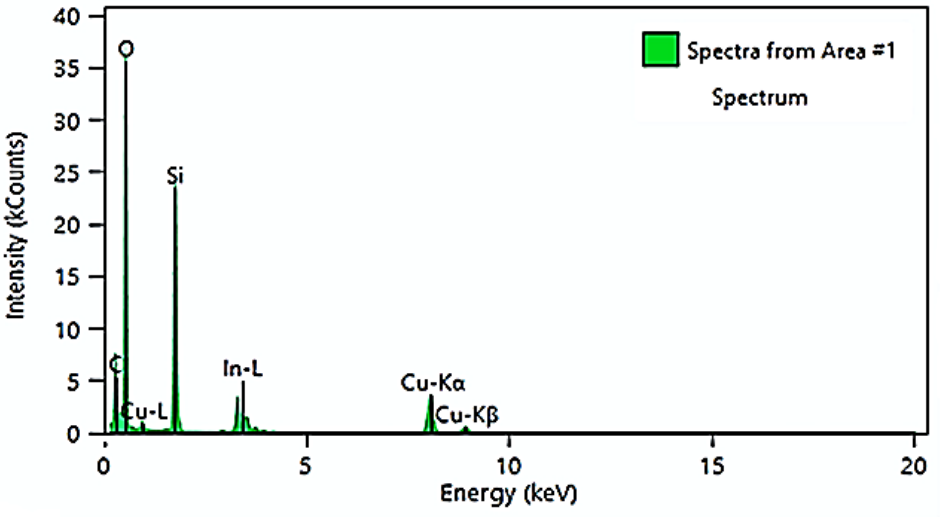

(a)

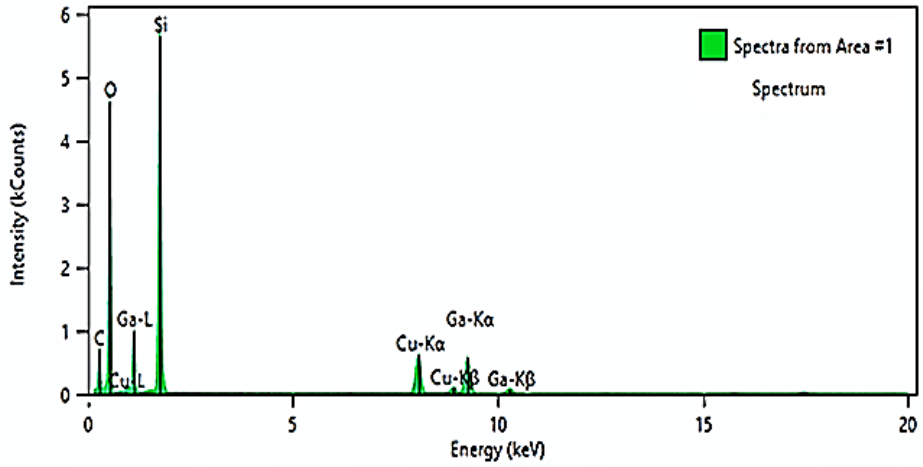

(b)

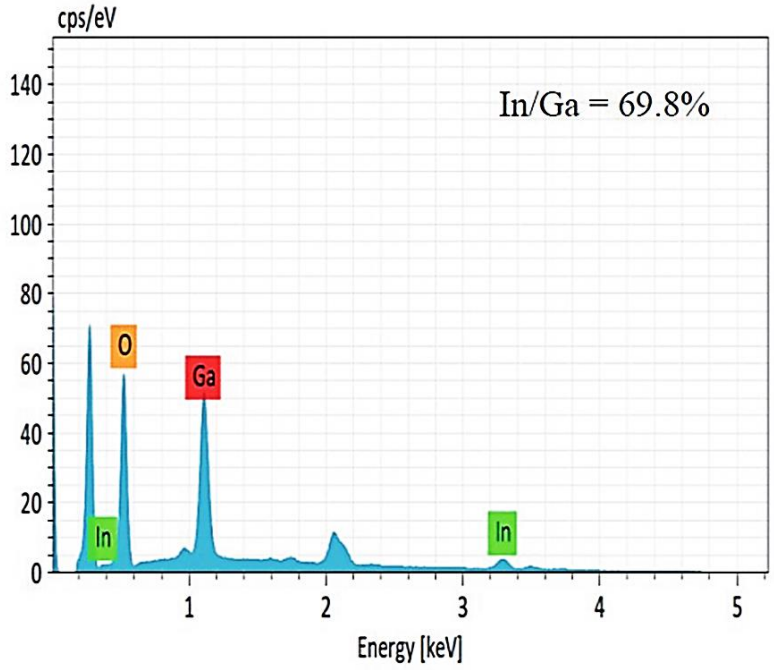

(c)

Fig. 6: EDX mapping of (a) In2O3 and (b) Ga2O3 and (c) In2O3/Ga2O3 nanocomposites, respectively

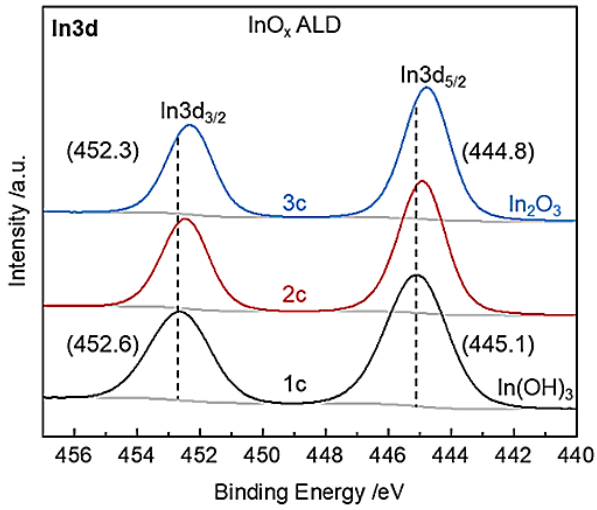

(a)

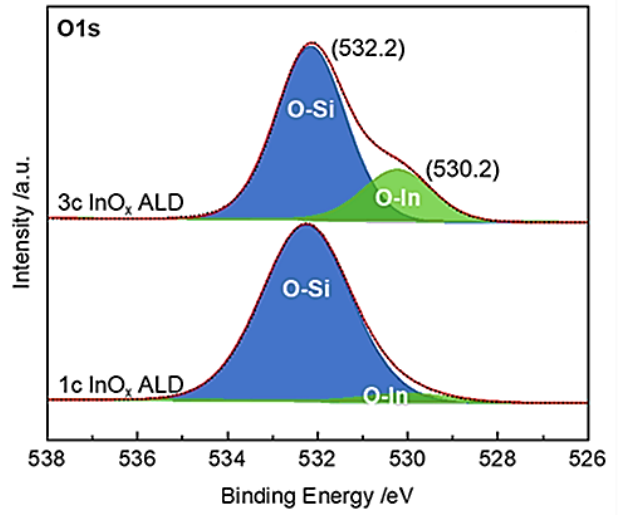

(b)

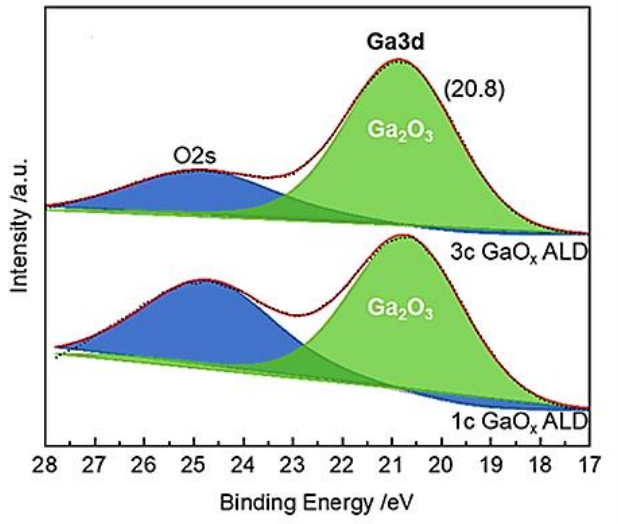

(c)

Fig. 7: XPS scans of the (a) In3d, (b) O1s and (c) Ga3d regions of a s-deposited 1–3 cycle. (a-b) In2O3 ALD on SiO2, and (c) Ga2O3 on SiO2, respectively. Surveys were corrected to the C1s orbital peak at 284.8 eV. Intensities were normalized to values between 0 and 1 for comparison

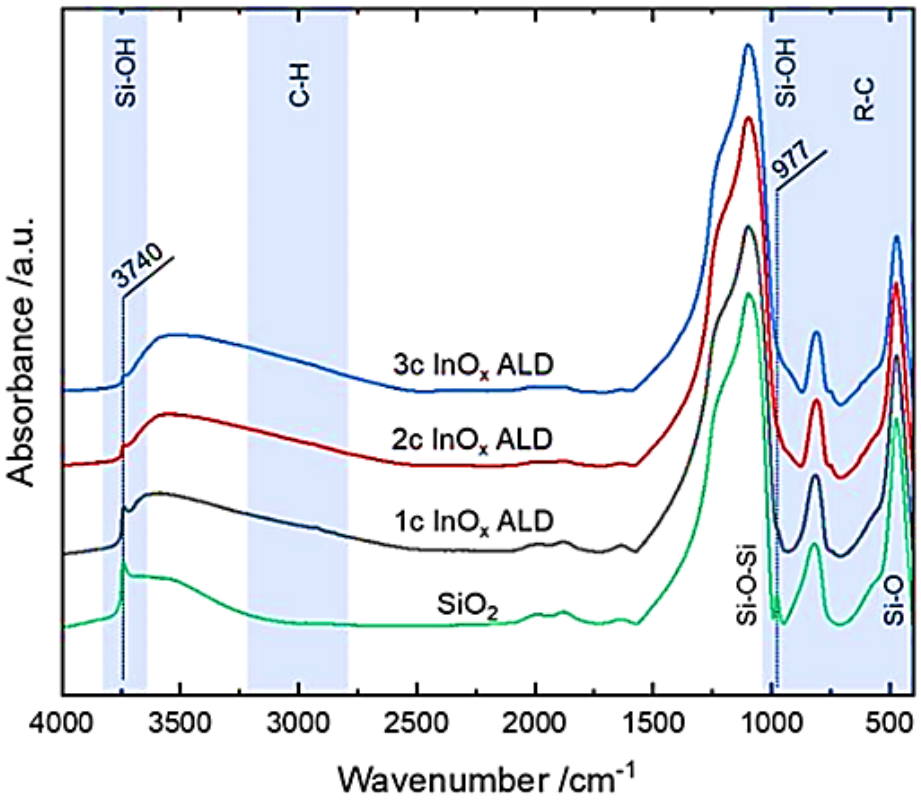

(a)

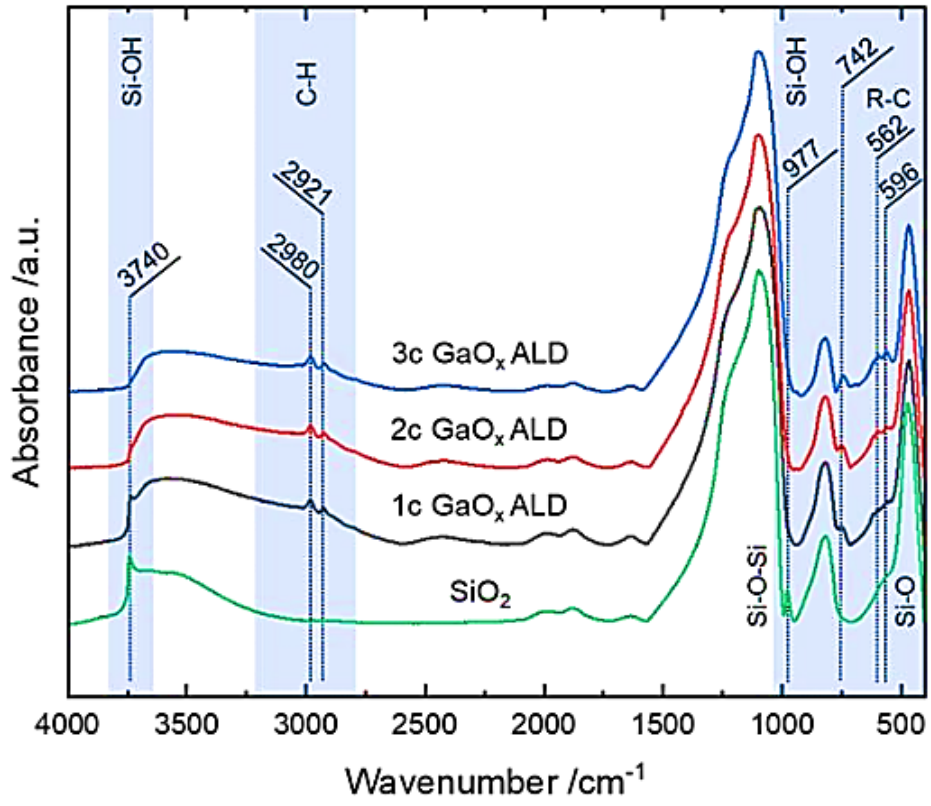

(b)

Fig. 8: FTIR spectra of (a) In2O3 and (b) Ga2O3 nanocomposites between 4000-400 cm-1 wavenumbers of 1-3 cycle on silica using TMX (X=G, I) and water 150oC, respectively

Table 2. Mass fractions of In2O3 and Ga2O3 on SiO2 with in three cycles of atomic layer deposition using TMX (X=G, I) and water at 150oC. Values are calculated from thermogravimetric data (MSB) and compared to ICP-OES data. Mass-fraction(frac.) = Δm / (m0+ m)

Samples	**Mass Fraction (%)**	*** M_2O_3 Fraction (%)**	**** $M(OH)_2$ Fraction (%)**	**Mass Fraction (%) (ICP-OES)**
1 cycle	27.90% In_2O_3	23.10 (In)	21.50 (In)	21.10 (In)
3 cycles	56.30% In_2O_3	46.60 (In)	43.40 (In)	48.50 (In)
1 cycle	19.60 % Ga_2O_3	14.50 (Ga)	13.10 (Ga)	14.60 (Ga)
3 cycles	35.40 % Ga_2O_3	26.30 (Ga)	23.80 (Ga)	26.00 (Ga)

Note: * calculated from in-situ mass-fraction, assuming M_2O_3 species being deposited.
** Assuming $M(OH)_2$ species being deposited on a single OH-group each.

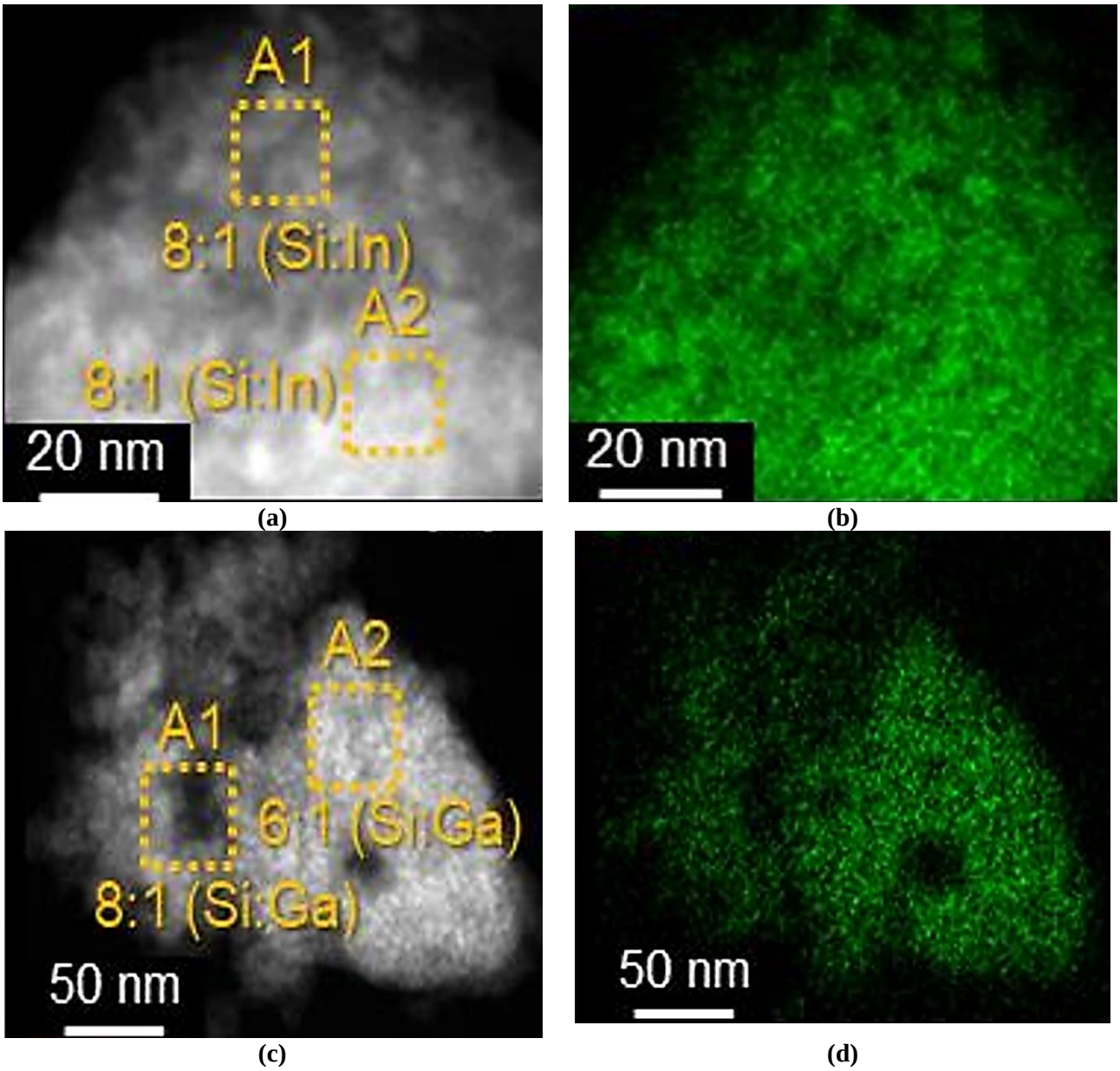

Fig. 9: STEM images of (a-b) In2O3 and (c-d) Ga2O3 nanocomposites

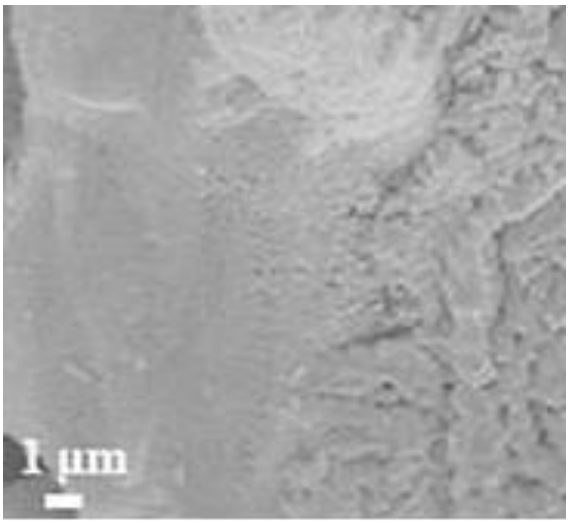

(a) (image size: 1 µm)

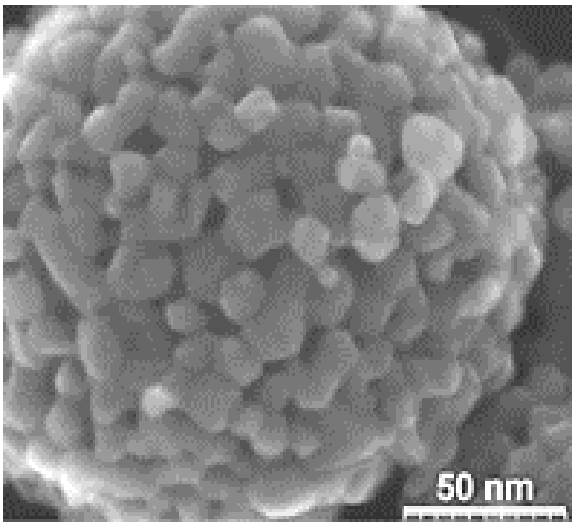

(b) (image size: 50 nm)

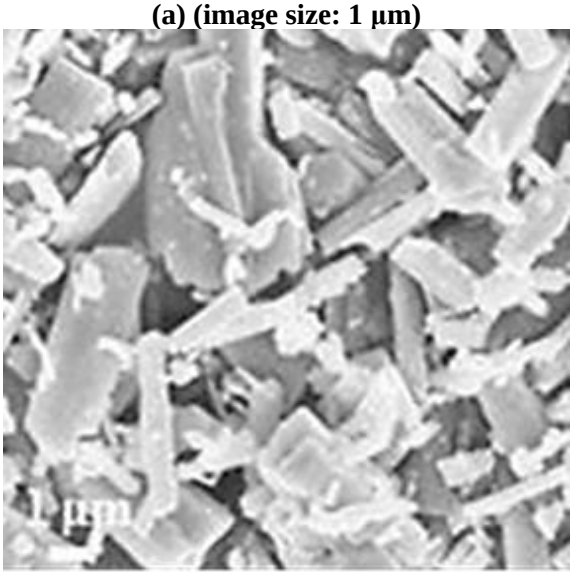

(c) (image size: 1 µm)

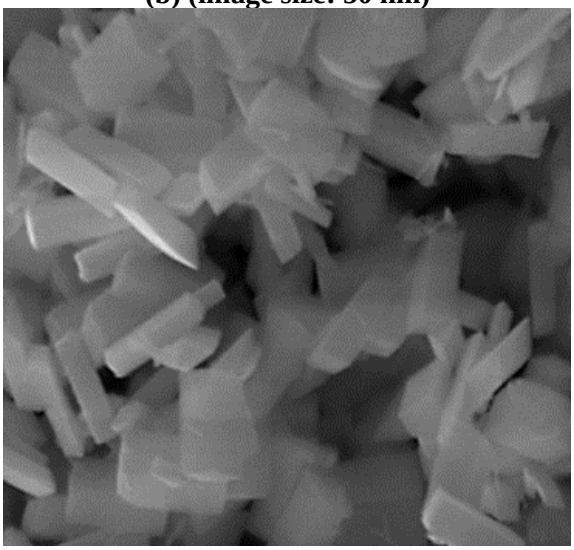

(d) (image size: 50 nm)

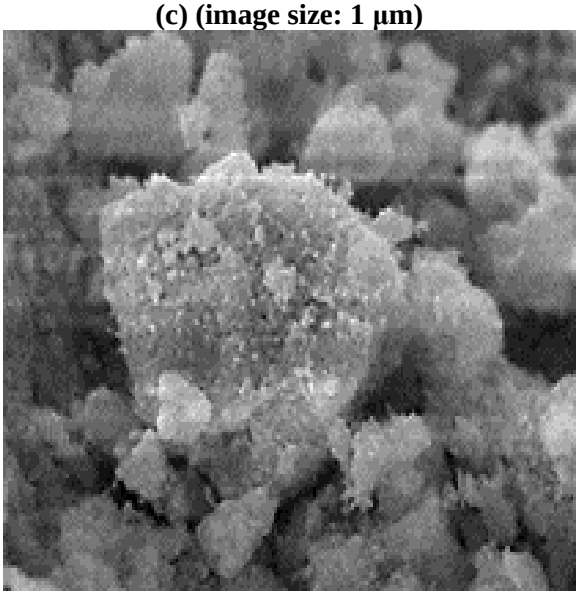

(e) (image size: 2 µm)

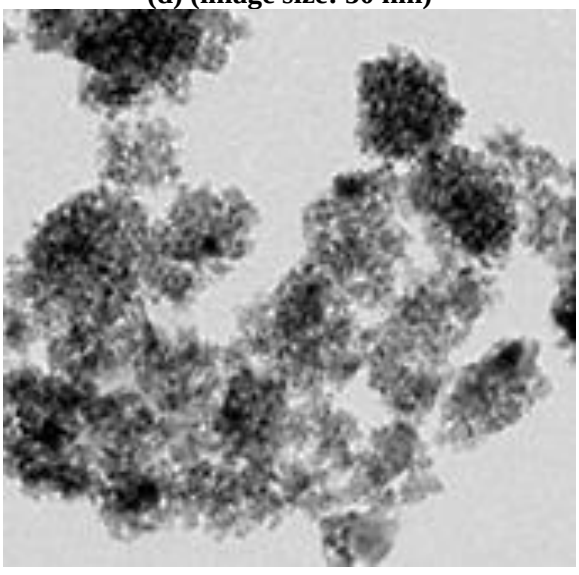

(f) (image size: 50 nm)

Fig. 10: FESEM images of (a-b) In2O3, (c-d) Ga2O3 and (e-f) In2O3/Ga2O3 nanocomposites, respectively

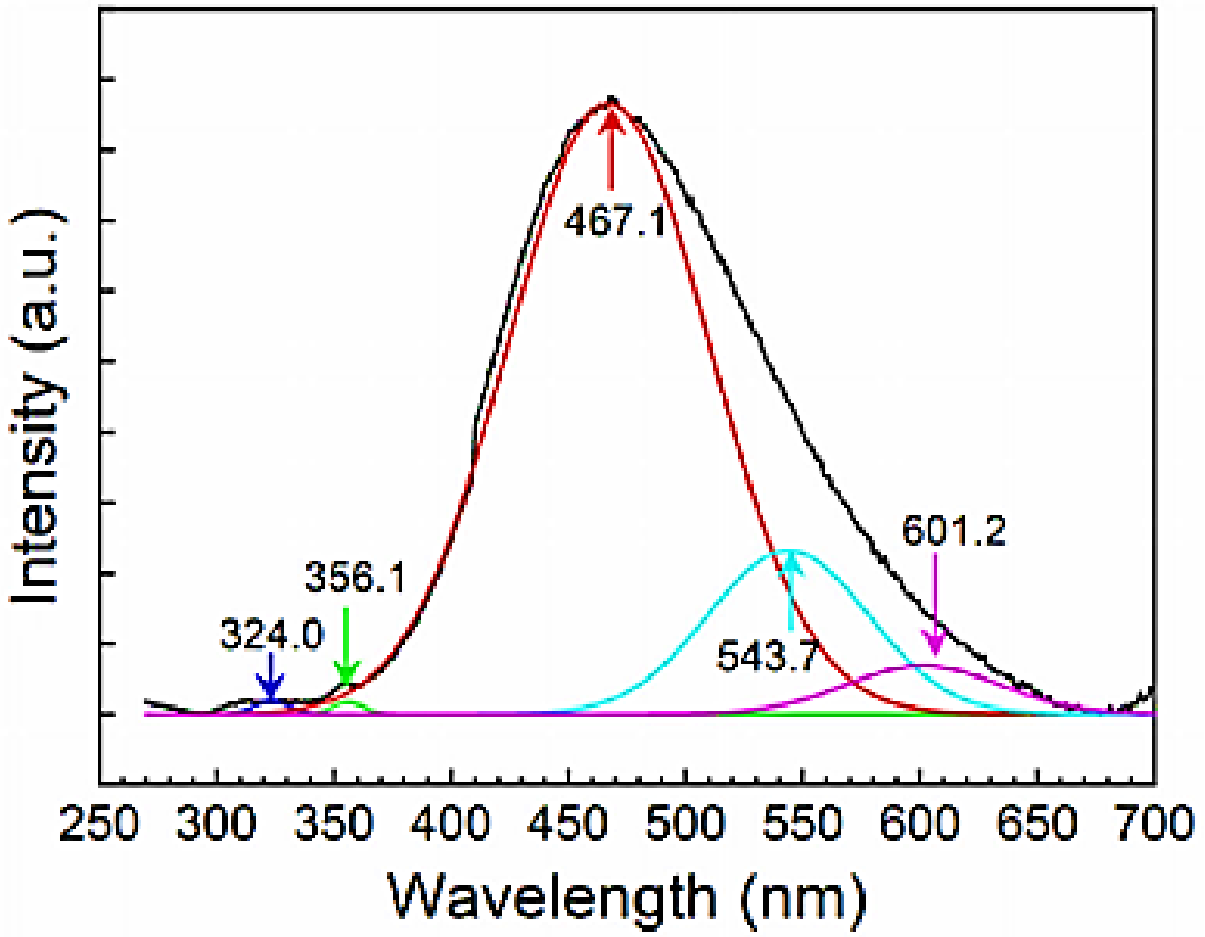

Fig. 11: PL spectra of In2O3/Ga2O3 nanocomposites

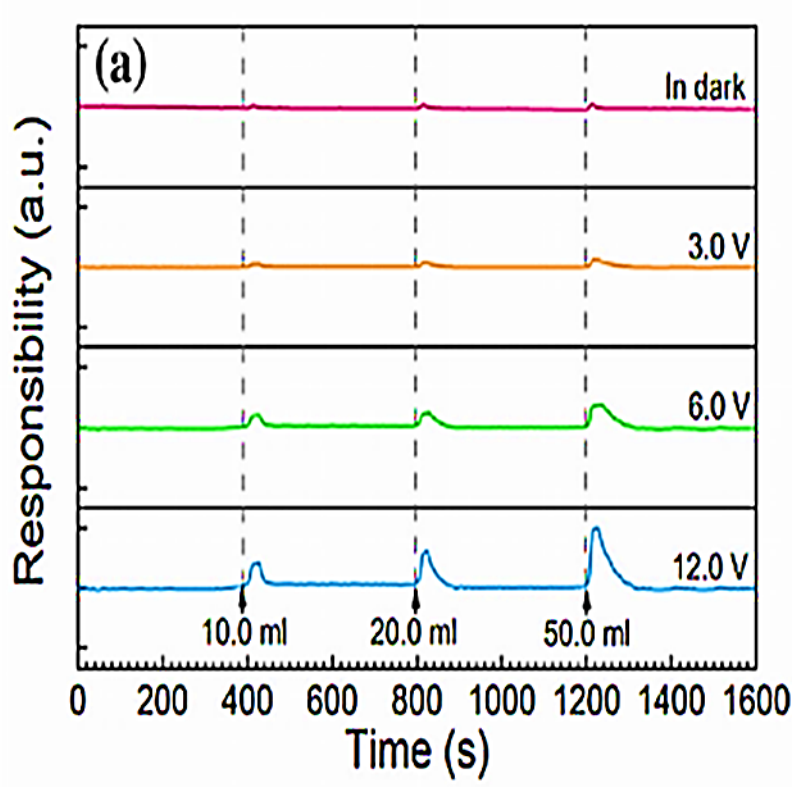

(a)

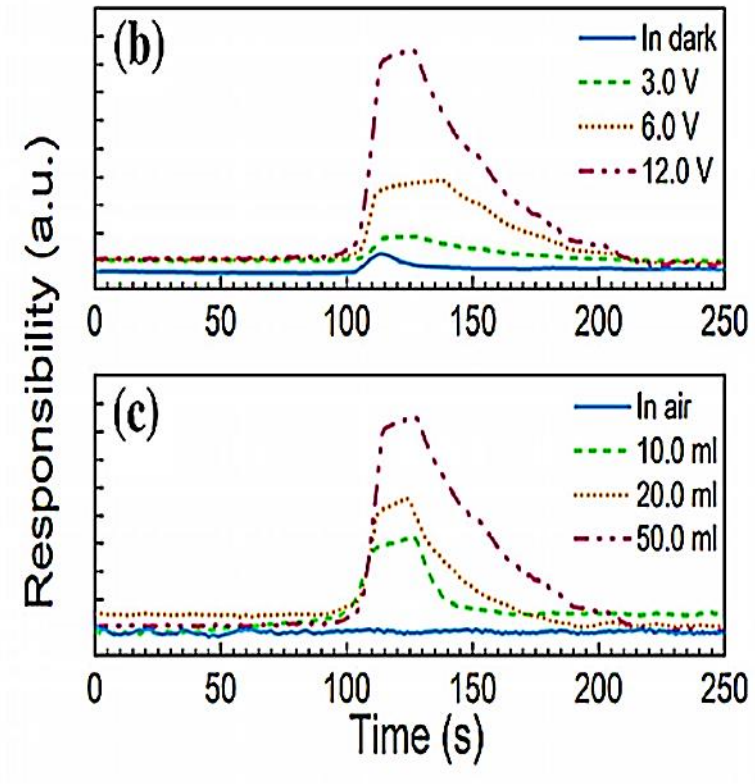

(b) – (c)

Fig. 12: (a) Oxygen gas sensing performance, a under different ultraviolet light intensities and amount of oxygen, (b) in 50 ml oxygen with various light intensities, (c) under 12.0 V ultraviolet light with various amount of oxygen, respectively

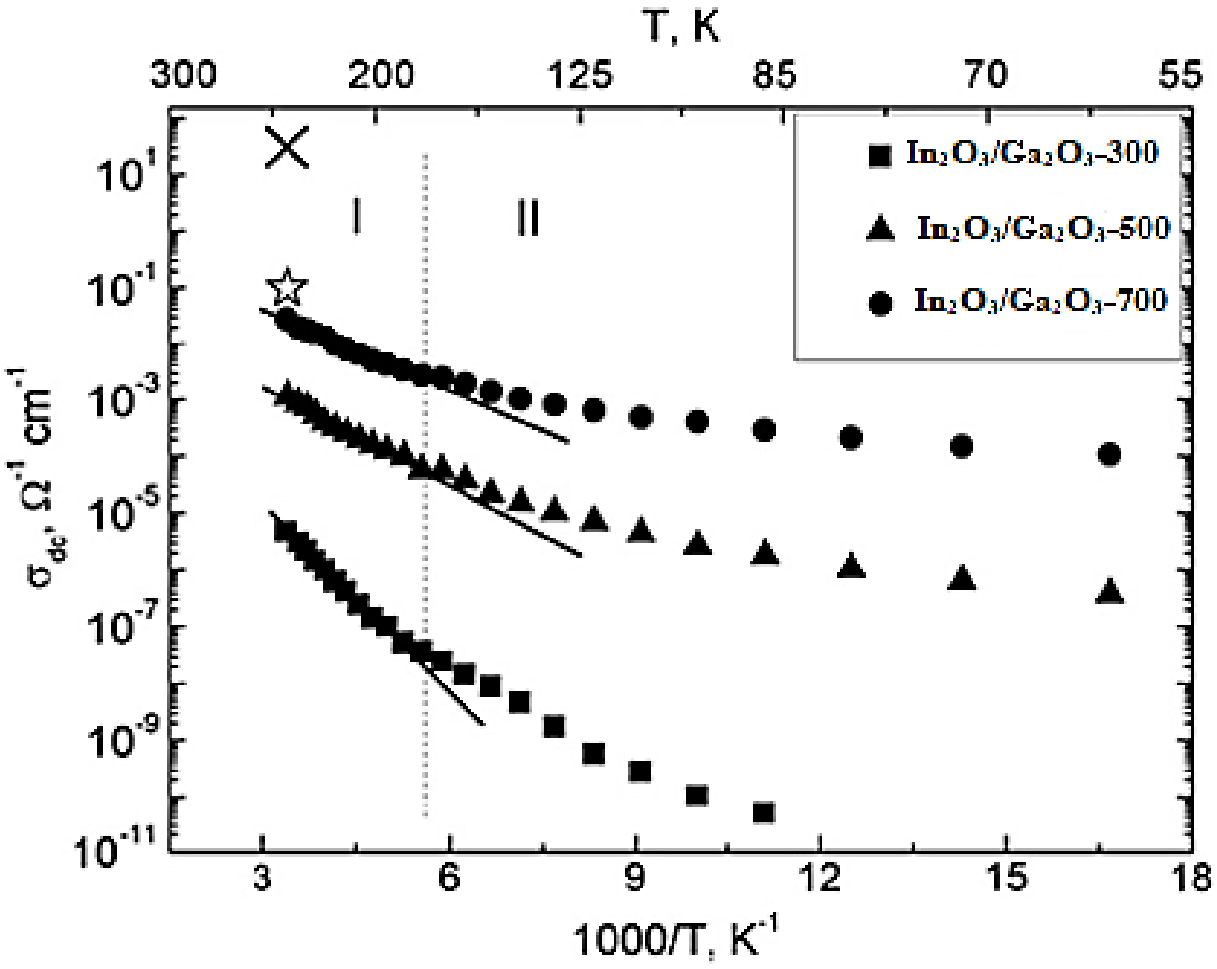

Fig. 13: The temperature dependencies of conductivity of the In2O3/Ga2O3 nanocomposite

Table 3. Activation energies and values of the Mott conduction parameters

Sample	E_A **(eV)**	T_0 **(K)**	σ_0` **(**Ω^{-1} **cm**$^{-1}$**)**	$N(E_F)$**, (eV**$^{-1}$ **cm**$^{-3}$**)**	R_{hop} **(nm)**	W_{hop} **(meV)**
In_2O_3/Ga_2O_3-300	0.16	$4.3x10^8$	$7.4x10^{10}$	$0.49x10^{18}$	15.4	133
In_2O_3/Ga_2O_3-500	0.10	$2x10^7$	$5x10^3$	$1.04x10^{19}$	7.2	62
In_2O_3/Ga_2O_3-700	0.07	$3.7x10^6$	$4.4x10^3$	$0.56x10^{20}$	4.7	41

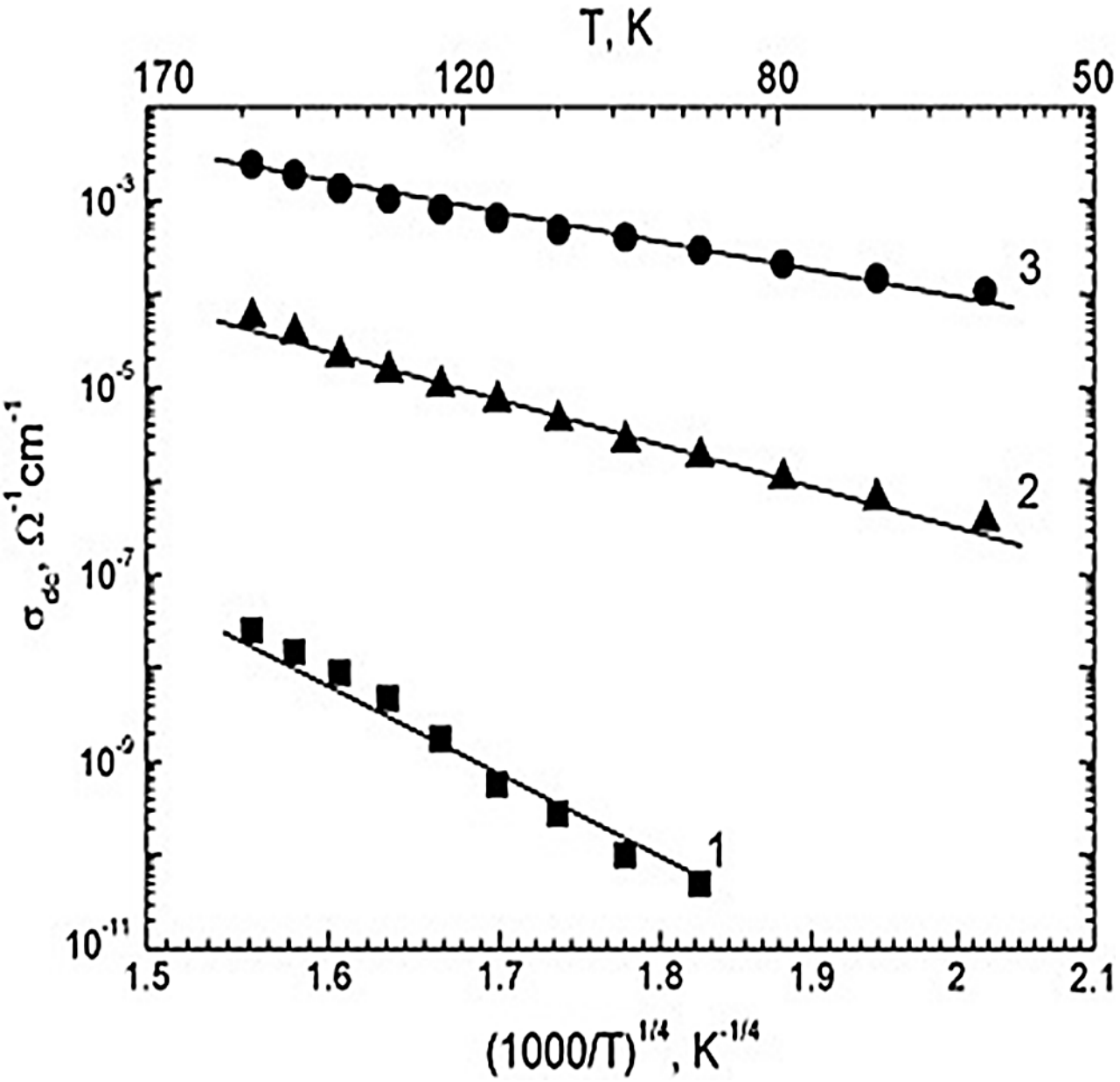

Fig. 14: The temperature dependencies of conductivity of the In2O3/Ga2O3 nanocomposite samples plotted as ln (σ T1/2) vs. T− 1/4 in the range of low temperature: (1) In2O3/Ga2O3 nanocomposite -300, T < 200oK, (2) In2O3/Ga2O3 nanocomposite -500, T < 170oK, (3) In2O3/Ga2O3 nanocomposite -700, T < 160oK

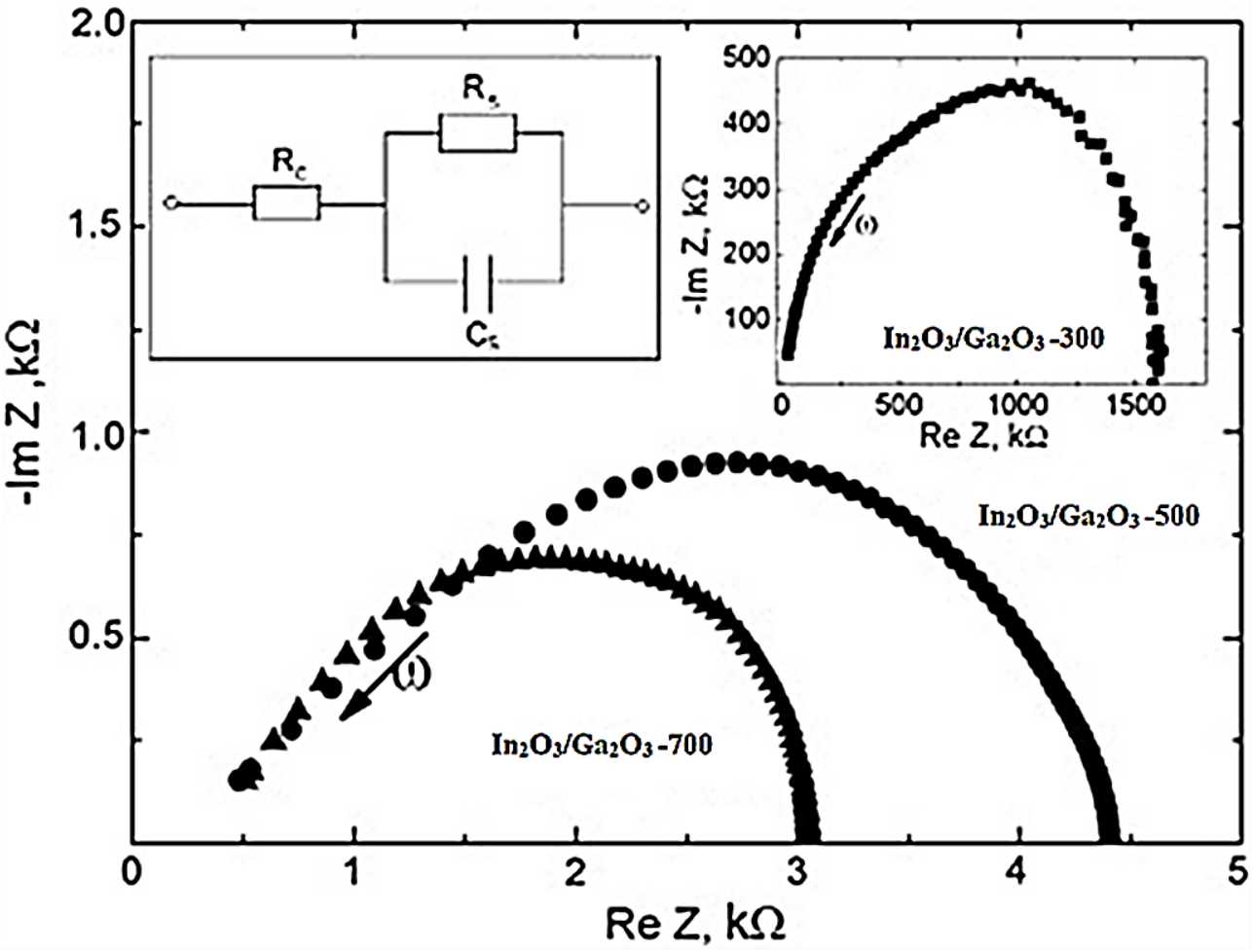

Fig. 15: Cole–Cole plot of the In2O3/Ga2O3 nanocomposites samples

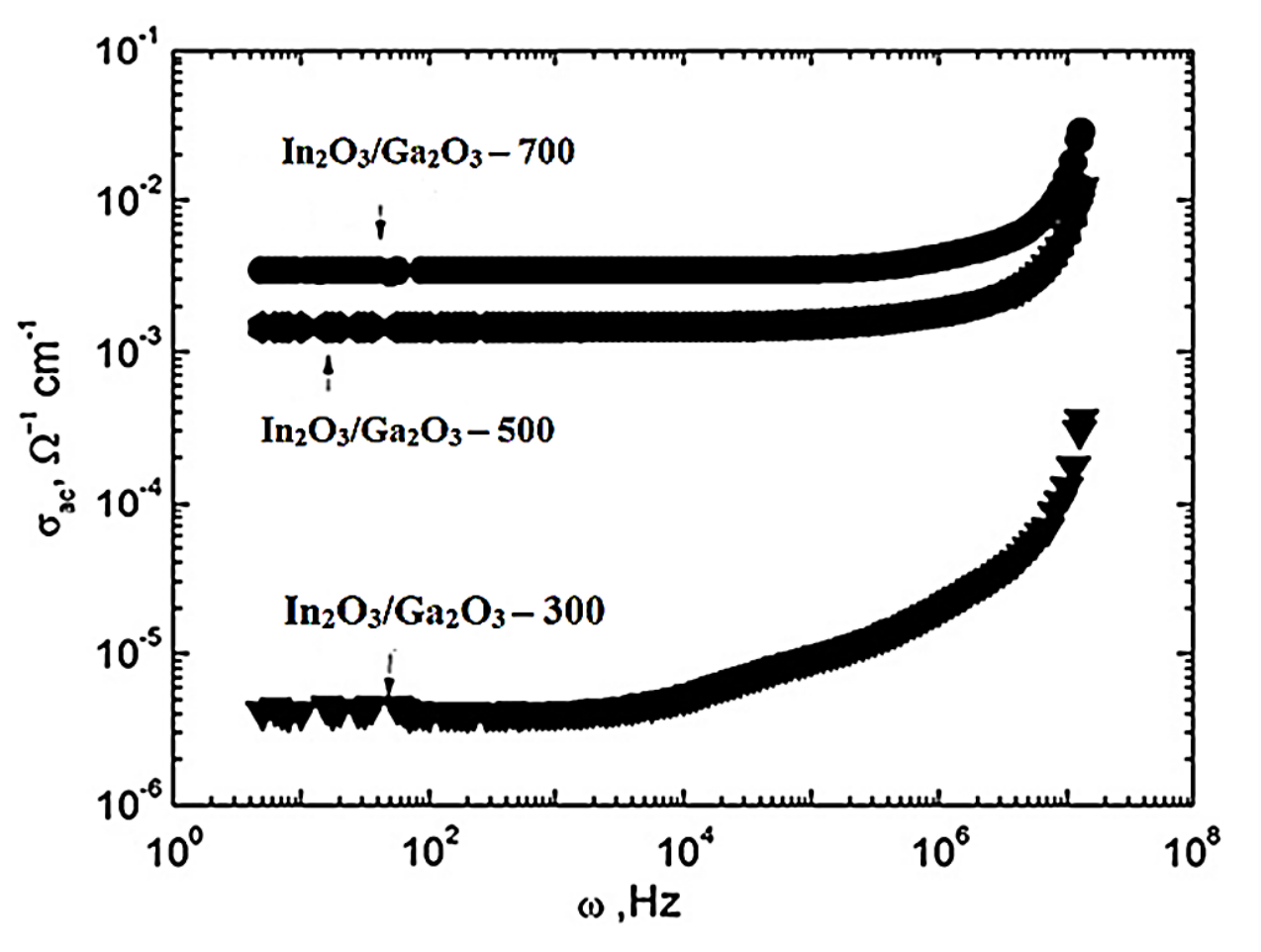

Fig. 16: The frequency dependencies of conductivity measured at T=300oK for In2O3/Ga2O3 samples

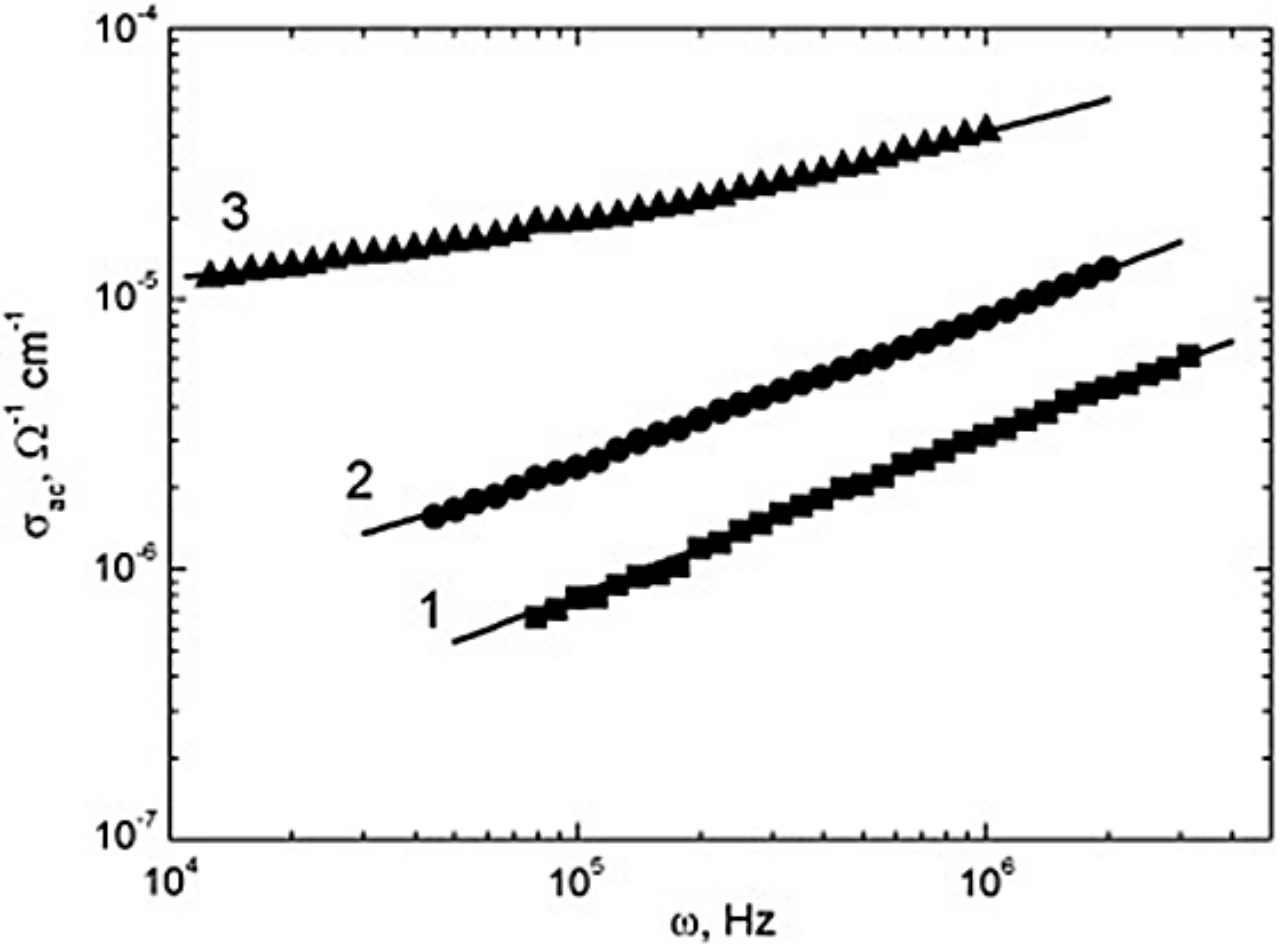

Fig. 17: The frequency dependencies of conductivity of In2O3/Ga2O3 -300 at T=200oK (1), In2O3/Ga2O3 -500 at T=60oK (2) and In2O3/Ga2O3 -700 samples at T=60oK (3). Solid lines are the best-fit lines with Eq. 32

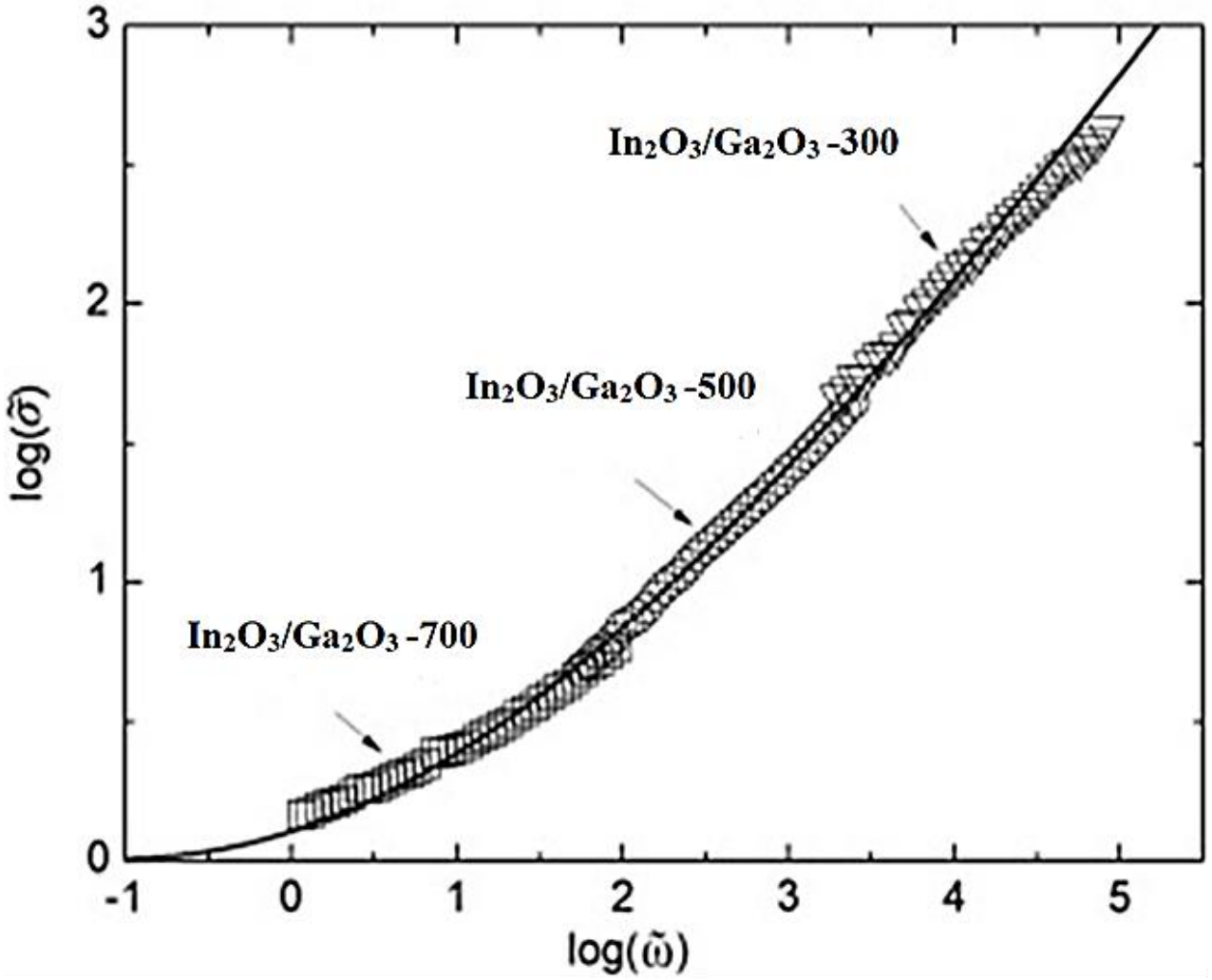

Fig. 18: The frequency dependence of conductivity of the In2O3/Ga2O3 samples in dimensionless values. Solid line is universal line with Eq.33

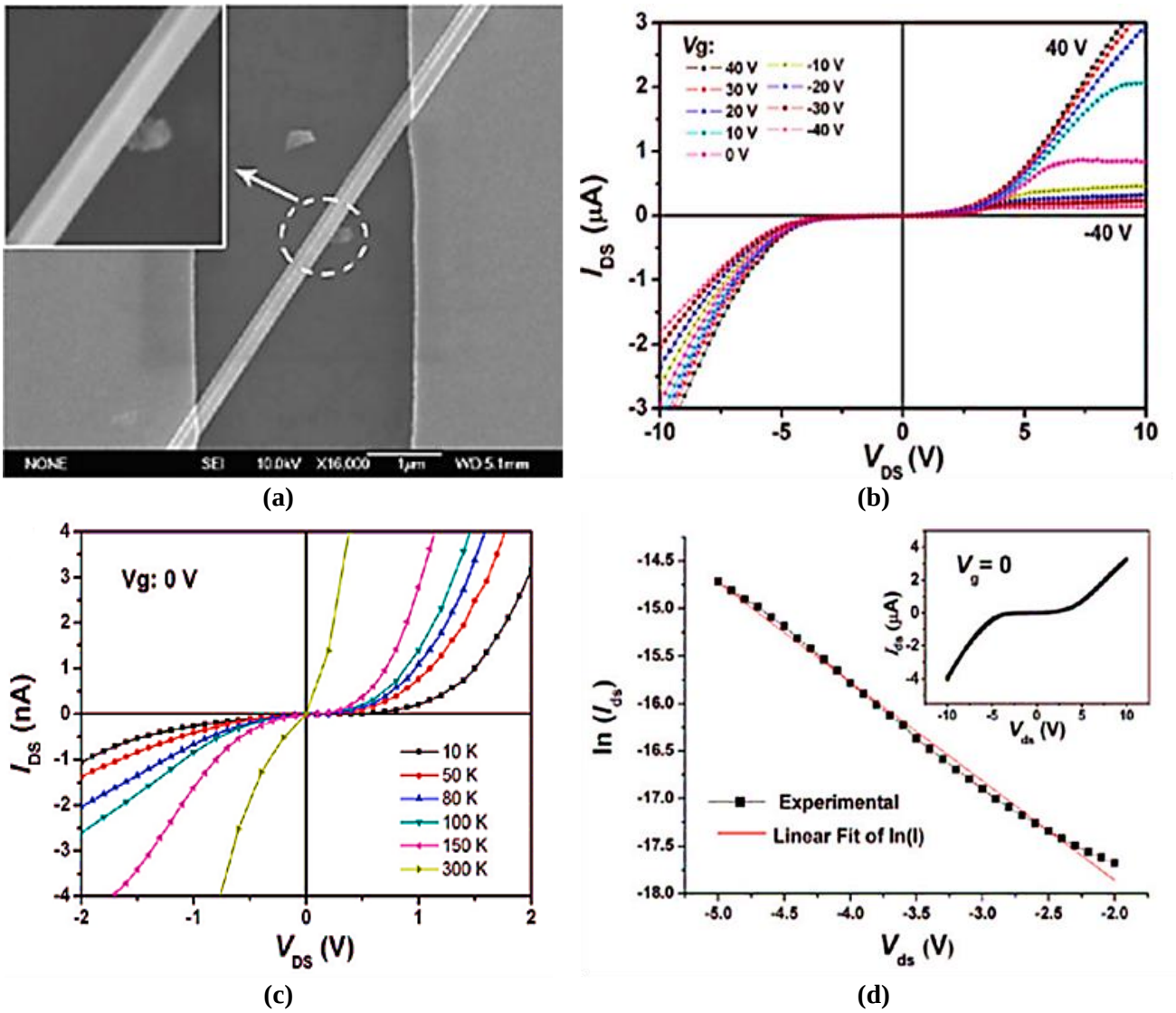

Fig. 19: (a) SEM image of a n In2O3-decorated Ga2O3 heterostructure-based FET; (inset) high-magnification SEM image showing the morphology of the heterostructure, (b) IdsVds plots at different Vg, (c) IdsVds curves measured from 300 to 10 K with Vg=0 V, (d) Experimental and fitted ln I versus V plots at an intermediate bias using the Ids-Vds curve at Vg=0 V, respectively

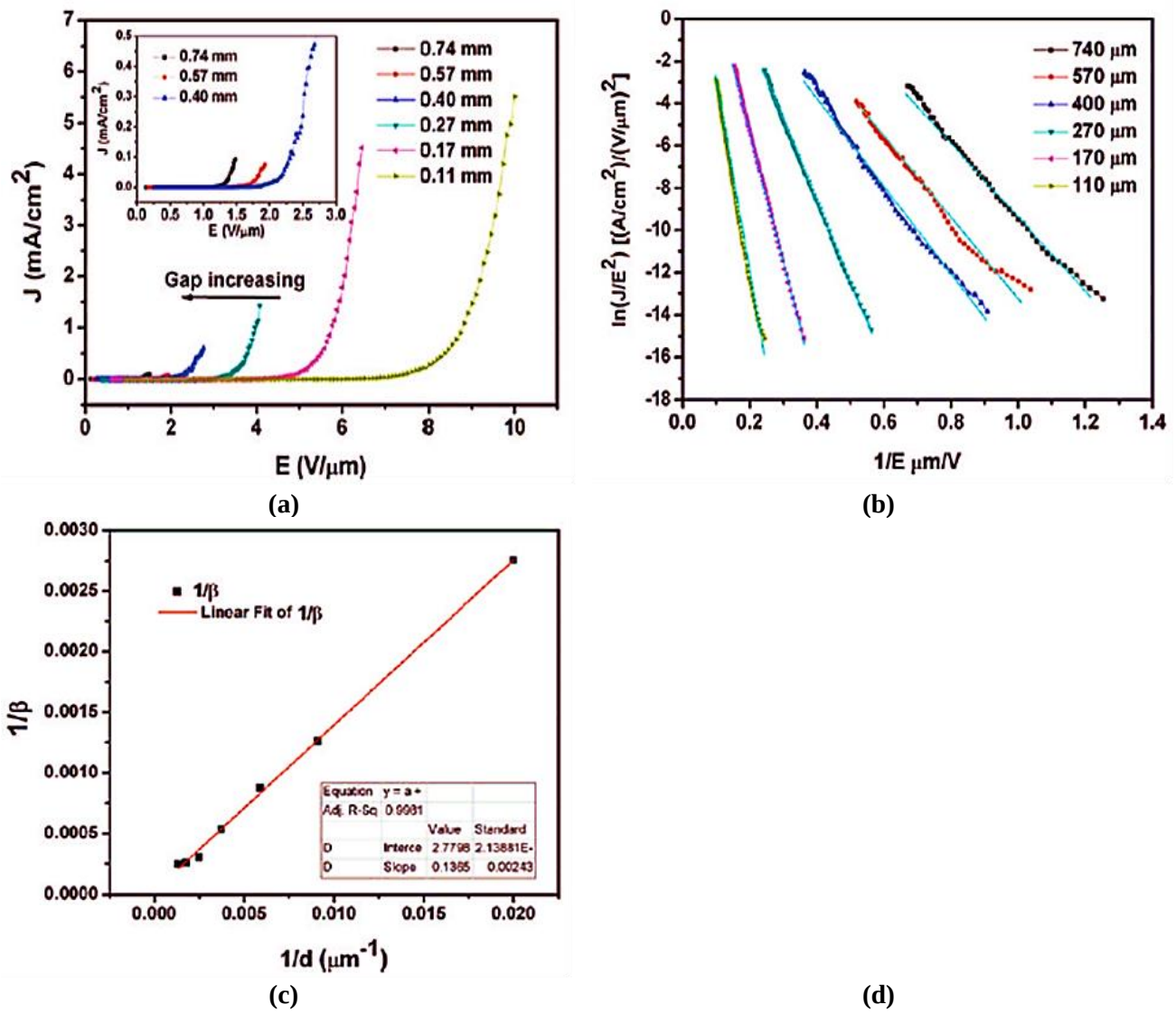

Fig. 20: (a) Field-emission current density versus an applied field (J-E) curves, (b) Field-emission properties of the heterostructures of corresponding Fowler ordheim (FN) plots with different vacuum gaps, (c) Relationship between the field-enhancement factor, β, and a vacuum gap, d. The straight line is the linear fit of the experimental data based on the TRFE model, respectively

Table 4. Turn-on field (Eto) and field-enhancement factor β obtained at different vacuum gaps (d)

Parameters						
d (mm)	0.11	0.17	0.27	0.40	0.57	0.74
E_{to} (V/μm)	6.45	4.23	2.89	1.975	1.70	1.31
B	793	1142	1875	3287	3827	4002

Table 5. Comparative key field-emission performance parameters of the present heterostructures and the conventional Ga2O3 and In2O3 nanostructures reported in the literaturea

Materials	Turn-on field (V/μm)	β	References
Quasi-aligned Ga_2O_3 nanowires	6.2	880	111
Ga_2O_3-C nanocables	7.73		116
Cactus-like Ga_2O_3 nanostructures	12.6	38.2	117
In_2O_3 nanowires	2.47 at 0.1 μA/cm^2	1810	118
In_2O_3 naowires	7 and 10.7 at 1 μA/cm^2		119
In_2O_3/Ga_2O_3 heterastructures	1.31-6.45	793-4002	In this work
[a] Here, the turn-on field is defined as the field required to produce a current density of 10 μA/cm^2. If the other values are used, then this is mentioned separately.			

Table 6. The intermediates of PFOA and PFOS for In2O3/Ga2O3 nanocomposites after photodegradation process

PFOA Intermediates for In_2O_3/Ga_2O_3 Nanocomposites	**PFOS Intermediates for In_2O_3/Ga_2O_3 Nanocomposites**
Perfluoroheptanoic Acid (PFHpA)	Perfluorooctyl Radical (C_8F_{17})
Perfluorohexanoic Acid (PFHxA)	N-Methyl Perfluorooctane Sulfonamido Ethanol (N-MeFOSE)
Perfluoropentanoic Acid (PFPeA)	N-Ethyl Perfluorooctane Sulfonamidoethanol (N-EtFOSE)
Perfluorobutanoic acid (PFBA)	Perfluorooctanesulfonamide
Trifluoroacetic Acid (TFA)	Perfluorooctanesulfonyl Fluoride

Table 7. Effects of increasing In2O3/Ga2O3 nanocomposite concentrations on the yields of PFOA and PFOS

Table 8. Effects of increasing pH on the yields of PFOA and PFOS

In_2O_3/Ga_2O_3 Nanocomposite Concentration (mg/l)	**PFOA and PFOS Photodegradation Yields (%)±SD, n=10**	
	PFOA (%)	**PFOS (%)**
0.1	89±0.00002	86±0.00002
0.5	95±0.00001	93±0.00002
0.75	99 ±0.00001	98±0.00001
1.2	85±0.00001	84±0.00001
1.5	80±0.00002	79±0.00002
2.0	76±0.00002	75±0.00002

pH Levels	**PFOA and PFOS Photodegradation Yields (%)±SD, n=10**	
	PFOA (%)	**PFOS (%)**
2.0	78±0.00001	66±0.00001
3.0	79±0.00001	75±0.00001
4.0	79±0.00001	73±0.00001
7.0	99±0.00001	98±0.00001
8.0	98±0.00001	95±0.00001
9.0	76±0.00001	73±0.00001

Table 9. Effects of PFOA and PFOS concentrations on the yields of PFOA and PFOS

PFOA and PFOS Concentrations (mg/l)	**PFOA and PFOS photodegradation yields (%)±SD, n=10**	
	PFOA (%)	**PFOS (%)**
400	99±0.00001	98±0.00001
700	99±0.00001	98±0.00001
900	99±0.00001	98±0.00001
1000	99±0.00001	98±0.00001
1200	76±0.00002	73±0.00002
1500	76±0.00002	73±0.00003

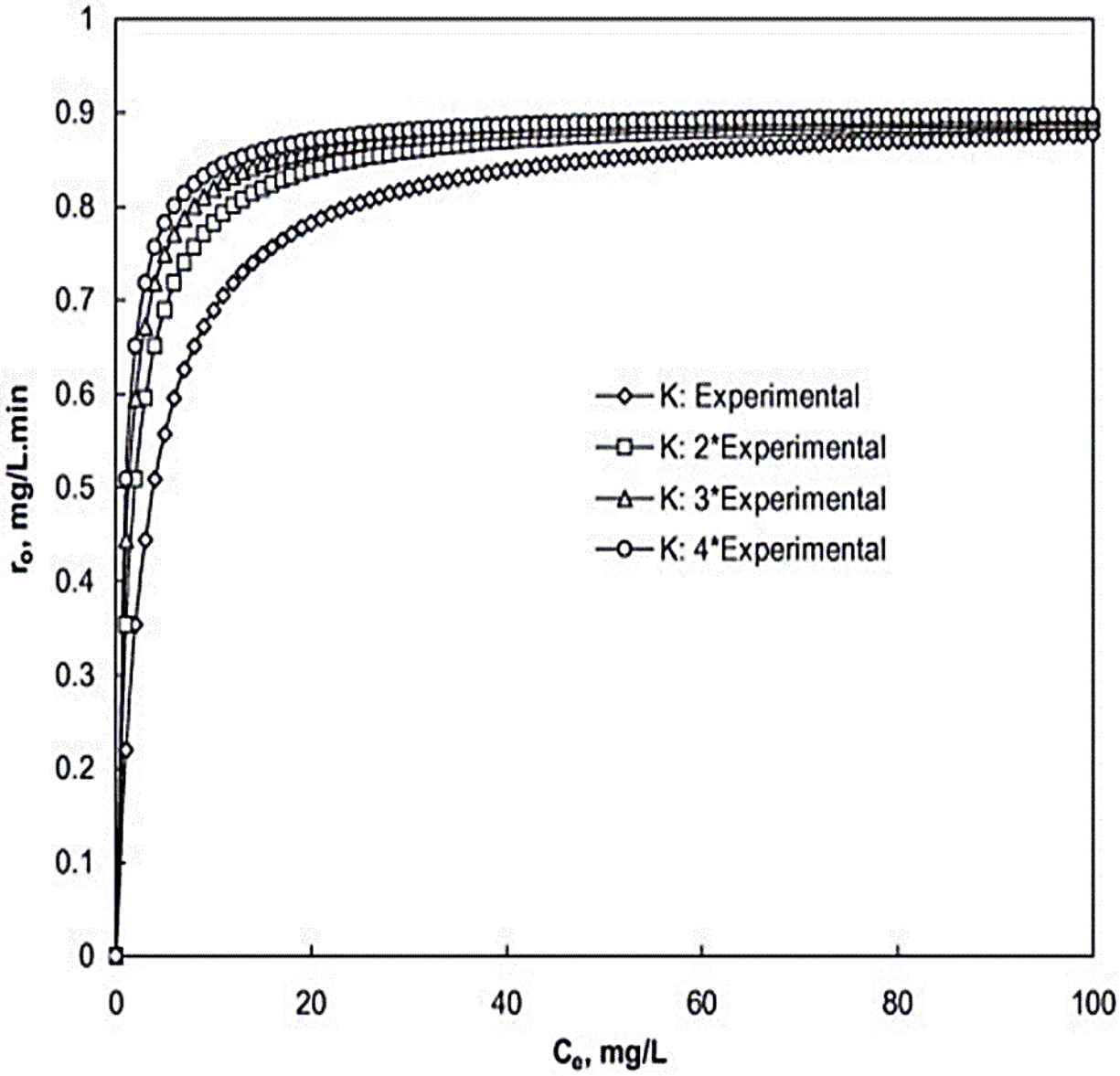

Fig. 21: Plot of τ0 versus Ce for the photocatalytic degradation of 1000 1/liter by PFOA (1.2) and PFOS in the presence of 0.75 mg/l In2O3/Ga2O3 nanocomposite for different K values (0.087, 0.089, 0.090 and 0.099 min-1)

Table 10. Effects of increasing temperature on the yields of PFOA and PFOS

Temperature (°C)	**PFOA and PFOS Photodegradation Yields (%)±SD, n=10**	
	PFOA (%)	**PFOS (%)**
10	34±0.00001	30±0.00001
20	37±0.00001	34±0.00001
30	98±0.00001	96±0.00001
40	99±0.00001	98±0.00001
60	43±0.00001	40±0.00001
80	20±0.00001	18±0.00001

Table 11. Effects of sun light powers on the yields of PFOA and PFOS

Sun Light Power (W/m^2)	**PFOA and PFOS Photodegradation Yields (%)±SD, n=10**	
	PFOA (%)	**PFOS (%)**
10	23±0.00001	20±0.00001
20	30±0.00001	30±0.00001
30	95±0.00001	92±0.00001
80	99±0.00001	98±0.00001
90	43±0.00001	40±0.00001
100	20±0.00001	18±0.00001

Table 12. Effects of rotating speed on the yields of PFOA and PFOS

Rotating Speed (rpm)	**PFOA and PFOS Photodegradation Yields (%)±SD, n=10**	
	PFOA (%)	**PFOS (%)**
1	23±0.00001	20±0.00001
2	30±0.00001	30±0.00001
4	95±0.00001	92±0.00001
5	99±0.00001	98±0.00001
6	83±0.00001	80±0.00001
7	20±0.00001	18±0.00001

Table 13. Effects of time on the yields of PFOA and PFOS

Time (min)	**PFOA and PFOS Photodegradation Yields (%)±SD, n=10**	
	PFOA (%)	**PFOS (%)**
1	23±0.00001	20±0.00001
2	30±0.00001	30±0.00001
5	99±0.00001	98±0.00001
10	90±0.00001	88±0.00001
20	83±0.00001	80±0.00001
25	20±0.00001	18±0.00001

Table 14. Photodegradation of PFOA and PFOS in the samples taken from a river to stimulate the environmental conditions

Parameter	**PFOA Photodegradation Yield (%) n=10±SD**	**PFOS Photodegradation Yield (%) n=10±SD**
PFOA / PFOS concentration (20µg/l)	99±0.0001	99±0.0001
In_2O_3/Ga_2O_3 Nanocomposite Loading (2 µg/l)	99±0.0001	99±0.0001
Photodegradation time (3 min)	99±0.0001	99±0.0001
Sun light power (5 W/m^2)	99±0.0001	99±0.0001
Temperature (18^{o}C)	99±0.0001	99±0.0001
pH=7.0	99±0.0001	99±0.0001
Rotating speed (4 rpm)	99±0.0001	99±0.0001

Table 15. Concentrations of F^- into the aqueous phase during treatment, fluorine remaining in parent PFOS, and corresponding defluorination percentage. Fluorine mass balance and F^- recovery, calculated from the measured F^- and theoretical total fluorine (TF) from PFOS (organicallOAy bound fluorine) at $[PFOS]_0$ = 5 mg/l

	For PFOA				**For PFOS**			
Time (min)	**PFOA (20 µg/l)**	**F^{-1} In aqueos (µg/l)**	**TF bound in PFOA (µg/l)**	**Defluorination efficiency (%)**	**PFOS (20µg/l)**	**F^{-1} In aqueos (µg/l)**	**TF bound in PFOA (µg/l)**	**Defluorination efficiency (%)**
1 min	4	5	15	28	4	17		29
5 min	15	18	5	86	15	3		88

Table 16. Recovery and reusability of In_2O_3/Ga_2O_3 heterogenous nanocomposite

Runs	**PFOA Photodegradation yield (%)±SD (n=10)**	**PFOS Photodegradation yield (%)±SD (n=10)**
1	99±0.00001	99±0.00001
2	99±0.00001	99±0.00001
3	99±0.00001	99±0.00001
4	99±0.00001	99±0.00001
5	99±0.00001	99±0.00001
6	99±0.00001	99±0.00001
7	99±0.00001	99±0.00001
8	99±0.00001	99±0.00001
9	99±0.00001	99±0.00001
10	99±0.00001	99±0.00001
…	99±0.00001	99±0.00001
…	99±0.00001	99±0.00001
60	99±0.00001	99±0.00001
61	99±0.00001	99±0.00001
62	99±0.00001	99±0.00001
63	99±0.00001	99±0.00001
64	99±0.00001	99±0.00001
65	99±0.00001	99±0.00001
66	99±0.00001	99±0.00001
67	99±0.00001	99±0.00001
…	99±0.00001	99±0.00001
…	99±0.00001	99±0.00001
80	98±0.00001	98±0.00001
81	98±0.00001	98±0.00001
82	98±0.00001	98±0.00001
83	98±0.00001	98±0.00001
84	98±0.00001	98±0.00001
85	98±0.00001	98±0.00001
…	98±0.00001	98±0.00001
…	98±0.00001	98±0.00001
97	98±0.00001	98±0.00001
98	98±0.00001	98±0.00001
99	98±0.00001	98±0.00001
100	97±0.00001	97±0.00001